GROUND PENETRATING RADAR (GPR) EXAMINATIONS AT THE FANTA STREAM FOSSIL AND ARCHAEOLOGICAL SITE, CENTRAL ETHIOPIA

by

PETER MATTHEW LANZARONE

(Under the direction of Ervan Garrison)

ABSTRACT

A ground penetrating radar (GPR) survey was conducted at the Fanta Stream archaeological and paleontological site during two field seasons (2009 and 2010). Located in the city of Addis Ababa, Ethiopia, the site contains a rich assemblage of fossil mammals and Acheulean artifacts located in a rare high altitude context. The radar survey provides a three – dimensional data visualization of the subsurface that can be used for both geological mapping and planning for excavations. Stratigraphy at the site can be observed in the stream's cut bank and from hand – augured cores collected in 2009. Major areas of interest have been highlighted throughout this survey that have increased the size of the previously defined site boundaries. Information gleaned from this study provides pertinent information regarding the extent of fossil deposits and serves to assist in delineating the site to aid in its preservation from destruction due to industrial and agricultural practices.

INDEX WORDS: GPR, fossils, Ethiopia, Africa, archaeology, hyperbola, geoarchaeology, shallow geophysics, Addis Ababa

GROUND PENETRATING RADAR (GPR) EXAMINATIONS AT THE FANTA STREAM FOSSIL AND ARCHAEOLOGICAL SITE, CENTRAL ETHIOPIA

by

PETER MATTHEW LANZARONE

B.A., University of Florida, 2008

A Thesis Submitted to the Graduate Faculty of The University of Georgia in Partial Fulfillment of the Requirements for the Degree

MASTER OF SCIENCE

ATHENS, GEORGIA

2011

GROUND PENETRATING RADAR (GPR) EXAMINATIONS AT THE FANTA STREAM FOSSIL AND ARCHAEOLOGICAL SITE, CENTRAL ETHIOPIA

by

PETER MATTHEW LANZARONE

Major Professor:	Ervan Garrison
Committee:	Rene Bobe Rob Hawman

Electronic Version Approved:

Muareen Grasso
Dean of the Graduate School
The University of Georgia
May 2011

ACKNOWLEDGEMENTS

There were many people who made this study possible, without whom I would not have been able to conduct this research project. Firstly, I would like to thank Dr. Ervan Garrison, for his use of the GPR equipment and supplying me with the program I used to complete all of the GPR processing. Without his kindness, I would not have been able to take these materials with me to Ethiopia. I would also like to thank the members of my committee, Drs. Rene Bobe and Robert Hawman. Rene suggested I complete my research at the site, and added me to the research permit. Without his help, this project would not be a possibility. Dr. Hawman has provided me with a strong technical knowledge of the theory and practice of geophysics in general, and I thank him for all his help in answering my questions.

A big thanks to the many friends I made in Ethiopia. Assiged Getahun really made this project run smoothly by showing me the location of the site and assisting me with data collection. His assistance was critical in conducting this project. Mogus Mekonnen and Ayele Desta were also a huge help in conducting the survey. I would also like to thank Dr. Yonas Beyene and Ato Jara Haile Miriam of the Authority for Research and Conservation of Cultural Heritage (ARCCH) for assisting me in receiving the necessary permissions to access the site. Steven Brandt and Erich Fisher also reviewed my grant proposals, without which I may not have received funding to conduct this research.

An additional thank you to all of the people who have assisted me throughout the course of this project while in the US: Zelalem Assefa, Brian Jones, Kent Schneider, Dean Goodman, Nathan Mountjoy and Jacob McDonald.

Further, I am gratefully indebted the following funding sources for this project: Grant – In – Aid of Research from Sigma Xi, The Scientific Research Society; Claude C. Albritton Jr. Memorial Student Research Award; Geological Society of America Graduate Student Research Grant; Geological Society of America Student Travel Grant; Joseph W. Berg Scholarship; University of Georgia Student Association for Archaeological Sciences Small Grant and the Miriam Watts – Wheeler Scholarship.

TABLE OF CONTENTS

LIST OF TABLES

Page

LIST OF FIGURES

Page

CHAPTER I

INTRODUCTION

"We have always been more interested in our own origins than in the origins of anything else. We trace our family roots and take pride in their length. We follow the histories of nations and their sources. We look behind recorded history to the beginnings of civilizations, and ultimately to the beginnings of humanity itself."

– D. Johanson and M. Edey

This thesis outlines and discusses two seasons of shallow geophysical surveys using ground penetrating radar (GPR) conducted at the Fanta Stream paleontological and archaeological site in Central Ethiopia, within Addis Ababa city limits, Ethiopia's capital city (Fig. 1.1). The site was discovered in 2007 and has not been excavated or systematically analyzed to present. A 10-day reconnaissance survey performed by Drs. Rene Bobe and Zelalem Assefa in 2008 was the first surface survey where the collection and examination of fossils and artifacts was undertaken (Assefa, et al., 2008: 1) including the delineation of the site's extent based on surface cultural materials (Fig. 1.2). An additional survey was also performed by Ato Kebede Geleta of the Ethiopian Authority for Research and Conservation of Cultural Heritage (ARCCH), who also estimated the spatial extent of the site (Geleta, 2009: 11) (Appendix A). At the time of this writing there has been no published analysis performed on artifacts, sediments or bone found at Fanta. The age of artifacts and fossils are uncertain up to now, but preliminary work by

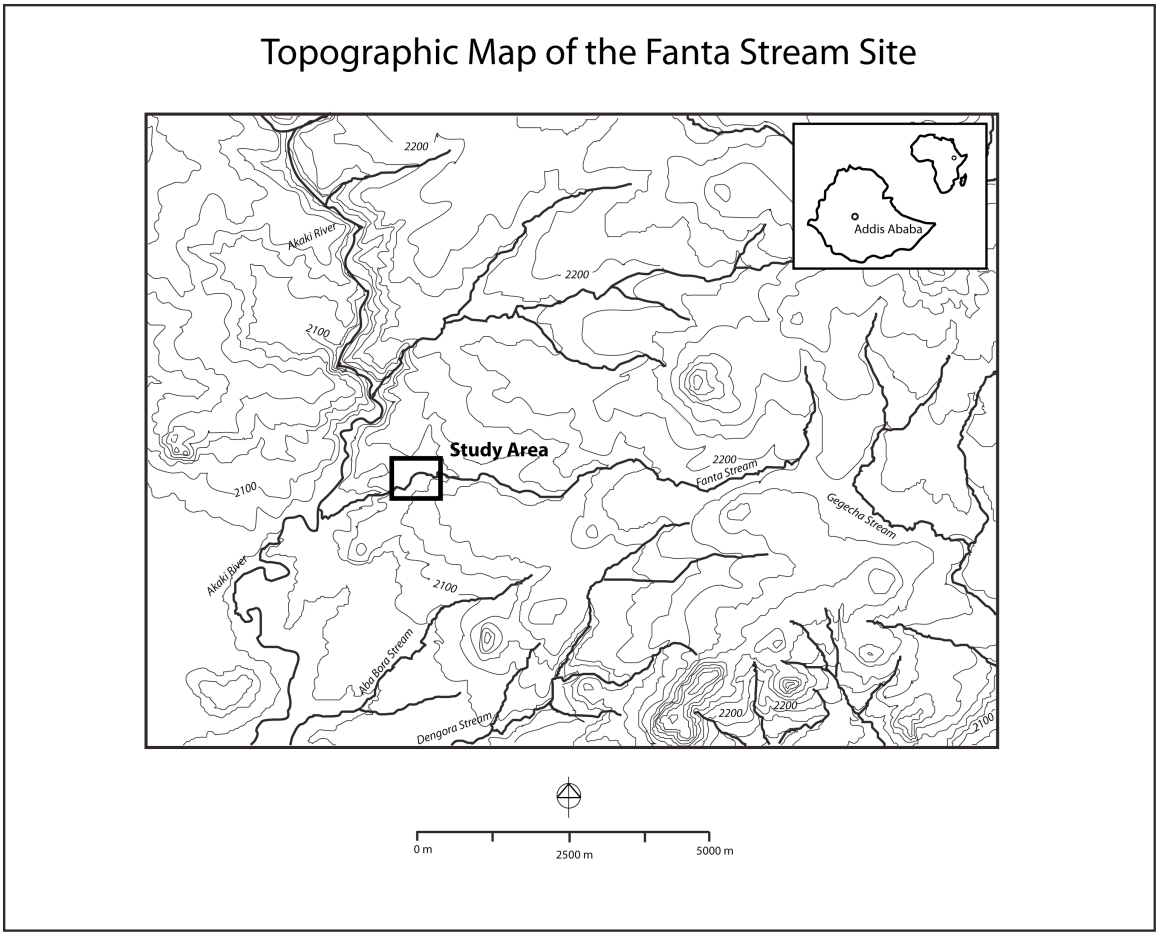

Figure 1.1: Location Map of the Fanta Stream Site with topographic features.

Contour Interval = 20 meters.

Figure 1.2: Initial delineation of the Fanta Site's extent based on surface survey. (Received from Assefa, 2008: 10).

Christopher Lepre (personal communication, 2010) has suggested that the volcanic ash stratigraphically below the fossils is roughly early Pleistocene (1.8 my) in age. Based on preliminary analyses of stone artifacts at the Fanta site, it is suggested that the archaeological deposits at Fanta may date to roughly 600 ka or earlier (Assefa, et al., 2008: 8). This is based on stone tool morphology, where early to middle Acheulean bifacial hand axe and cleaver technologies produced from obsidian and basalt are most commonly represented across the site (Fig 1.3). The site was also discovered along with two other sites, Bantu and Gemeda. Fanta, however is the richest fossil locality of these, being the first and only well – documented Pleistocene archaeological and fossil site within Addis Ababa.

Despite the lack of scientific understanding about the Fanta fossil locality at this time, this relatively small region is currently threatened by the initiation of water drilling projects and local agricultural practices. Specifically, plowing the surface destroys fossils and disturbs the site sediments. The Fanta Stream site is now in desperate need of protection by local authorities to mitigate potential damages due to the effects of agricultural management practices and urban sprawl. The area is also rich in geological resources. Basalts, pumice and clay soils are used for road and house construction, manufacturing household materials and brick production (Getahun, 2007: 29). Mining for these materials is currently taking place only a few hundred meters away from the site which poses an additional danger to the cultural and natural resources at Fanta (Fig. 1.4). The main problem with initiating a protection program for Fanta is the fact that the site is not spatially well

Figure 1.3: Bifacial stone artifact from the surface survey.

Figure 1.4: Photograph of current mining practices occurring at a short distance from the site.

constrained. The location of fossils observed in the stream's cut bank is unknown at any given distance away from the stream's cut bank exposure and fossils appearing on the surface. The principal aim of this thesis is to constrain the spatial domain of the Fanta stratigraphy utilizing a ground-penetrating radar (GPR) system, in hopes of estimating the location of fossils across the site for future protection.

GPR has been applied to archaeological contexts since the late 1970's and little published material has demonstrated the application of utilizing GPR in locating fossiliferous deposits into the present. One noteworthy exception is a paper by Main and Hammon (2003) that used GPR in locating sauropod (Dinosauria) fossils in Texas, USA. Additionally, Stokes and Laub (2006: 2) describe the use of GPR in locating Pleistocene megafauna. Despite these few examples, using GPR to map fossiliferous deposits is a new technique in paleontology, and this study attempts to demonstrate the ability of GPR to provide stratigraphic information that can be used to locate fossil materials at the Fanta Site.

There are many benefits to using GPR in archaeological and fossil contexts, most notably their ability to guide excavations and provide a non – destructive analysis (Sharma, 2002: 323; Garrison, 2003: 79; Kvamme, 2003: 436; Conyers, 2004: 2). The addition of hand – augered boreholes taken at selected intervals across the GPR survey transects provides a ground truth in testing GPR profiles and further constrains the location of primary deposits.

Objectives

It is the aim of this paper to establish a site map using geoarchaeological methods that can be referenced by the Ethiopian Authority for Research and Conservation of Cultural Heritage (ARCCH) in delineating the site's boundaries and thus protect it from industrial and agricultural destruction. Further, it is hoped that GPR and core data analyzed throughout this study will aid archaeologists and paleontologists in future excavation work at the site in order to locate probable fossil and artifact locations across the Fanta Stream and understand the evolution of the Fanta Stream spatially and temporally. Main outcomes of this research will be to:

1. Initialize GPR survey grids in appropriate locations in order to detect where the fossil – containing stratigraphic units are located.
2. Develop a management plan for locating GPR grid and transect positions for future scientific research at the site.
3. Identify the best methods in geophysical processing in order to maximize resolution and depth and to allow for interpretation.
4. Utilize hand – augured borehole data in corroborating GPR grids with ground control.
5. Foster an understanding of ground penetrating radar (GPR) techniques applied to African paleontology to the local Ethiopian community through outreach initiatives.

Background information on the Fanta Stream site, including the natural environmental and environmental history as well as previous research at the site is summarized in Chapter II. Chapter III provides relevant information about GPR principles and theory that will aid in understanding the terminology and concepts discussed in subsequent chapters. This Thesis utilizes GPR as a mapping and visualization tool and discusses its effectiveness at the Fanta site, therefore, citations to appropriate literature describing the methodological theory will be included, but it is not the focus of this study. Special detail in the estimation of depth from velocity in the GPR profiles will also be given in Chapter III. Results received from both the GPR survey and hand – augered soil cores are described in Chapter IV, including the display of GPR images used in interpreting the site's stratigraphy. Conclusions and recommendations for future research at this site are presented at the conclusion of this Thesis in Chapter V. All figures and tables are embedded within the text of each chapter to allow for a continuous display of the ideas and illustrated data.

CHAPTER II

BACKGROUND

History and Natural Environment of the Fanta Site

The Fanta Stream Site was first discovered by Assiged Getahun and his associates of the Ethiopian Geological Survey and reported to the Authority for Research and Conservation of Cultural Heritage (ARCCH) for its registration as a cultural and fossil – containing site in 2007. The site surrounds the banks of the Fanta Stream, located within the city limits of Addis Ababa, the capital city of Ethiopia. To the south lies the border of the neighboring city, Akaki. The Fanta stream is currently surrounded by farmland inhabited by local residents. Rural inhabitants are dependent on raising cattle and dry farming a variety of crops such as: maize, tef, wheat and sorghum. Several grazing animals were noted while conducting work at the Fanta Stream, including: sheep, cow and donkey. The mean annual temperature of this area is at 20^{o} C, with rainfall at 1500 mm per year. Other times of the year are extremely dry, and agricultural practices cannot endure (Getahun, 2007: 4).

The Fanta stream belongs to the Abay and Awash River catchment areas, places that are historically notable for excellent fossil preservation, notably the many hominid discoveries by the Middle Awash Project currently led by White, et al.

(Asfaw, et al., 1999: 629; WoldeGabriel, et al., 2001: 175; Asfaw, et al., 2002: 317; White, et al., 2003: 742). The area at large is characterized by wet climate during the rainy season from June to September, although this time interval varies from year to year (Getahun, 2007: 4). The Fanta site was extensively surveyed using GPR during two field seasons. The first was during the 2009 field season, from June 6th, 2009 to June 20th 2009, where moderate to little rain affected the survey conditions. A second survey was completed from March 13th, 2010 to March 15th, 2010, where no rain impacted the surveys.

Northern Ethiopia is home to the Afar triangle, a famous archaeological and paleonanthropological locale as well as a tectonic triple junction (Winter, 2001: 364) that dominates the regional geology of the East African region (Fig. 2.1). Uplift during the Mesozoic eventually segmented the landscape into a broken three-armed rift associated with alkaline and tholeiitic volcanism (Park, 1997: 162). Volcanism continues into the present episodically throughout the whole of the rift region where major volcanic episodes have spilled over central rifts into adjacent plateaus. The Tertiary – Quaternary tectonic system known as the Rift System is one of the largest structural features of the Earth's crust. This tectonic feature stretches from Mozambique to Syria and is equivalent to 1/6th of the Earth's circumference (Mohr, 1966: 159). The rift system is composed of a complex pattern of narrow, parallel faults, with sunken area between the faults giving the characteristic graben morphology. There are two parts of the rift, the Western Branch and the Eastern Branch. The Eastern Branch runs north into central Kenya and continues north –

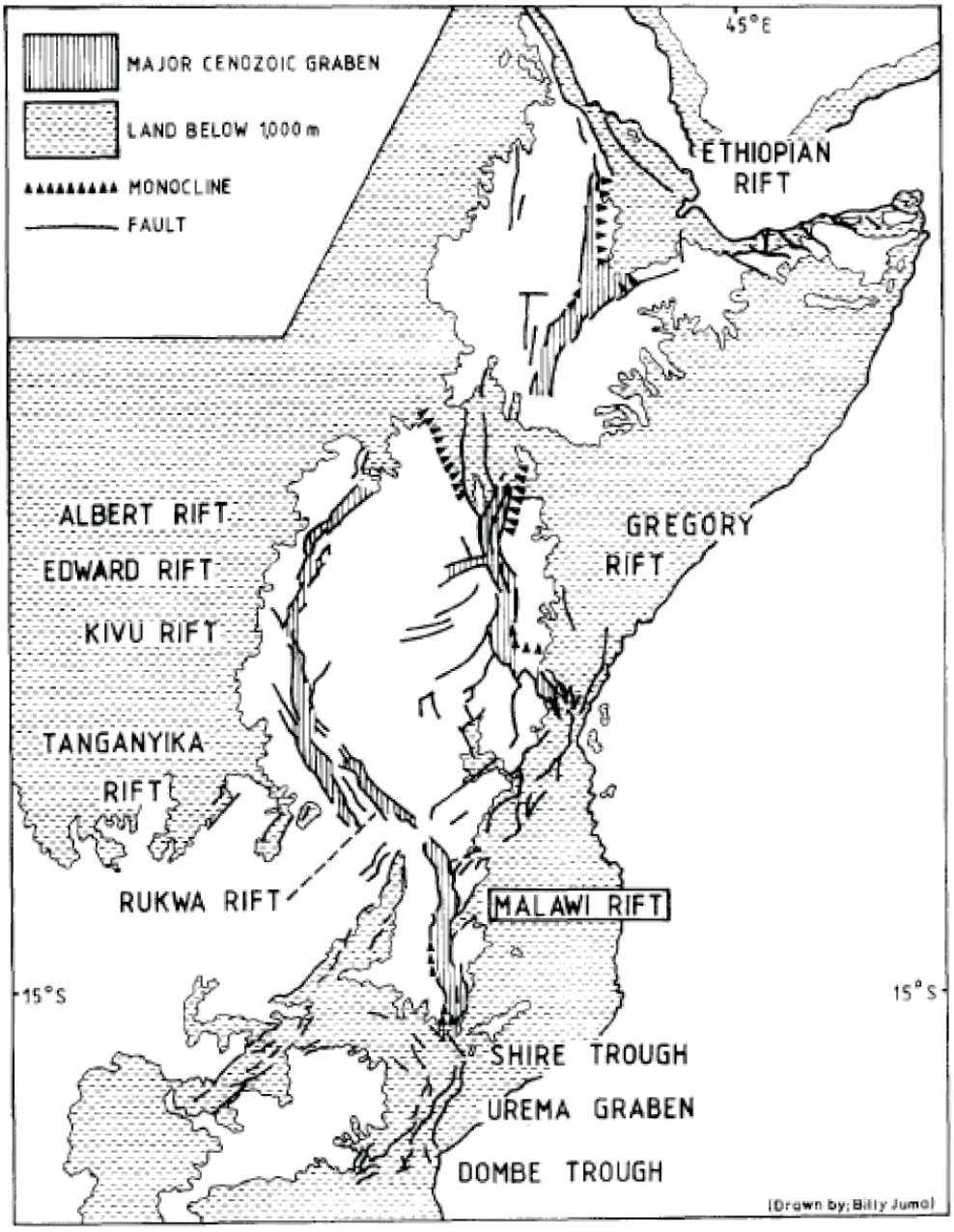

Figure 2.1: Map of the African Rift Valley System (Modified from Crossley, 1984: 34).

northeast into Ethiopia before opening out into the complex sunken region of the Afar.

The local geology of central Ethiopia has been characterized by multiple stages of tectonism and volcanism. Fossils found at the Fanta site are encased in Quaternary sediments that are underlain by basaltic rock types. Two main rock units: olivine basalt and Repi basalt are exposed in the surrounding region and are overlain by fossil containing Quaternary sediments (Getahun, 2007: 19). The olivine basalt is porphyritic, vesicular and crops out to form a central ridge in the surrounding area. Repi basalt is characterized by porphyritic to aphanitic texture, vesicles and local spheroidal weathering associations. This geological environment underlies the Quaternary sediments in which fossiliferous deposits are encased at Fanta. These sediments were produced from a variety of environments and are likely derived from fluvial deposits based on thehigh energy gravel and conglomeritic units.

Description of Previous Research at the Fanta Stream Site

The fossil and archaeological assemblage at the Fanta site is encased in a stratified sequence of sedimentary units initially defined by Chris Lepre of Rutgers University during the reconnaissance of the site in 2008 with Dr. Bobe and Assefa (Assefa, et al., 2008). Sedimentary descriptions outlined throughout this Thesis were based on the observations of the author and from the 2008 Fanta field report (Assefa, et al., 2008: 2 – 4).

Defined stratigraphic units (Fig. 2.2) include the modern plow zone containing clay – rich soils with pedogenic features. This unit is considered 'black cotton soil' (Getahun, personal communication, 2009), and is typified by paleosol features including slickensides, root casts and carbonate nodules. Vertic features are present, indicating seasonal wet/dry intervals at the site. These soils are characterized by montmorillonite 2:1 clay minerals, which have an exceptionally high cation exchange capacity (Jutzi, 1988: 153; Thompson, et al., 1999: 106). The soils shrink and swell with drying and wetting and are thought to pose problematic radar response during GPR surveying due to dispersion of the electromagnetic (EM) energy (Olhoeft, 1996: 1; Conyers, 2004: 50). These deposits are considered to be a product of low – energy deposition and although it is not possible to interpret the precise depositional environment, the unit may be a result of fluvial overbank or lacustrine deposits. The author will refer to this unit as 'clay' for subsequent descriptions and visualizations of data.

There are two fossil beds at the site. The upper fossil unit is encased in a diffuse tuff and graveliferous sequence; this being the most densely packed and well defined fossil bone bed at the site. The lower bone bed is found in a matrix – supported conglomerate and is not very well exposed at the site. These strata were likely deposited in high – energy fluvial environments and may represent lag deposits due to the high degree of abrasion on the fossils.

Because this is an active volcanogenic zone, this area is associated with ashfall or tuff deposits. Preliminary electron microprobe work completed on glass shards by the author show that the tuff displays rhyolitic chemistry (76 – 79% SiO_2)

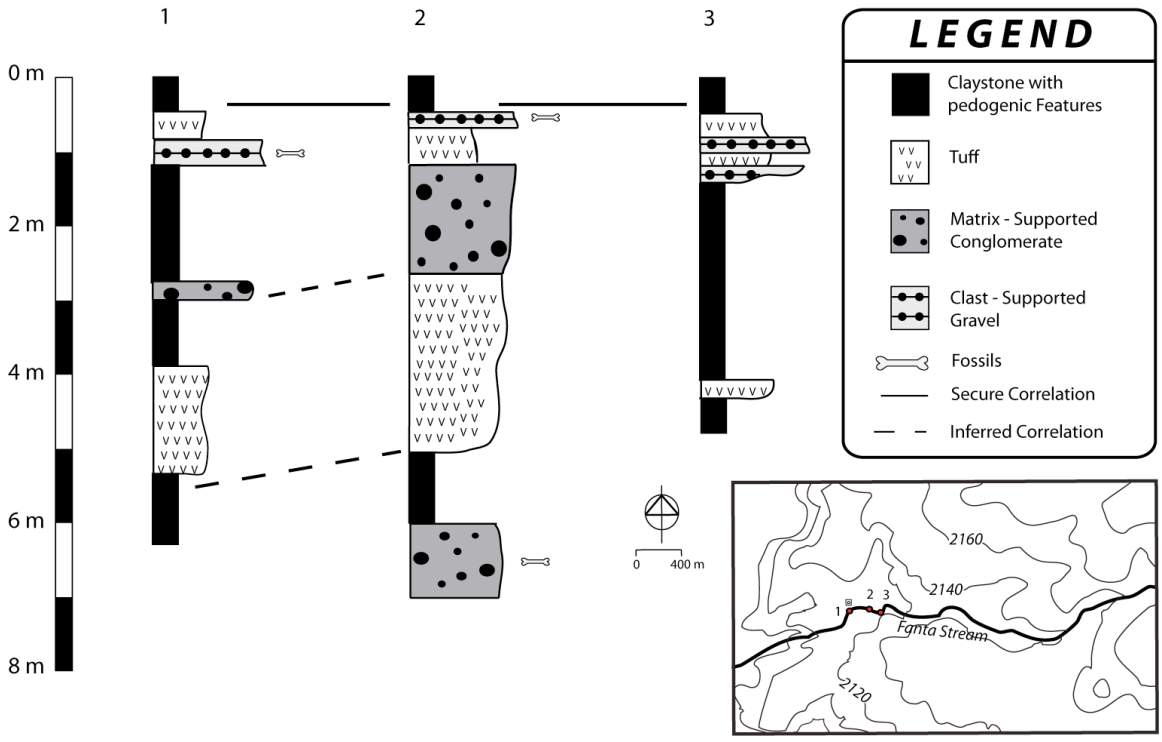

Figure 2.2: Composite stratigraphic section at Fanta including major geological units and sedimentary features. Note the distribution of fossil inclusions (Modified from Assefa, et al., 2008).

in both upper and lower stratigraphic deposits. Due to the extensive volcanic nature of deposits at the Fanta site and encasing a majority of fossil and archaeological sites throughout East Africa, volcanic sediments have been used extensively to define the ages of sites in this region. Tuff deposits show associations of primary sedimentary structures including thinly laminated units of silt and sand – sized glass particles and pumice inclusions. These sediments are interpreted as deposited in a low energy fluvial environment due to its fine grain size and laminated sedimentary structures. The deposits suggest reworking by fluvial action and are considered secondary deposits.

Fossil materials have been observed *in situ* in the stream's cut bank exposure however artifactual materials have only been observed on the surface. Further underlying sediment includes both gravel and conglomeritic sequences that contain fossil deposits at lower vertical depths, and are less well exposed and defined throughout the site. Both stratigraphic units contain coarse sediments where volcanic materials form clasts of sand, pebbles and cobbles. These are interbedded with uppermost tuffs. These coarse clastic sediments preserve fossils, and are lacking sedimentary structures. The deposits are most likely related to high – energy phenomena such as debris flow from flood events or gravity flows, supported by poor sorting and large clast size (Fig. 2.3). Additionally, photomosaics of the stream deposits are presented in Figures 2.4 and 2.5 that document the strata seen in the stream's cut bank. These photographs were taken during the 2010 field season and show changes in sediment thickness at various fossil exposures. No excavations

Figure 2.3: Large, boulder – sized clast within the conglomeritic unit at the Fanta site.

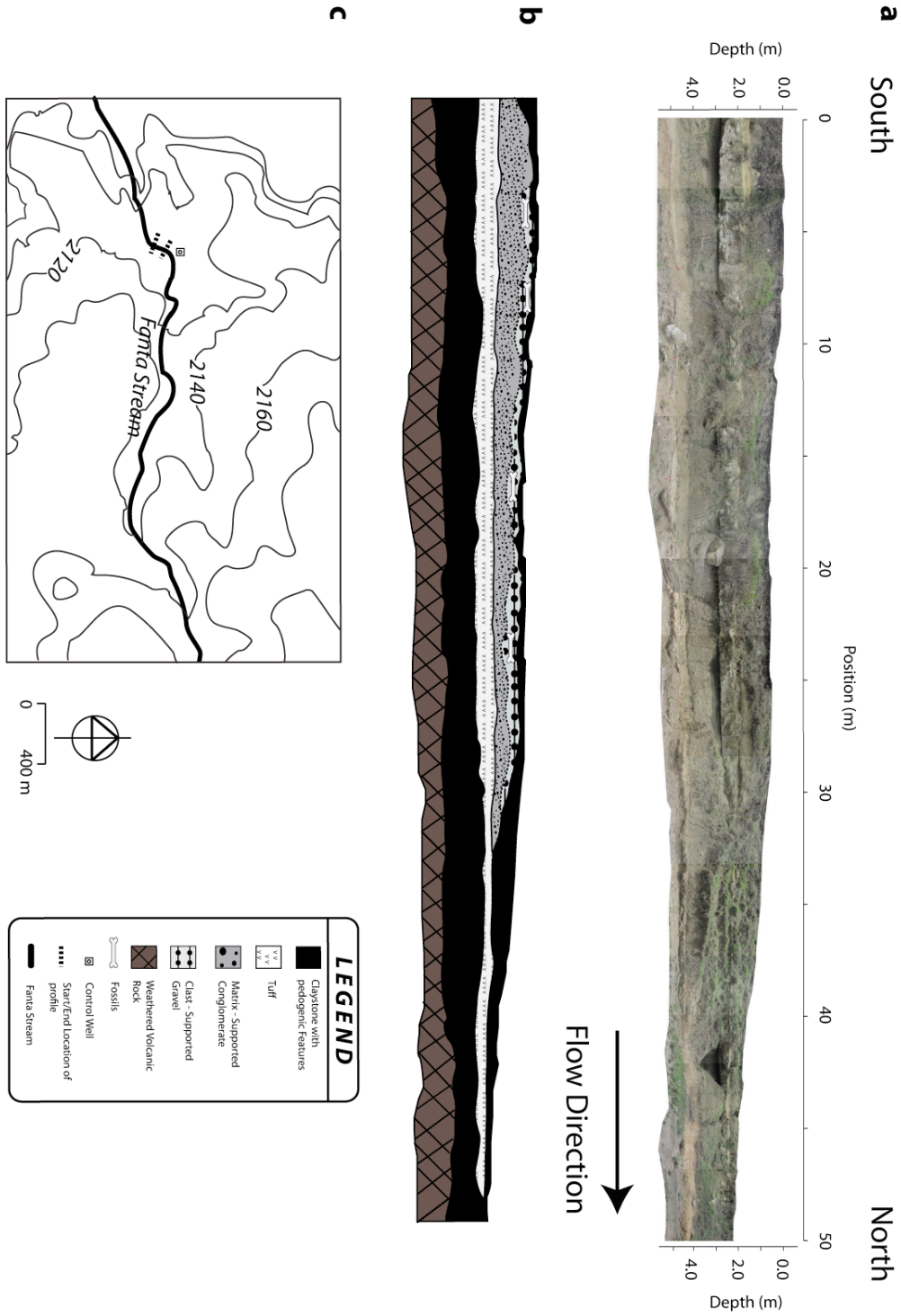

Figure 2.4: (a) Photomosaic of the Fanta Stream exposures. (b) Interpretation of stratigraphic units. (c) Index map. (Photographs taken in 2010)

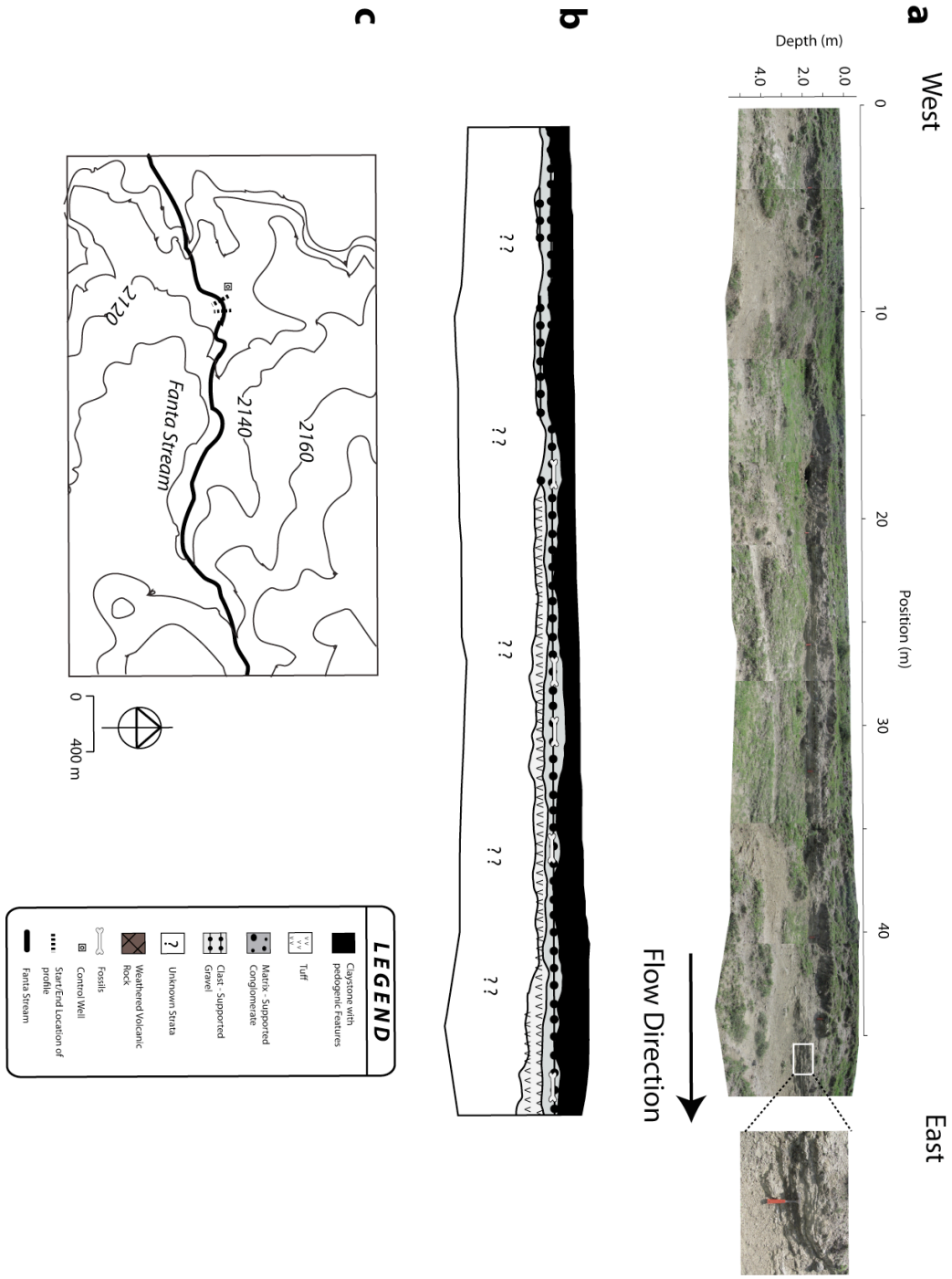

Figure 2.5: (a) Photomosaic of the Fanta Stream exposures (inset highlighting ash deposit features). (b) Interpretation of stratigraphic units. (c) Index map (Photographs taken in 2010).

have been conducted at the time of writing, although some surface samples of stone artifacts from the Gemeda site and faunal material from Fanta currently reside in the National Museum of Ethiopia for current storage and future analytical purposes.

The Importance of the Fanta Site

The Fanta Stream Site is an extremely important cultural and natural resource. The location of the site with relationship to the Awash River is significant with regard to the regional context of the African rift valley where a variety of hominid fossils have bee discovered by various paleoanthropological groups working in this area. Ethiopia, in general, is considered the 'cradle of humanity' due to its sites that display fantastic preservation of fossil materials of early human remains. The well preserved and little disturbed Fanta site adds significantly to our understanding of Plio – Pleistocene paleoenvironments existing when early hominids emerged. Fanta, if properly characterized using shallow geophysics and sediment coring, will provide new data to advance our understanding of these paleoenvironments during a critical time in hominid evolution where few sites of a high – altitude context have been observed and recorded.

The site's history is complex, and the reliance on understanding the nature of sedimentary deposits within the stream's cut bank and with hand – augered cores is important for characterizing the nature of the fossil deposits at the site. The site is also considered to be deposited by pluvial events. Pluvial deposits are formed by meteoric water deposition. This commonly occurs as the fluvial action of rainwater flows through a stream channel, especially in the case of an ephemeral stream

(Nuendorf, 2005: 501) such as Fanta. Ethiopian rivers commonly show aggradational terraces in pluvial alluvium, as in the Akaki and Mojjo rivers (at 3 – 5 meter and 10 meters, respectively) in the Addis Ababa region, present – day incisive action is the general rule for all Ethiopian rivers. Silt deposits seen in this area are attributed to being largely derived from the Ethiopian Plateau, relating to the emptying of Lake Yaya by immense Pleistocene uplifting and tilting (Mohr, 1966: 205). Quaternary terrestrial sediments are extensively developed on the high plateau where sedimentary rocks are derived from Tertiary intravolcanic lake sediment (Mohr, 1966: 206; Getahun, 2007: ii). Thick lateritic soils are also characteristic of the high plateau in Ethiopia. These terrestrial deposits are generally formed by calcification and ferruginisation of torrent and slope – wash gravel during arid interpluvial periods.

The fossil mammals at Fanta are found in the plowed agricultural fields and within the stream's cut bank exposure (Fig. 2.6). The most abundant fossils at the site are *Hippopotamus*, Bovidae, and *Equus* taxa, of which 19 specimens are currently curated at the National Museum of Ethiopia. Although the exact number of fossil specimens at the site is currently unknown, future excavation work will surely shed light on the types of organisms and their respective abundances. The large proportion of hippos indicates permanent water near the site of deposition.

Ecologically, hippos' use of swamps and waters as day time refuges has allowed them to develop a successful ecological strategy (Kingdon, 1997: 324). Bovids or Bovidae are horned ungulates that are characteristically long – legged and hooved (Kingdon, 1997: 346). Specialization in grass – eating confirms the presence

Figure 2.6: Fossils from the surface survey.

of highland grassland habitat in this area. The presence of *Equus* additionally allows the constraint on the age of the site to late Pliocene to Pleistocene and confirms the presence of an open grassland paleoecosystem (Assefa, 2008: 8).

The importance of this site is not well – realized or well understood at the time of this Thesis submission. What is known is that the Fanta site contains a dense accumulation of vertebrate fossils in a small section of the stream. Due to the high altitude context of the site, information on the fossiliferous deposits may yield important insight into the paleoenvironment and paleoecology of the East African Quaternary Period. The site may allow for significant understanding of early hominid evolution, where there is a current lack of data throughout this region within a high – altitude context. The extent of the fossil unit is not well constrained laterally and vertically across the site, and it is thus the goal of this study to use GPR and soil coring in order to determine the spatial occurrence of stratigraphy, in particular the location of the fossiliferous beds.

CHAPTER III

METHODOLOGY

Additional Background

This study is unique in the fact that there has been very little GPR research performed and published into the present throughout eastern Africa for archaeological purposes. Although there have been several publications utilizing GPR in Egypt (Shaaban and Shaaban, 2001; Kamei, et al., 2002; Abdallatif, et al., 2003) and the Middle East (Witten, et al., 2000; Casana, et al., 2008; Seren, et al., 2008), there is a substantial lack of modern literature applying radar in the context of the east Africa as a whole. This may be a manifestation of difficulties inherent in working within remote areas where there is a lack of infrastructure in accessing sites. Other concerns include the laborious processing of transporting geophysical equipment overseas and the administrative security clearances required. Logistical considerations involved in working in Ethiopia are tremendous and time – intensive, especially when utilizing costly scientific equipment. Recently however, this is beginning to change, and more studies are beginning to emerge using GPR in Africa and Ethiopia.

Orlando and Soldovieri (2008) document the use of GPR at Axum archaeological park in Northern Ethiopia. Despite the exciting nature of the survey performed in order to preserve buried fragile archaeological features at this

location, the paper reported on varying approaches in data processing, not with the aim of interpreting archaeological features in the park. Regardless of the lack of archaeological significance and feature interpretation, the article highlights the utility of GPR as a non - invasive prospecting tool, being the most suitable geophysical method for imaging the shallow depths below the surface (Orlando and Soldovieri, 2008: 1-2).

Arthur, et al., 2009 described the use of GPR at Ethiopian archaeological sites with a survey conducted by Dr. L Conyers during the summer of 2008. They described the interpretation of GPR profiles collected at five sites located in the Gamo Highlands of Southern Ethiopia. The detection of wall structures, hearths and compact floors were made possible by GPR prospection, which would otherwise not be constrained and mapped non – destructively (Authur, et al., 2009).

A study conducted in 2007 by the Sodo Wolayta Archaeology Project (Project Investigators Brandt and Hildebrand) also utilized ground - penetrating radar in mapping stratigraphic contacts at Moche Borago, a large rock shelter located in the Southern Ethiopian Highlands. The GPR survey conducted by Erich Fisher (in Brandt, et al., 2007) revealed the possible maximum depth of archaeological deposits at the site. Also, the nature of stratigraphic units below the lowest excavated sedimentary unit was described as non – volcanic in origin based on comparative GPR signatures from other excavated deposits at Moche Borago (Brandt, et al., 2007: 5). The author of this Thesis assisted with collecting the GPR data during this study in 2007 and conducted an additional GPR survey in 2010 at Moche Borago.

Despite these few documented studies, which includes one peer - reviewed journal article (Orlando and Soldovieri, 2008) one presentation (Authur, et al., 2009) and one unpublished field report (Brandt, et al., 2007), there are little to no other studies reported of using GPR throughout in this region. This is extremely unfortunate, considering the rich quantity of archaeological and paleontological sites throughout Ethiopia. A field report outlining the preliminary results of data presented throughout this Thesis is currently on file at the Ethiopian ARCCH office in Addis Ababa (Lanzarone, 2010).

It is hoped that this study will help to shed light on the application of GPR analyses in this incredibly diverse setting, where many threatened or endangered sites could benefit from GPR investigations that are commonly performed at North American archaeological sites.

Introduction to GPR Theory

Ground-penetrating radar has become a major geophysical tool for a variety of environmental, engineering, geological and archaeological studies (Vaughan, 1986: 595; Conyers, 2004: 2; Sharma, 2002: 309; Garrison, 2003: 75; Kvamme, 2003: 436; Gaffney, 2008: 313). Although the ranges in applications are many, the principles of electromagnetism are applied through all examinations utilizing GPR in understanding the information highlighted in radargrams and time slices. GPR also borrows some concepts and techniques from seismic data acquisition, processing and interpretation (Jol, et al., 1996: 960; Baker, et al., 2001: 627; Hildebrand, et al., 2002: 9 - 10). Some studies even combine the use of shallow seismic data with GPR

data (Derobert and Abraham, 2000; Baker, et al., 2001; Cardarelli, 2002; Schwamborn, et al., 2002; Ghose and Slob, 2006). Understanding methods and theory behind seismic reflectivity is particularly advantageous when interpreting radar data; and despite inherent differences in seismic acoustic versus EM waves, seismic and GPR data are both based on reflection imaging and wave propagation in sediments (Hildebrand, et al., 2002: 10).

GPR relies on the propagation of electromagnetic (EM) waves, generally between frequencies of 10 and 1,500 megahertz (MHz) (GSSI, 1995b: 2). This frequency range lies within the same section of the EM spectrum as FM (frequency modulation) radio, television and communication devices (Conyers, 2004: 24). Radar waves are generated in a control unit and are both transmitted and received through an antenna. The most common GPR system is a fixed, or so – called 'monostatic' system that contains both the receiver and transmitter housed in a set geometry (Annan, 2009: 4). The system is usually towed over the ground surface and detects changes in the electrical properties of subsurface materials of the area under investigation. The antenna used in this study was a monostatic system, which provides ease of data collection and equipment transport. Additionally, the antenna was a shielded model that encloses the antenna and selectively enhances the system to ground coupling in order to minimize interference from surrounding objects or internal and external signaling. This lessens leakage effects into the air and is common for most GPR systems at greater than 100 MHz frequencies (Annan, 2009: 29). Bistatic models utilize two separate antennas with a fixed – offset and provide some advantages over monostatic systems (generally greater penetration), although

utilizing this configuration was not a possibility for this study due to costs and transport.

Energy used in transmitting electromagnetic (EM) pulses derive from a trigger generated in the control unit that is directed through a cable and into the antenna (100 MHz, etc.), where a copper plate or wire produce an applied oscillating electrical current. The frequency of the oscillation is based on the center frequency of the antenna, and controls the wavelength of electromagnetic energy sent into the subsurface (Conyers, 2004: 23). The center frequency describes a range of ± 50% above and below this value, so a 100 MHz antenna transmits EM energy from 50 – 150 MHz (Garrison, 2003: 76). This oscillation frequency controls the relative depth that the EM wave can penetrate and reflect back to the control unit. Generally, higher frequencies generate short wavelengths that penetrate into the shallow subsurface while lower frequencies generate long wavelengths that penetrate deeper, based on subsurface conditions.

Radar reflections occur at the interface of two dielectrically contrasting materials, the degree of which is related to the relative amplitudes of reflected waves. The observed reflections are created by changes in electrical and magnetic properties that relate to water content, bulk density or the lithology of discontinuous surfaces. The wave velocities, amplitudes and other parameters change as a function of relative dielectric permittivity (RDP), dielectric permittivity or the dielectric constant (ε), the main driver that gives rise to reflections in the data. The concept of RDP is unique to geophysical literature (Baker, et al., 2007: 4) and is a measure of the ability of a material to store an electrical charge within an

applied electric field,; its value ranging from 1 to 81 (Sheriff, 2006: 88; GSSI, 1995: 30; Sharma, 2002: 311). It is a dimensionless ratio of electrical displacement (D) to the electrical field strength (E) of the material (Dobrin and Savit, 1988: 754; Sheriff, 2006: 88; Baker, et al., 2007: 7; Cassidy, 2009: 44):

$$D = \varepsilon E \qquad (1)$$

In terms of RDP and its relationship to radar velocity, this value can be expressed as (Conyers, 2004: 48):

$$\varepsilon = \left(\frac{c}{V}\right)^2 \qquad (2)$$

Where c is the speed of light (.2998 m/ns) and V is the velocity of the material through which the radar waves pass through (m/ns). GPR is thus best suited to operate in subsurface conditions where strata are changing abruptly over a short distance.

Most earth materials are considered dielectric, in that they represent electrical insulators. This can be expressed by satisfying (Baker, et al., 2007: 4):

$$\frac{\sigma}{\omega\varepsilon} < 0.01 \qquad (3)$$

where ω is angular frequency expressed in radians/sec and σ represents the electrical conductivity (Siemens/meter). A material's conductivity is an additional factor that greatly influences its ability to affect the radar signal. Conductivity is defined as the ability of a material to conduct an electrical current and the ease of electron movement within a material under the influence of an external electrical field (GSSI, 1995a: 13; Sheriff, 2006: 64; Baker, et al., 2007: 5). The property of sediment conductivity is a result of charges from dissolved anions and cations. Conductivity increases with increasing water, clay and soluble salt contents. Radar wave energy losses are mainly derived from ionic charge transport in soil solution and the electrochemical processes of ions in clay minerals, which can greatly affect GPR performance in clay environments (Doolittle and Butnor, 2009: 180). In metals, highly conductive charges relate to the free electrons of metal atoms. At low antenna frequencies (like the 100 MHz antenna used in this study), the charge response of the radar wave into the material is instantaneous and is 'in – phase' with the electrical field (Cassidy, 2009: 54). Conductivity in this sense can be represented by a real or static value, σ, and has units in S/m or Siemens per meter. This parameter shares an important relationship with resistivity ρ, another EM parameter that relates to the measure of the resistance of electrical flow through a material (Dobrin and Savit, 1988: 752; Sheriff, 2006: 298) and is given by (Garrison, 2003: 60):

$$\sigma = \frac{1}{\rho} \qquad (4)$$

Reflections received by the control unit are converted into electrical signals that generate changes in voltage that can be recorded and processed using digital processing programs (Conyers and Goodman, 1997: 28). The remainder of EM wave energy not reflected off of the first electrically contrasting interface is propagated further into the subsurface until its energy is attenuated, or greatly weakened to the point of dissipation. The reflection strengths differ for varying materials and their contrast to over and underlying sediments. Higher amplitude reflections relate to stronger contrasts in RDP whereas lower amplitude materials may reflect more subtle changes in stratigraphy. Reflections generated in the GPR profiles can be visualized using a variety of geophysical processing programs. The program utilized in this investigation is GPR SLICE ® version 7.0.

Radar Resolution

In general, the performance of ground penetrating radar can be expressed in terms of two characteristics: maximum penetration depth and depth resolution (Noon, et al., 1998: 127). Resolution describes the limit and certainty of information collected using GPR. This principle considers the position and geometrical attributes of a target or radar event (Annan, 2009: 14). An important aspect in using GPR is determining the appropriate resolution required and selecting the best start-up parameters with which to conduct the survey. This property is a function of wavelet sharpness (or pulse width), and is proportional to the antenna frequency and the electrical properties of materials being analyzed (Neal, 2004: 279). For vertical depths, the pulse width and velocity of materials being analyzed dictate the vertical

resolution. This is governed by wavelength (λ), the resultant of wave velocity (*V*) divided by the frequency (*f*) (Schwamborn, et al., 2002: 263; Garrison, 2003: 76; Knight, et al., 2004: 2):

$$\lambda = \frac{V}{f} \qquad (5)$$

Solving for Equation 5 using an average velocity from the Fanta site (a more detailed discussion regarding the methodology used in achieving this value can be found later in this Chapter) at 0.036 m/ns and the center frequency of the antenna at 100 MHz gives:

$$\lambda = \frac{3.6 \times 10^{7}\ m/s}{1 \times 10^{8}\ s^{-1}} = 0.36\ m$$

Considering that resulting vertical resolution can be estimated as one quarter the wavelength for vertical separation of distinct features (Jol, 1995: 693 – 694; Schwamborn, et al., 2002: 263; Grasmueck, et al., 2005: 13) and calculating the result:

$$\frac{\lambda}{4} = \frac{0.36\ m}{4} = 0.09\ m = 9\ cm$$

This implies that a 100 MHz antenna can resolve objects that have greater than 9 cm of vertical separation between distinct features. Vertical depth resolution and the GPR depth of investigation generally decreases as a result of an increase in electrical conductivity, water content, clay content, scattering and conductive contaminants (GSSI, 1995a: 26; Schwamborn, et al., 2002: 263). The user has no control over these factors in the field. Vertical resolution is important in determining the scale of sedimentary structures, laminae and stratigraphic units being observed (Neal, 2004: 280).

Horizontal resolution is dependent on the velocity, pulse – width and distance of the target to the system (Knight, et al., 2004: 2; Neal, 2004: 281; Cassidy, 2008: 143; Deiana, et al., 2008: 224; Annan, 2009: 16). This is also known as the Fresnel zone, defined as the portion of the reflector from which reflected energy can reach a detector within one – half wavelength of the first energy reflected (Dobrin and Savit, 1988: 290; Schwamborn, et al., 2002: 263; Grasmueck, et al., 2005: 15; Sheriff, 2006: 153). This sets a limit on the horizontal resolution, which increases as a function of reflector depth (Sharma, 2002: 149). This is given by (GSSI, 1995a: 30):

$$R_F = \left(\lambda r_0 + \frac{1}{4} \lambda^2 \right)^{\frac{1}{2}} \qquad (6)$$

Where R_F is the radius of the first Fresnel zone (describing the first reflection) λ is wavelength and r_0 is the depth to the target. Using the wavelength calculation from

Equation 4 yields:

$$R_F = \left(\left[0.36\ m \times 4\ m \right] + \left[\frac{1}{4} \times 0.36\ m^2 \right] \right)^{\frac{1}{2}} = 1.21\ m$$

A value of 1.21 meters was obtained for the Fresnel zone radius, and the horizontal resolution is thus a function of this distance on either side of the center of the antenna, having a total horizontal resolution of $2 \times R_F$, at 2.42 meters diameter. Adjusting the spacing of the radar antenna so that enough overlap is sufficient to stay within the Fresnel zone during data collection provided sufficient horizontal resolution throughout 2009 data collection procedures. 2010 data is subjected to a large error in interpolating time slices across transects spaced from 10 to 20 meters apart and was not done for 2010 survey.

GPR System and Functional Survey Equipment

GPR data collected from the Fanta site was acquired using GSSI (Geophysical Survey Systems, Inc.) equipment owned by the Anthropology Department at The University of Georgia. This included the following:

- GSSI SIR – 2 System Control Unit
- Monostatic, shielded GSSI 100 MHz single frequency antenna
- Shielded cabling

Additionally, a 12 – Volt automobile battery was used to supply power to the equipment.

These items were utilized in operating and deploying the GPR system at the Fanta site. Several other materials were required in deploying the survey grids, providing ground control. This includes:

- 4, 100 – Meter tapes
- Flagging tape
- Plastic Flags
- Garmin hand - held GPS system
- Brunton compass
- 3 – Meter hand – auger
- 30 wooden stakes

The equipment listed above provided control over the set – up parameters for the survey during GPR operation and was important in managing the survey. Knowing the location of the survey grids was extremely important in tying the GPR survey units to a location in space that can be referenced during future research at Fanta.

Additionally, a GSSI 500 MHz antenna was taken into the field during the 2009 field season in order to provide additional higher – frequency, higher – resolution data. Resulting data with this instrument yielded an extremely noisy dataset with no coherent reflection patterns. Despite post – processing analysis, there was no information provided about the subsurface from this equipment. The

radar unit may have been damaged during air transport from the USA to Ethiopia. Several of these grids were collected but are not listed in the site maps or are interpreted. However, the survey continued with the 100 MHz antenna for the rest of the field season, allowing for a larger coverage across the site with the single antenna.

Survey Procedures: 2009 Season

The first day at the Fanta site entailed a ground survey without the use of GPR. This was done in order to plan for future grid set – up and to observe site conditions. Conditions related to soil moisture, topographic features and accessibility were noted and photographed as well as meeting with local residents at the site. A student (Ayele "Butu" Desta) at the local kebele (school) was hired to assist in the field and was employed for the duration of the 2009 survey.

Multiple GPS readings were taken at the established main control point at the site, a permanent water well encased in concrete, referred to as the 'control well' for the remainder of this Thesis (Fig. 3.1). This was chosen because it is the only permanent structure located near the fossil and archaeological deposits, and appeared at the center of the fossil exposures. All GPR grids were referenced to this point for ground control using a Brunton, meter tapes and GPS points. GPR grids of various sizes were placed surrounding the Fanta Stream cut bank area in order to provide a multi – scalar data visualization of subsurface stratigraphic units and totaled 19.2 km^2 in area. Initial grids were established in representing the best possible locations for deposits to be located based on their proximity to the exposed

Figure 3.1: Permanent control well used in spatially defining GPR survey grids.

fossils. Subsequent grids were scattered across the site and in various locations and sizes based on the day – to – day processing that took place in determining where the next probable location of fossiliferous and archaeological deposits occur. Figure 3.2 documents the location of the 2009 grids and 2010 transects with reference to the control well and the Fanta Stream. Additionally, Figure 3.3 shows this map overlaying the defined site boundaries set by Bobe and Assefa (Assefa, et al., 2008).

The GPR system was brought into the field following the initial surface survey to establish the ability of the GPR signal to properly function and map stratigraphy at known fossil locations. This was done as a test, to see if signal penetration and reflections could be visualized on the control unit. My assistant and friend from the Ethiopian Geological Survey and Addis Ababa University, Assiged Getahun, towed the antenna in a continuous run mode across the grid. Ayele moved tapes and the antenna cable, and the author operated the control unit and took notes. These tasks were periodically switched throughout each surveyed grid between Assiged and the author.

Notes were complied about survey grids that describe detailed information about the survey location. This includes GPS coordinates taken at grid corners, transect spacing, transect length, direction, surface disturbances, total area and line breaks. Line spacing is an extremely important aspect of survey design, relating to the detail desired and the size of the survey area (Bristow, 2009: 277). A listing of complete GPS coordinates at each grid along with other diagnostic information is presented in Table 3.1. GPS coordinates of each grid corner are presented in Appendix B.

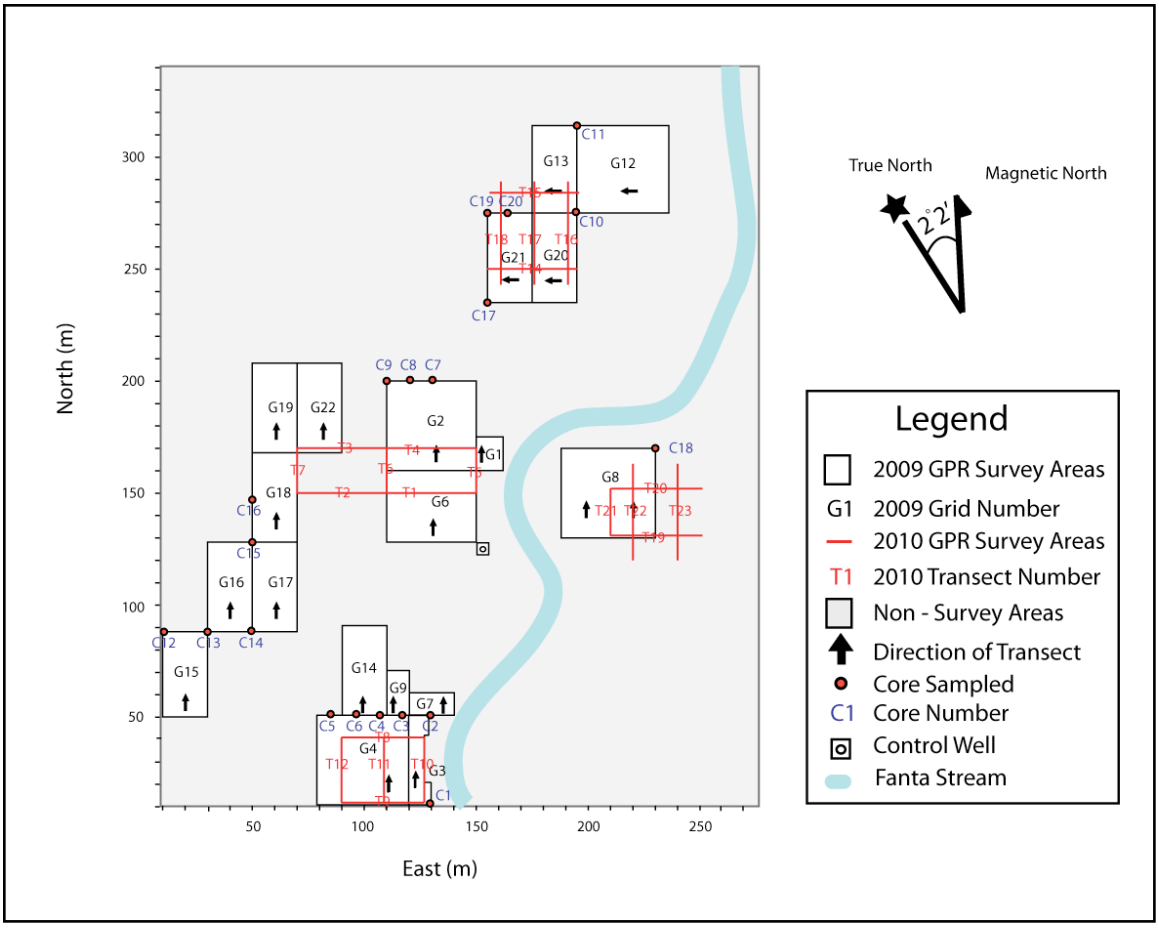

Figure 3.2: Location of survey grids and cores taken at the Fanta site.

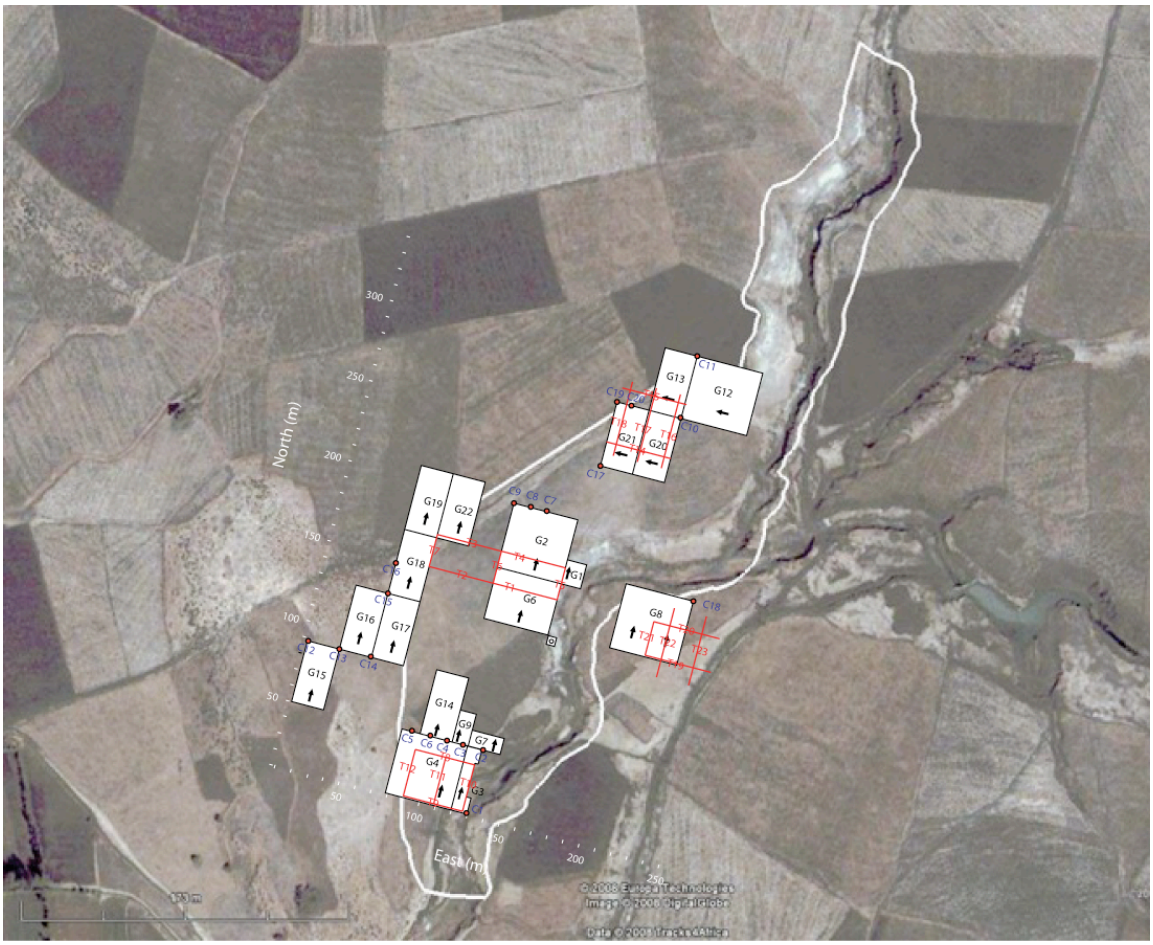

Figure 3.3: Overlay of GPR survey grids and core locations on original site delineation by Bobe and Assefa (2008).

Table 3.1: GPR Grid Parameters. Note that Grids 5, 10, 11 and 23 were collected with the 500 MHz antenna which yielded no interpretable results and are not referenced in the site maps (Figs. 3.2 and 3.3).

Grid	Ant. Freq. (MHz)	Size (m^2)	UTM Northing+	UTM Easting+
1	100	180	478071	981877
2	100	1600	478010	981871
3	100	400	477867	981513
4	100	1600	477825	981516
5	500	400	477836	981520
6	100	1280	478002	981631
7	100	280	477868	981554
8	100	1680	478029	981675
9	100	200	477853	981552
10	500	900	478030	981676
11	500	380	478067	981715
12	100	1600	478055	981787
13	100	800	478013	981791
14	100	800	477850	981553
15	100	800	477849	981595
16	100	800	477871	981629
17	100	800	477850	981627
18	100	1040	477910	981674
19	100	800	477912	981711
20	100	800	477990	981757
21	100	800	477966	981752
22	100	1040	477965	981709
23	500	264	478068	981742

+ GPS coordinate taken at SW corner of each grid. Collected using WGS 1984 datum UTM Zone 17N.

Various required set – up parameters were input into the GPR system before data collection began. The run mode was set to 'continuous,' which allows for user – defined marks to be taken at a given interval. This method was employed because there was no survey wheel connection compatibility with the 100 MHz antenna. As the antenna was towed across the ground surface, whoever was deploying the antenna marked the survey at the beginning and end of each transect as well as at every meter, marked by plastic flags placed along a taper measurer. Each navigation mark was generated when the center of the antenna crossed each flag. This creates a degree of user error in horizontal spacing, based on the accuracy of the defined user – marks. However, resampling the data during the post – processing phase allows for a consistent horizontal scale to be fixed for each radargram.

On 'continuous' run mode, the control unit collects data at the number of scans per second sampled (GSSI, 1995b: 33). Using this setting, the antenna was continuously pulled across the ground along a meter - tape or flagging tape at known intervals and distances. This is the fastest mode of data collection, where the antenna was consistently moved across each transect at a constant walking speed. The scans per mark setting was fixed to 32, this was automatically set in the system using 'automatic' set – up parameters. Since navigation marks were collected at every meter (at 32 scans per meter), each scan was collected at every 3.125 cm horizontal distance. The scan value relates to the 'samples per scan' setting, which is the number of data samples in a vertical scan. This value is normally set to 512, which is an average value for most applications (GSSI, 1995a: 25). Although a value of 512 provides an extremely large digital dataset which takes up internal storage

memory, this is an important aspect for the survey in that it ensures the data is not under - sampled. The bit per sample parameter determines the dynamic range of the dataset. Data recorded at 16 bits has a more robust dynamic range but uses twice the disk storage space as 8 bit data (GSSI, 1995b: 26). Since data could be downloaded each night after data collection, the value was set to 16 bits to maximize resolution. This is important for GPR post – processing in the ability to image various subsurface features with a wide range of wave parameters.

The sample per scan calculation is important in considering the 'range' or time window of the GPR antenna. The range parameter is the time value in nanoseconds, and required adjustment based on the antenna frequency and the sought depth of penetration. This time window describes the two – way travel time (TWT) in receiving reflected signals after the systems generates a radar pulse (GSSI, 1995a: 20; Conyers, 2004: 85). With increased range, there is an increase in depth of viewing into the subsurface. A 250 ns range in TWT, was utilized throughout the majority of the project since it represents the 'normal' transmitting power at a relatively shallow depth of view for a 100 MHz antenna. This parameter was adjusted throughout the course of data collection, including the use of 500 and 150 ns range values. In all, the 250 ns window provided sufficient depth to image the deposits of interest at the site.

The position of the surface reflection or direct wave was recorded and relates to the time – zero position. This is a calibration that resolves the first reflection recorded from the ground surface. The position is set at the place in TWT where the radar pulse leaves the antenna and enters into the subsurface. This value

was adjusted manually to achieve a high – resolution direct wave measurement to calibrate the subsurface reflections. Selecting a time – zero position was also achieved during post – processing procedures. Additionally, the 'effective time window' describes the range value minus the time – zero position. This value varied for each grid and was adjusted during post – processing for consistency.

Gain is a parameter that must be adjusted as it varies from one location to another. Initially, the antenna was deployed in random orientations across an entire survey grid before each grid was sampled for data collection. This was done so that maximum amplitudes were regained for best fit on the oscilloscope display of the control unit during data collection. Gain is defined as giving rise to a change in signal amplitude or power from the system input to output (GSSI, 1995b: 22; Sheriff, 2006: 156). The adjustment of gain in the GPR system provides gain control, used to compensate for the variations in signal input strength. Using the automatic gain function in the SIR – 2 System was a first step in defining the gains for the survey. After viewing the automatic adjustments, the author used the manual gain mode to refine the set gain functions. This way, changes in soil moisture, changing ground surface conditions and various depths of reflectors can be adjusted in the field to ensure the best gain control before processing takes place (Conyers, 2004: 93). Using 5 gain points (or time position – dependant locations along the oscilloscope display with which to control waveform amplitudes), the gains were adjusted so that they center at 75% the width of the oscilloscope display; the recommended orientation of gain display appearing on the control unit (GSSI, 1995b: 22). Since deeper reflections require more amplification and gain adjustment in the lower

portion of the radargram, the SIR – 2 applies a time – varying gain (TVG) curve to account for this phenomena (GSSI, 1995b: 22). Increasing the linear or exponential gain factor in GPR SLICE ® v7.0 during post – processing can additionally add continuous gain to deeper reflections. Throughout this study, gains were generally consistent for each surveyed grid during data collection, with only minor adjustments applied during post - processing.

The spacing was selected at 1 meter intervals for the 100 MHz antenna in order to provide horizontal control with overlap. This provides sufficient coverage based on the Fresnel zone calculation completed earlier in this Chapter. This is considered a default interval for most archaeological GPR surveys (Garrison, 2003: 78). Each profile was automatically saved onto the control unit hard drive, later downloaded on a computer for storage and processing.

Survey Procedures: 2010 Season

In 2010, a second visit to the Fanta site allowed for additional data collection. During this time, the goal of the survey was to provide data during a different seasonal cycle, this period having dryer conditions at the site. At this time, the ground surface was not plowed; a potential benefit of having more uniform surface conditions than in 2009, which was just before the beginning of the rainy season. Conditions were wetter and the surface was extensively plowed at this time. The 2010 survey occurred in March, during which was an extremely dry period for the site where no farming practices were taking place. It was hypothesized that this survey would provide better results due to drier environmental conditions. This is

due to the fact that drier sediments do not have the conducting capacity of wet sediments and allow for generally deeper penetration.

The same surveying procedures were followed as the 2009 survey expect for the data transect spacing and geometry. Here, single transects were collected across the site and intersected as fence diagrams or isometric fence diagrams, as opposed to the grids collected in 2010. This allowed for faster data collection while providing a second trial to the previously collected lines. GPS coordinates of the starting and ending location of these transects are documented in Appendix B.

GPR Processing

The primary objective of GPR processing is to produce high – resolution profiles and amplitude time slices in order to visualize subsurface features at the Fanta site. Processing procedures for the Fanta transects and grids follow standard techniques in GPR processing. A number of steps are involved in the processing method. Goodman, 2010 and Cassidy, 2009 provide an in – depth review of GPR processing procedures similar to those utilized by the author. The various processing procedures are summarized in Figure 3.4, which shows the workflow involved in achieving GPR imagery. Throughout the creation of all GPR images, processing steps were completed systematically and consistently to ensure an accurate correlation of results between grids and profiles.

After each day of data collection, .dzt files collected by the GPR were downloaded onto a personal computer for processing, archiving and storage. This was an extremely time - consuming process since the files were collected at the

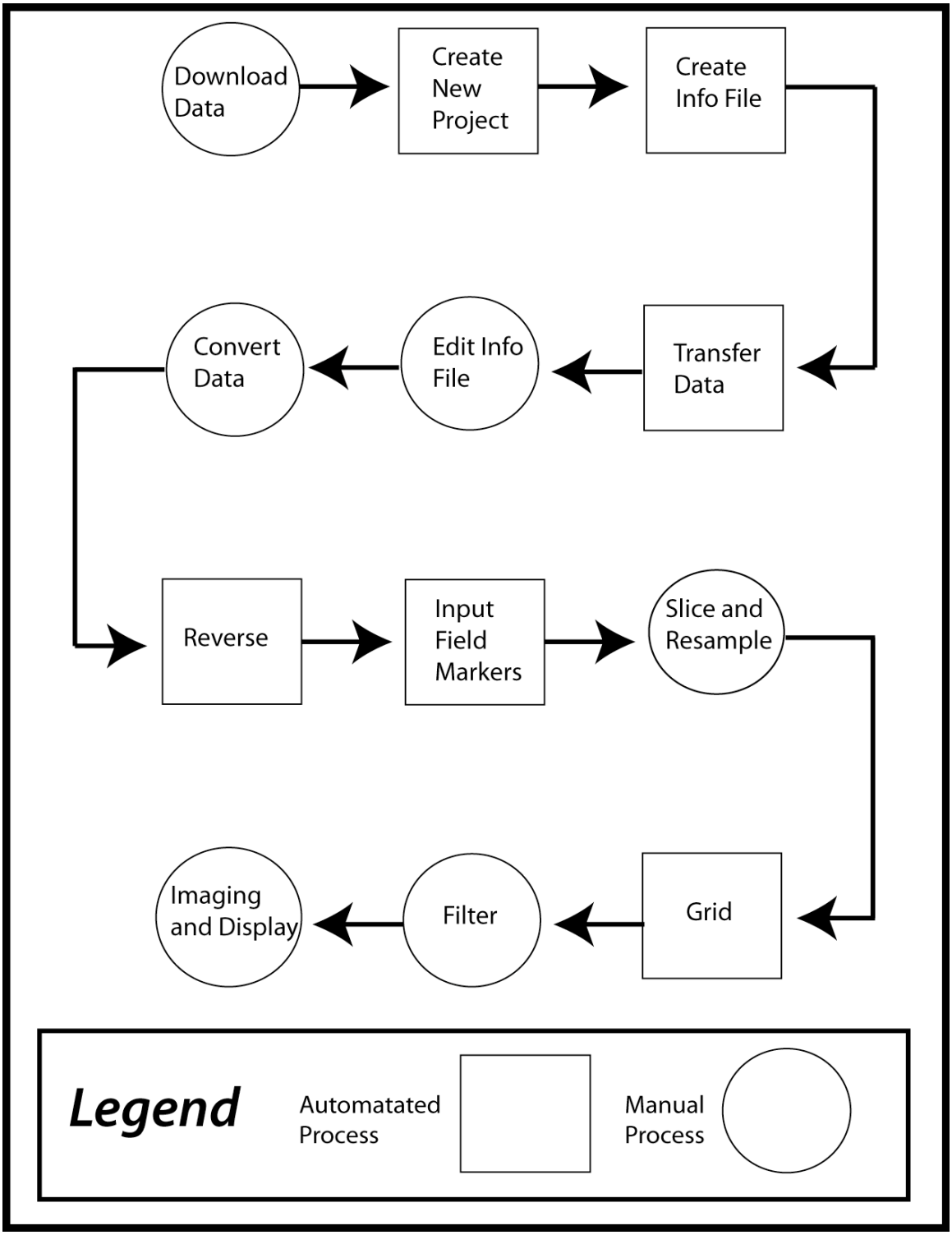

Figure 3.4: GPR processing workflow

highest possible resolution (as 16 bit data), and several grids were surveyed each day. Once the files are downloaded, processing began using GPR SLICE ® version 6.0 for the 2009 survey and 7.0 for the 2010 survey. Data was reprocessed for the 2009 survey on GPR SLICE ® v7.0 to ensure homogeneity of the data visualizations. GPR SLICE ® is a complete imaging and signal processing software package that has a built – in user interface that allows for ease of workflow in radar analysis.

The first step in the processing workflow was to create a new project. Each grid had its own project, denoted by the number of the grid or transect. Information files list the name of each file and the location of each radargram across a site. Files were edited to include directional information regarding each transect, whether it is reversed or collected in a fence diagram configuration. File lengths as well as starting and ending positions of each radargram were edited in this mode. Converting data from GSSI format (.dzt) to a format that allows for manipulation in GPR SLICE ® is an additional step in the processing workflow. In this menu, gains were adjusted for each radargram and applied to the entire dataset. The DC – drift component or wobble noise is also eliminated during this process. Drift effects commonly occur in geophysical data and are due to changes in the background magnetic or electrical fields as well as the instrument itself (Milsom, 1996: 14). After this procedure, files can then become reversed for transects collected in the reverse direction. The navigation was set by inputting hand – markers collected during the survey. Extra and missing markers in the dataset were accounted for and edited during this time. Field markers are automatically searched and input by GPR SLICE ®, and the detection and adjustment of navigation errors can be accounted for

during this processing procedure. Marker errors can occur due to a variety of reasons, including human error in correctly documenting numerous transects and grids in their respective locations. It is important to note the significance of keeping detailed field notes outlining the length of each line and transect within a grid. Throughout the surveys completed, markers were added at the beginning and ending of each line, including every meter in between. This allowed sufficient horizontal control and is a suitable scale for the 100 MHz antenna. Before usable data can be generated, marker navigation must be completed with no marker errors (Goodman, 2010: 57), this is because GPR analysis requires accuracy in spacing between radargrams and lines and subsequent radargrams in order to produce useful processed images in profiles and time slices.

Amplitude Time Slices

Slicing and resampling the data are the main processing steps and the heart of GPR – SLICE ® operations, where time slice datasets are created from radargrams (Goodman, 2010: 28). Time slices are composite images of collected radargrams and are used to highlight localized features over a gridded area. Confirmation of the ground – surface or 0 ns reflection from the direct wave is the initial step in creating time slices. It is important to verify this parameter so that each profile has the same 0 ns starting point. The effective time window is based on setting this parameter manually. Calculating this value allows an 'effective time window' to be determined (Goodman, 2010: 29):

$$Effective\ Time\ Window = \frac{T(N - N_0)}{N} \qquad (7)$$

Where T is the recorded time window, N is the recorded samples per scan and N_0 is the sample at 0 ns position. Solving for this equation gives:

$$Effective\ Time\ Window\ (ns) = \frac{250\,ns(512 - 49)}{512} = 226\ ns$$

The effective time window is actual time – depth that the GPR can record, accounting for travel time to the direct wave or surface reflection. This is a shorter depth than the 250 ns preset range input on the GPR system and was accounted for during post – processing procedures. The time 0 ns setting may change during each transect since the subsurface velocities are changing frequently, however GPR SLICE ® allows a continuous 0 ns starting point which is set for an entire grid.

The thickness and number of time slices is also decided at this point, as well as the type of spatial interpolation method: inverse distance or kriging. The thickness of each time slice was set so that there was sufficient overlap with which to connect potential anomalies and allow for smooth transitioning during time slice animations. This thickness varied over each grid in experimenting with best possible visualizations. Throughout the course of this project, generally 20 time slices were generated for each grid at roughly 25 ns thickness. The use of the inverse distance gridding method allowed for faster processing time compared with kriging, and was utilized for all time slices in the dataset. Inverse distance

interpolation provides an estimation between surrounding data points using a distance weighting exponent given as (Goodman, 2010: 62):

$$Estimated\ Data = w_1 z_1 + w_2 z_2 + \ldots w_n z_n \qquad (8)$$

Where $w_i = 1 / h^a$ and h is equal to the distance between the nearby point and the point on the grid to be estimated, a is the smoothing factor (set to a default value of 2) and z is the radar reflection strength of the point to be interpolated. Inverse – distance weighting is the spatial interpolation method most – used by GIS analysts, and estimates unknown measurements as weighted averages over known measurements, giving the greatest weight to the nearest points (Longley, et al., 2005: 333 – 334). Kriging is a geostatistical method which involves the interpolation of spatial data between locations of known values, using a linear combination of weights based on a model of spatial autocorrelation (Longley, et al., 2005: 336; Sheriff, 2006: 202). Despite the 'slightly' higher resolution provided with kriging, the inverse distance method can be used effectively with most datasets (Goodman, 2010: 39) in producing smoothed time slice maps.

Grid filtering in an option in GPR SLICE ® that applies noise removal to time slices, just as similar filtering options are applied to radargrams. Using vertical and horizontal background filters throughout time sliced data allows a smoothing of the amplitude values across the radargrams to provide a filtered image. The filters compute an average value over the filter length set by the user. This value is then subtracted from the center of the line filter. It is useful in removing striation noise

and mosaic patterns in time slice data where alternating horizontal high or low amplitude banding noise appears across time slices in the direction of the antenna transect (Goodman, 2010: 66).

Radargram Filtering

The process of filtering was critical in achieving the highest quality data images for display and visualization possible. There are many options available in GPR SLICE ® for filtering a dataset. This includes: migration, Hilbert transform, background filtering, boxcar filtering, band – pass filtering, spectral whitening, regaining and deconvolution. The first step in the filtering workflow was to apply a background removal filter. This is possibly the most commonly used filter in GPR data (Sharma, 2002: 142). In this process, the average scan is subtracted form each individual trace within the radargram (Conyers, 2004: 123; Goodman, 2010: 158). This was used to remove horizontal banding noise and was set from sample start to end for all radargrams to ensure consistency in the dataset. Horizontal banding noise can be a result of radio or other electromagnetic interference and antenna ringing, and can mask important subsurface reflections. These are known as 'multiples', which are caused by radar energy being reflected multiple times, producing erroneous data. Virtually all radar data contains the interference by some multiples (Sheriff, 2006: 238). The background removal filter sums all amplitudes of reflections recorded at the same time and divides by the number of traces summed, this is then subtracted from the dataset, displaying only the non – horizontal reflections (Conyers, 2004: 124). Background filters, however, can be problematic

as they can remove reflections caused by continuous flat – lying reflectors, interpreted as horizontal bedding (Conyers, 2004: 124; Cassidy, 2009: 154; Goodman, 2010: 158-159). Raw radargrams were examined before background removal filter application in order to emplace quality control over the data.

Additionally, band – pass filters were applied in order to remove high and low frequency noise that appeared in the dataset. This technique provides a frequency domain or vertical filter. Low – pass filters allow low – frequency components of the data to remain, and is suitable for eliminating high frequency noise by providing an aid in noise reduction. This is similar to the background removal filter application. High – pass filters allow only the high frequency components of the signal be recorded. This aids in the reduction of signal drift and low frequencies. The combination of both low and high – pass filtering allows a specific range of frequency components defined as a 'pass region,' in which specific trace frequencies are permitted. Finally, deconvolution filters were applied to thr data in order to achieve an enhanced image with well – defined reflections. Deconvolution is a temporal, inverse filtering process used to improve resolution by compressing the recorded wavelet into a narrower form. This is used to remove the source wavelet and leave only the impulse response from subsurface layers (Cassidy, 2009: 158). Additionally, deconvolution nullifies objectionable effects of other filtering actions and improves resolution and recognition of reflected events (Sheriff, 2006: 80). Thus, this process can remove adverse effects to other filtering methods and restore reflections that are masked by multiples and near surface reverberations (Sharma, 2002: 142). The combination of these filtering options was

utilized throughout this project, and the steps taken in documenting the response of different filters on radar wave properties are documented in Chapter IV of this Thesis.

Data Visualization

Generally, the data quality varies between the 2009 and 2010 surveys. Noise was present throughout much of the raw data and the application of filters was essential when performing interpretations of the site for both 2009 and 2010 datasets. In most figures, the raw radargrams are presented in order to show the processing steps and resulting outcomes. Each dataset required differing set – up parameters before initializing data collection. Factors such as sample selection, gain factor (linear, exponential), color table and color transform (linear, cosine, square root, etc.) affected the visual appearance of radargrams and time slices presented throughout this Thesis. For all radargrams and time slices, data is displayed utilizing a 'linear' color transform. This applies a black and white transform (Fig. 3.5) to linescan radargram displays and a 'rainbow' color bar for the time slice maps (Fig. 3.6) at equal amplitude intervals. 'Cosmetic' differences in data presentation greatly affect the image quality and display, and were consistent throughout profile and time slice data visualizations.

Time slice filtering greatly added to the interpretations of these data. Compared to radargram data, however, the time slice filtering involved minimal processing steps throughout. In producing final images, the data was saved in .jpg

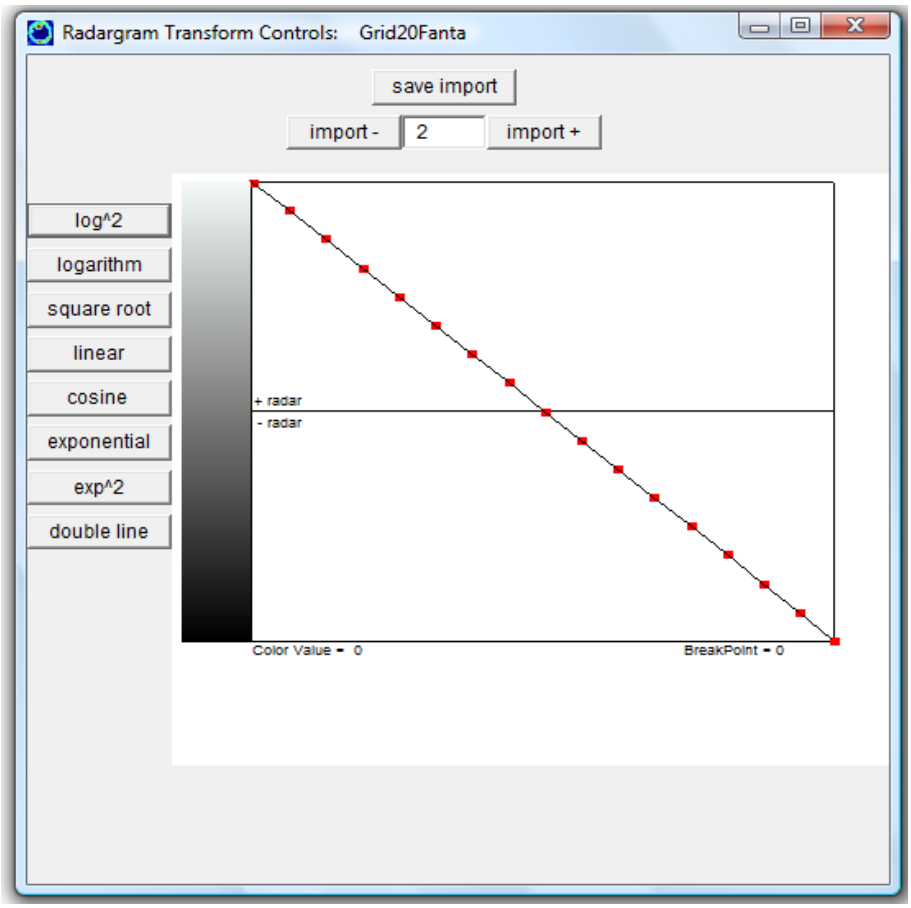

Figure 3.5: GPR SLICE ® color transform table. The linear color transform setting seen here was used in all variable density or linescan GPR profile visualizations.

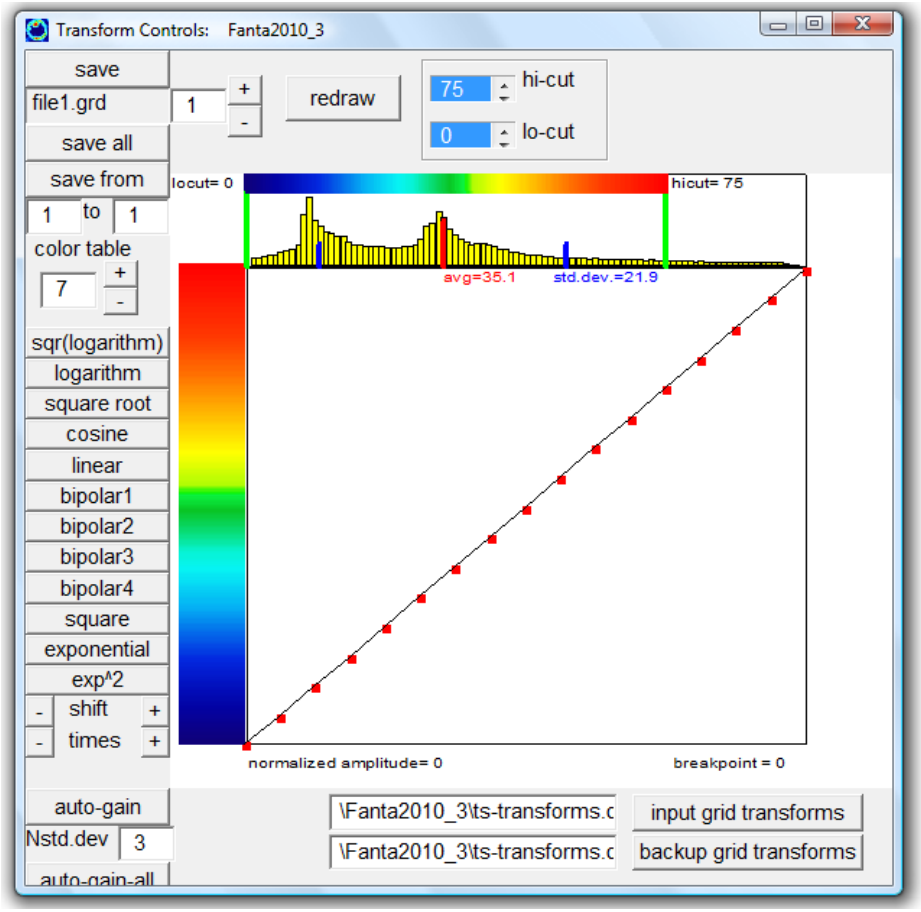

Figure 3.6: GPR SLICE ® color transform table. The linear color transform setting seen here was used in all GPR time slice visualizations.

format from GPR SLICE ® and edited first in Adobe Photoshop CS3 ®, where the header information was removed. These images were then brought into Adobe Illustrator CS3 ® where they were aligned for consistency and labeled for easy identification. Interpretation of the radargrams and the creation of an index map was also added using Adobe Illustrator CS3 vector tools, in order to clarify the location of each transect and grid with reference to the control well. The line drawings follow dominant (maximum) positive amplitude values at various depths, where reflections occur. Data interpretation was performed on both line – scan and wiggle displays. Not all amplitude values are included in the interpretation of subsurface features, however, generally the maximum positive amplitudes were interpreted and mapped as stratigraphic contacts and internal stratigraphic variations. The author was particularly judicious in deciding which values represented earth materials or were generated by signal interference and noise.

In EM surveying, noise can be generated through a variety of mechanisms. This includes interference from power lines, electronic equipment in the vicinity, atmospheric electrical discharges or low – frequency metallurgic phenomena. Circuit noise also exists and is caused by the randomization of conduction electrons, modulation noise, discreteness of magnetic transitions and the discreteness of charge carriers in semiconductors (Sheriff, 2006: 245). Some of this noise is apparent in the radargrams, specifically with raw data, which is why multiple filtering options were weighted in establishing images to interpret. Noise in the data was assessed in line – scan view, and could be seen more readily than in the wiggle displays. Understanding geological phenomena at the site through coring and cut

bank exposures allowed for ground control while interpreting radar data. Collected data is generally zero phase (Jones, personal communication, 2011), where reflections appear on the peak amplitudes on the wiggle display. However, phase shifts commonly occur in EM surveying since the position of the source radiation generated in the antenna will vary along the length and position across the antenna (Daniels, 2009: 108). Considering the effect of depth resolution error ranges from 10 – 15 % or greater, this likely will not effect the interpretations presented in this study.

Time – Depth Relationship

Perhaps one of the most difficult concepts in the ability to utilize GPR is constraining the time – depth relationship. Radar profiles are collected and processed in two – way travel time (TWT), and are displayed throughout this study in units of nanoseconds. The conversion of time to depth is needed for realistic interpretations, especially when collecting high – resolution data required to provide information about the shallow fossil unit at Fanta. This is a product of the velocity of the radar waves, or the time it takes for GPR waves to propagate and return to the antenna. Different earth materials cause differences in the velocity of the wave propagation, however, calculating an average velocity for shallow investigations is commonly performed as an industry standard (Jones, personal communication, 2011; Schneider, personal communication, 2011) and is seen frequently in contemporary GPR literature (Conyers, 2004: 103; Cassidy, 2009: 158). Considering velocity changes through each sediment or rock type, average

velocities create an acceptable model with which to provide an accurate time to depth correlation. Comparing collected data with theoretical values provides control and serves as a good proxy with which to compare field data.

Depth conversion can be done in a multitude of ways. This includes common midpoint (CMP) analysis (GSSI, 1995a: 47; Cassidy, 2009: 159), hyperbolic velocity analysis (GSSI, 1995a: 47; Sharma, 2002: 314; Conyers, 2004: 115-116; Cassidy, 2009: 159; Goodman, et al., 2009: 484; Goodman, 2010: 160), estimating velocity from the dielectric constant (GSSI, 1995a: 44; Conyers and Goodman, 1997: 134) and locating an object at known depth (GSSI, 1995a: 45; Conyers and Goodman, 1997: 110; Conyers, 2004: 102). Table 3.2 shows approximate velocities for the various sediments at Fanta, which were used in establishing theoretical velocity values for the site. Considering that CMP and hyperbola matching analysis produce errors in velocity control in upward of +/- 10 %, using an average velocity will generally produce the similar interpretational results (Cassidy, 2009: 159). The attempt to use multiple methods was made throughout this study in the estimation of velocity.

Depth Calibration and Velocity Analysis

Of major importance in any GPR study is to constrain the time to depth conversion of vertical depth from nanoseconds to meters (Cassidy, 2009: 158 – 159). Meeting this objective is critical in determining an accurate velocity model and establishing depth control. There are many different ways to perform this analysis that can be used in calculating an average velocity for the entire survey.

Table 3.2: Approximate velocities of materials at the Fanta Site (Modified from GSSI, 1995a: 21).

Material	T (m/ns)
Clay	0.039
Volcanic Ash	0.043
Conglomerate	0.065
Gravel	0.065
Weathered Volc. Rock	0.053

An understanding of the stratigraphy at the site was an important factor in generating an established velocity model for the GPR data. Since clay is capping the bone bed and subsequent stratigraphic units, the effect of signal attenuation and loss of suitable depth to penetration was of large concern. This is due to the attenuation effects of clay materials that cause potentially problematic results for radar (Hayakawa and Kawanaka, 1998: 38; Saarenketo, 1998: 73). Attenuation is a reduction in amplitude or energy caused by the transmitting media (Dobrin and Savit, 1988: 46 – 47; Sharma, 2002: 311; Conyers, 2004: 49; Neuendorf, et al., 2005: 43; Sheriff, 2006: 23; Cassidy, 2009: 144). As the radar pulse is subjected to geologic media, it suffers from attenuation effects as a result of absorption, dispersion, scattering and spherical divergence (Neuendorf, et al., 2005: 43; Neto and Medeiros, 2006: 140). Additionally, the high dielectric constant value for volcanic ash and tuffaceous sediments may also cause attenuation effects due to the silty matrix of the material and highly conductive nature of the deposits (Russell and Stasiuk, 1997: 518; Tohge, et al., 1998; Rust and Russell, 2000: 24; Edwards, et al., 2000: 223; Gomez – Ortiz, et al., 2006: 63; Gomez, et al., 2009: 120). The effect of signal attenuation can be evaluated by performing velocity analyses.

Aside from the potentially adverse effects of the conductive nature of stratigraphy on the GPR signal, the consideration of the water – sediment interface is an additional concern that needs to be considered when evaluating the effectiveness of the velocity analysis (Saarenketo, 1998: 73 – 74; Conyers, 2004: 101; Lunt, et al., 2005: 255; Pyke, et al., 2008: 335). Areas with increased water

content can fluctuate in depth dramatically due to changes in drainage location, stratigraphy and surface topography (Conyers, 2004: 101). Coring data confirmed that there is an increase in water content of the sediments at depth, however, the sediments are largely unsaturated and at a shallow depth (< 2 meters) most likely does not represent the water table. This zone observed throughout coring analysis most likely represents a capillary fringe. This is the lower subdivision of the unsaturated zone, immediately above the water table and held by surface tension (Neuendorf, et al., 2005: 96). The stream channel contained small, isolated water pockets and was not discharging at the time of the survey (Figs. 3.7 and 3.8). These complex phenomena led to a robust pre-processing assessment of an estimation of velocity values at the site.

Bar Test: 2009

The first attempt to perform a depth calibration was by employing a method that involves the recording of depth to a known reflector. This way, the estimation of subsurface velocity can be calculated using (GSSI, 1995a: 45):

$$V = \frac{D}{TWT/2} \qquad (9)$$

Where V is equal to velocity, TWT is the two – way travel time and D is depth of the metal object that gives rise to a reflection. The depth of unknown targets can thus be estimated using (GSSI, 1995a: 45; Conyers and Goodman, 1997: 111):

Figure 3.7: Photograph showing isolated water pockets within the stream channel at Fanta.

Figure 3.8: Photograph showing isolated water pockets within the stream channel at Fanta.

$$D = \frac{TWT}{2} \times V \qquad (10)$$

In evaluating the depth component, the application of rebar (iron bar used in concrete reinforcement) served as a point source and was placed at a known location and known depth and inserted into the stream cut bank exposure. The GPR antenna was then slowly pulled over the bar while subsurface reflections were recorded. This is also known as the 'bar test' (Conyers and Lucius, 1996: 27; Conyers and Goodman, 1997: 110; Chow, et al., 2006: 186), where a metal reflector is used in determining velocity values. Because radar antennas emit electromagnetic waves in a broad cone, the expected resulting anomaly should be a steeply – curved reflection, commonly known as a reflection hyperbola (Conyers and Lucius, 1996: 27; Conyers and Goodman, 1997: 111). A hyperbola describes a conical shape that is made up of an apex and two limbs or branches that mirror each other dimensionally, and results from radar energy reflections or diffractions. Surface scattering effects of the GPR signal generally resemble a hyperbolic move out, which degrades the visibility of reflections and potentially causes interpretation pitfalls (Nuzzo, 2003: 533 – 534). A synthetic hyperbolic reflection is shown in Figure 3.9 in order to visually clarify the geometry of the expected reflection pattern due to a buried spherical object.

The iron – reinforcing bar used in this study has dimensions of 1 meter in length by 2.5 cm diameter. The entirety of the rod was hammered into the cut bank exposure and can be seen in Figure 3.10. A GPR transect aligned perpendicular to

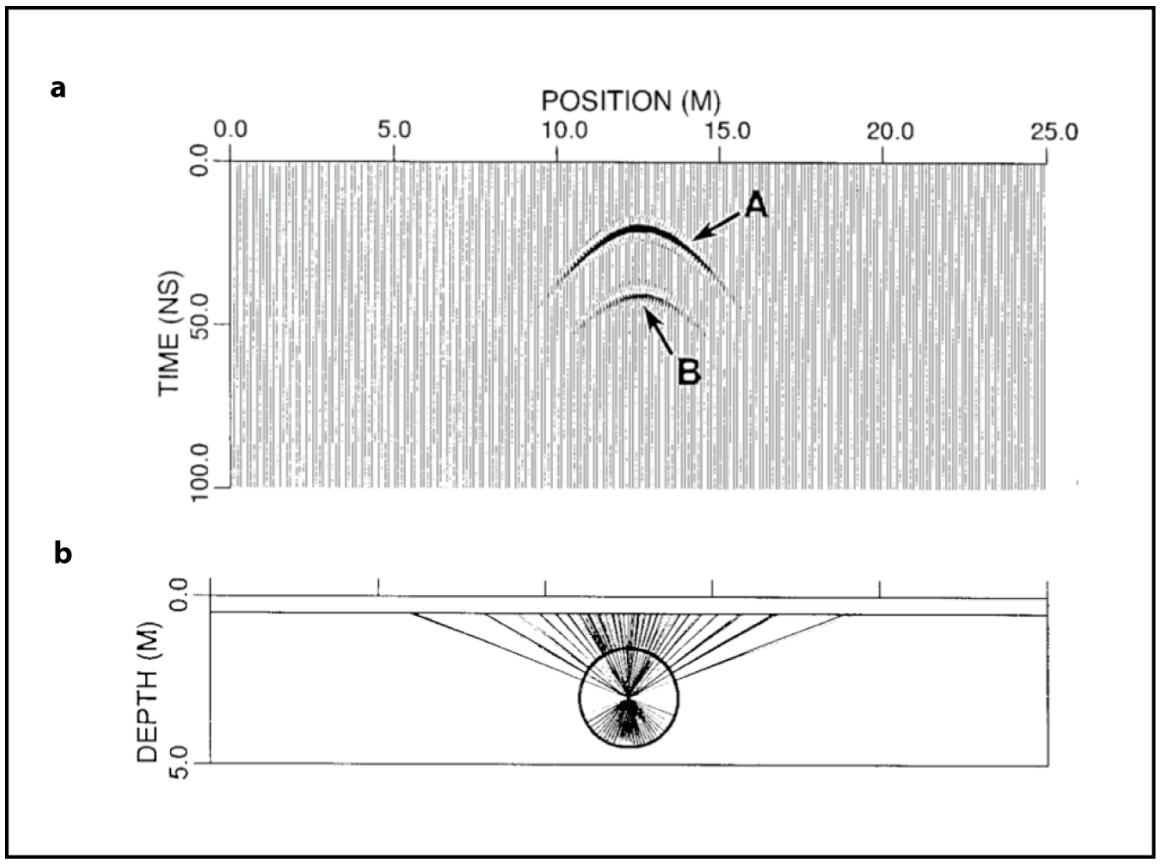

Figure 3.9: Synthetic hyperbolic reflection pattern in GPR imaging. (a) Two hyperbola here represent the top (A) and bottom (B) of a modeled, buried spherical object. (b) Interpretation of synthetic ray tracing at the point location. (Modified from Zeng and McMechan, 1997: 798).

the length of the bar was recorded several times in order to attempt the detection of a point source hyperbola. Careful attention to the radar reflection pattern went underway when interpreting the GPR data. Reflection and diffraction hyperbola commonly occur in the GPR files, and can be filtered using the migration technique, as these can be artifacts in the data created from surface or subsurface wave scattering or diffractions (Nuzzo, 2003: 534; Goodman, 2010: 160). Diffraction hyperbolas are also characteristic of GPR data collected from highly heterogeneous sediments and are a source of noise in the data (Vandenberghe and van Overmeeren, 1999: 248). This problem is especially pervasive for low frequency antennas, which are more prone to unshielding issues.

The depth calibration was completed in Grid 3, Transect 11. In this trial, the rebar was placed at 40 cm vertical depth, and is approximately at the contact of clay and uppermost ash unit (Fig. 3.10). Profiles seen in Figure 3.11a and b show a high amplitude feature that resembles a broadly shaped hyperbolic reflection that occurs at roughly 22 ns depth. The linescan display (Fig. 3.11a) shows the raw, resampled data where the hyperbolic pattern is less visible due to horizontal banding that appears from 0 – 25 ns depth. The wiggle display (Fig. 3.11b) appears to have a reflection pattern that may relate to a hyperbolic feature. The dipping nature of the 'potential reflection apex' may relate to one arm of a hyperbola and its apex. Examining the time slice data may help to confirm the appearance of the hyperbolic reflection as a function of time. Figure 3.11c shows a time slice of the Grid 3 data from 18 - 33 ns depth. As seen in this Figure, a high amplitude anomaly is present at between 32 - 36 meters horizontal distance. For this test, a reflection feature was

Figure 3.10: Photograph showing the location of the 'bar test' depth calibration procedure completed in the 2009 survey, Grid 3. The metal rod is located at 40 cm depth at the contact of clay and ash units, and can be seen by the tape measurer reading. Note the 100 MHz antenna appears on the surface.

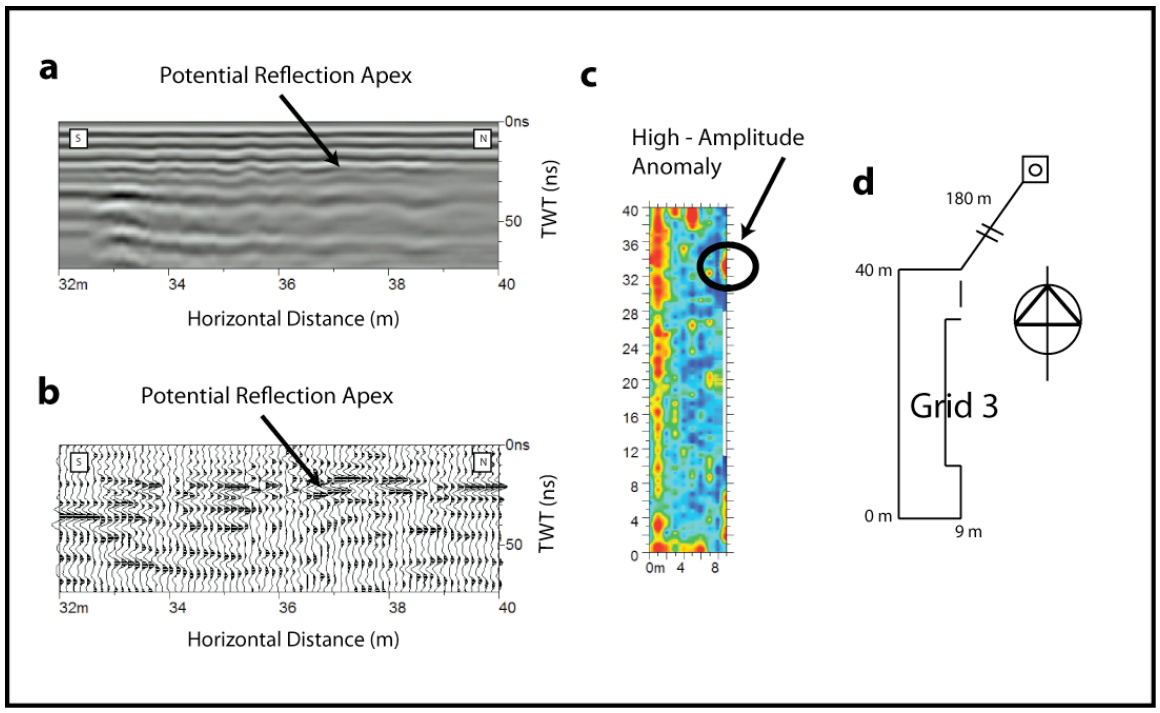

Figure 3.11: Bar test depth calibration analysis; Grid 3, 2009. (a) Processed, raw radargram showing the attempted depth calibration. (b) Processed, band – pass, background and deconvolution filtered data in wiggle display. (c) Time slice showing high amplitude anomaly that may be related to the buried metal object from 18 – 33ns depth. (d) Index map showing the location of the transect highlighted by a dashed line. Metal reflector is buried at 40 cm depth at a horizontal distance of 34.5 meters from south to north.

generated in the location of the buried rebar that resembled a hyperbolic moveout and was considered successful. It is expected that greater amplitude values would be associated with this feature in comparison to surrounding strata, which was apparent in the resulting radargram.

Using the depth of this reflector input into Equation 9, the following can be calculated (GSSI, 1995a: 45; Conyers and Goodman, 1997: 111):

$$Velocity = \frac{0.4\ m}{11\ ns} = 0.036\ m/ns$$

This calculation was used for achieving an average velocity value for the profiles in both 2009 and 2010 datasets. However, using additional methodologies was necessary in achieving confidence for this critical piece of the study.

Estimating Velocity from the Dielectric Constant (ε)

A theoretical calculation can be computed by estimating a velocity value from the dielectric constant. This is another way in which to attempt to approximate the time to depth conversion. Estimations on the dielectric constant can be predicted with published ε (dielectric constant) values found throughout GPR literature (GSSI, 1995a: 44; Milsom, 1996: 133; Conyers and Goodman, 1997: 33; Garrison, 2003: 77; Conyers, 2004: 47). This is useful in providing a theoretical velocity value with which to compare analytical results. Based on the sediments at Fanta, the approximate ε value of each stratigraphic unit at the site is outlined on Table 3.3. It

appears that sufficient contrasts in RDP exist with the Fanta sediments, enough to theoretically cause reflections in the data. Values from this table were normalized for sediment thickness to achieve a single ε value to use in the following equation (GSSI, 1995a: 44; Conyers and Lucius, 1996: 26; Conyers, 2004: 48):

$$V = \frac{c}{\sqrt{\varepsilon}} \qquad (11)$$

This results in an average velocity value of:

$$V = \frac{c}{\sqrt{\varepsilon}} = \frac{0.29\ m/ns}{\sqrt{19.71}} = 0.065\ m/ns$$

This value gives an estimation based on the normalized bed thicknesses and is comparable to velocity value generated from the 2009 bar test, despite its value being slightly higher. Considering the velocity of radar waves generally decrease with depth, this value provides a theoretical analysis of the site's sediments to be examined with caution regarding potential velocity changes.

Velocity Analysis Conclusions

Considering the variety of values achieved in the depth calibration techniques, data received from the bar test is likely to have the strongest confidence in approximating a realistic velocity value. Estimating the dielectric constant from established literature generated a higher velocity value, and due to the variable

Table 3.3: Table of Estimated RDP Values for Various Materials (Modified from: GSSI, 1995a: 44; Milsom, 1996: 133; Conyers and Goodman, 1997: 33; Garrison, 2003: 77; Conyers, 2004: 47).

Material	RDP
Air	1
Tuff	14
Silt (wet)	10
Conglomerate	6
Gravel	3 - 5
Volcanic Rock	8
Clay (dry)	5 - 40
Clay (wet)	15
Water	81

nature and water content of the conductive sediments at Fanta, a lower value is generally expected. All radargrams shown throughout the remainder of this Thesis will be assigned an average velocity value of 0.036 m/ns for both 2009 and 2010 data. This approximate value provides a reasonable constraint on the depth to lithological features seen in the radargrams and time slices.

Sediment Coring

A suite of cores was collected across the Fanta site in 2009 in order to test the GPR profiles with ground truth data at various locations away from the stream cut bank exposure. By coring, the author had the ability to test the presence and depth of the fossiliferous unit across the landscape at Fanta outside of the stream's cut bank. A 2-meter long extended hand auger with a 15 cm sampling bit was used to collect field samples in areas outlined in Figure 3.2 and Table 3.4. Cores were placed at various intervals away from the stream cut bank along surveyed GPR grids, and provided an excellent approach of testing stratigraphy in these areas while allowing minimal disturbance to paleontological and archaeological materials. Data from this analysis allows the spatial definition of sedimentary units at centimeter scale precision.

Table 3.4 and 3.5 document the results from geological coring. Grid locations are sometimes listed as multiples, since the cores frequently occur at the boundaries of multiple survey areas. The auger penetrated to a maximum depth of over 2 meters, therefore the depth required to reach the bone unit may not have been breached for some samples. Fossiliferous deposits may exist to greater depths than

Table 3.4: Core data from the Fanta Stream Site, 2009.

Core #	Grid Location	Depth	UTM North +	UTM East +
1	3	1.3 m	477874	981508
2	3	0.8 m	477877	981551
3	4,9	1.2 m	477866	981553
4	4,14	0.9 m	477860	981557
5	4,14	1.1 m	477837	981573
6	4	1.1 m	477849	981573
7	2	1.6 m	477970	981682
8	2	1.9 m	477955	981694
9	2	1.5 m	477939	981707
10	13	1.4 m	478015	981832
11	13	1.7 m	477993	981795
12	15	1.8 m	477848	981634
13	15, 16	1.8 m	477867	981636
14	16	2.0 m	477889	981630
15	16	2.1 m	477891	981673
16	18	2.1 m	477929	981710
17	21	1.7 m	477966	981757
18	11	2.1 m	478077	981724
19	11	2.0 m	478078	981744
20	11	2.1 m	478073	981745

+ Collected using WGS 1984 datum. UTM Zone 17N.

2 meters, however, the auger was noted to have breached penetration depth in some areas due to large boulder – sized materials within the conglomeritic unit (Figs. 2.3 and 3.12). This caused some sections to be recorded at less than 1 meter depth in some locations.

Figure 3.13 shows a three – dimensional illustration and interpretation of cores described in Table 3.4 and 3.5. Generally, core data shows the presence of the conglomeritic unit across varying areas to the central and northeastern part of the survey area. Strata at greater depths observed in the cut bank exposure do not appear throughout many of the cores. This includes volcanic bedrock, lower tuff deposits and to a large extent the lower clay unit. The upper clay capstone can be mapped in its entirety across the site, and extends to more than 2 meters (as seen in Core 18) in parts of the survey area. The uppermost tuff deposit was noted in most cores and ranged in thickness from 20 cm to over 1.5 meters.

Coring provides a ground truth in which to compare the GPR datasets, and serves to assist in further delineating the site for protection until an established excavation effort can be made. A synthesis of the results from these techniques is documented in the following Chapter.

Table 3.5: Detailed sediment core data from the Fanta Stream Site, 2009

Core 1	0-39 cm: black cotton soil 40 – 90 cm: black cotton soil, Fe concentrations, higher soil moisture 91 – 120 cm: volcanic tuff 121 – 130 cm: ash with clay
Core 2	0 – 70 cm: black cotton soil 71 – 80 cm: Enter conglomeritic layer mixed with volcanic tuff 81 cm: conglomerate, stopped due to large gravels/cobbles
Core 3	0 – 65 cm: black cotton soil 66 – 91 cm: volcanic tuff 92 – 110 cm: conglomerate 111 – 120 cm: clay
Core 4	0 – 70 cm: black cotton soil 71 – 85 cm: conglomerate 86 – 90 cm: volcanic tuff
Core 5	0 – 80 cm: black cotton soil 81 – 110 cm: volcanic tuff
Core 6	0 – 73 cm: black cotton soil 74 – 85 cm: volcanic tuff with redoximorphic features 86 – 92 cm: volcanic tuff, darker sediment color change 93 – 110 cm: volcanic tuff, increased water content
Core 7	0 – 70: black cotton soil 71 – 78 cm: volcanic tuff

	79 – 105 cm: volcanic tuff, coarsening 106 – 145 cm: volcanic tuff 146 – 150 cm: conglomerate with redoximorphic features 151 – 162 cm: clay
Core 8	0 – 39 cm: black cotton soil 40 – 75 cm: volcanic tuff 76 – 135 cm: volcanic tuff with gravels, redoximorphic features 136 – 190 cm: conglomerate
Core 9	0 – 55 cm: black cotton soil 56 – 70 cm: volcanic tuff 71 – 112 cm: conglomerate 113 – 145 cm: conglomerate with redoximorphic features and carbonate (?) nodules
Core 10	0 – 75 cm: black cotton soil 76 – 104 cm: volcanic tuff 105 – 140 cm: volcanic tuff, coarsening 141 – 145 cm: conglomerate, possible lithic debitage
Core 11	0 – 84 cm: black cotton soil 85 – 110 cm: volcanic tuff 111 – 177 cm: conglomerate
Core 12	0 – 113 cm: black cotton soil 114 – 152 cm: volcanic tuff, diffuse contact 153 cm: conglomerate, stopped due to cobbles
Core 13	0 – 100 cm: black cotton soil 101 – 130 cm: volcanic tuff mixed with clay

	130 – 165 cm: volcanic ash, lighter color change 165 – 175 cm: conglomerate, basalt fragments
Core 14	0 – 120 cm: black cotton soil 121 – 158 cm: volcanic tuff, coarsening downward 159 – 185 cm: conglomerate mixed with tuff, bone present 186 – 205 cm: conglomerate, coarser, possible lithic
Core 15	0 – 150 cm: black cotton soil 151 – 205 cm: volcanic tuff
Core 16	0 – 105 cm: black cotton soil 106 – 210 cm: volcanic tuff 211 – 230 cm: volcanic tuff with redox features
Core 17	0 – 30 cm: black cotton soil 31 – 170 cm: volcanic tuff
Core 18	0 – 210 cm: black cotton soil
Core 19	0 – 70 cm: black cotton soil 71 – 100 cm: conglomerate
Core 20	0 – 50 cm: black cotton soil 51 – 104 cm: conglomerate

Figure 3.12: Photograph of coring completed at the Fanta Site. As seen, field assistants struggled to penetrate past large cobble – sized fragments within the conglomeritic unit at the site.

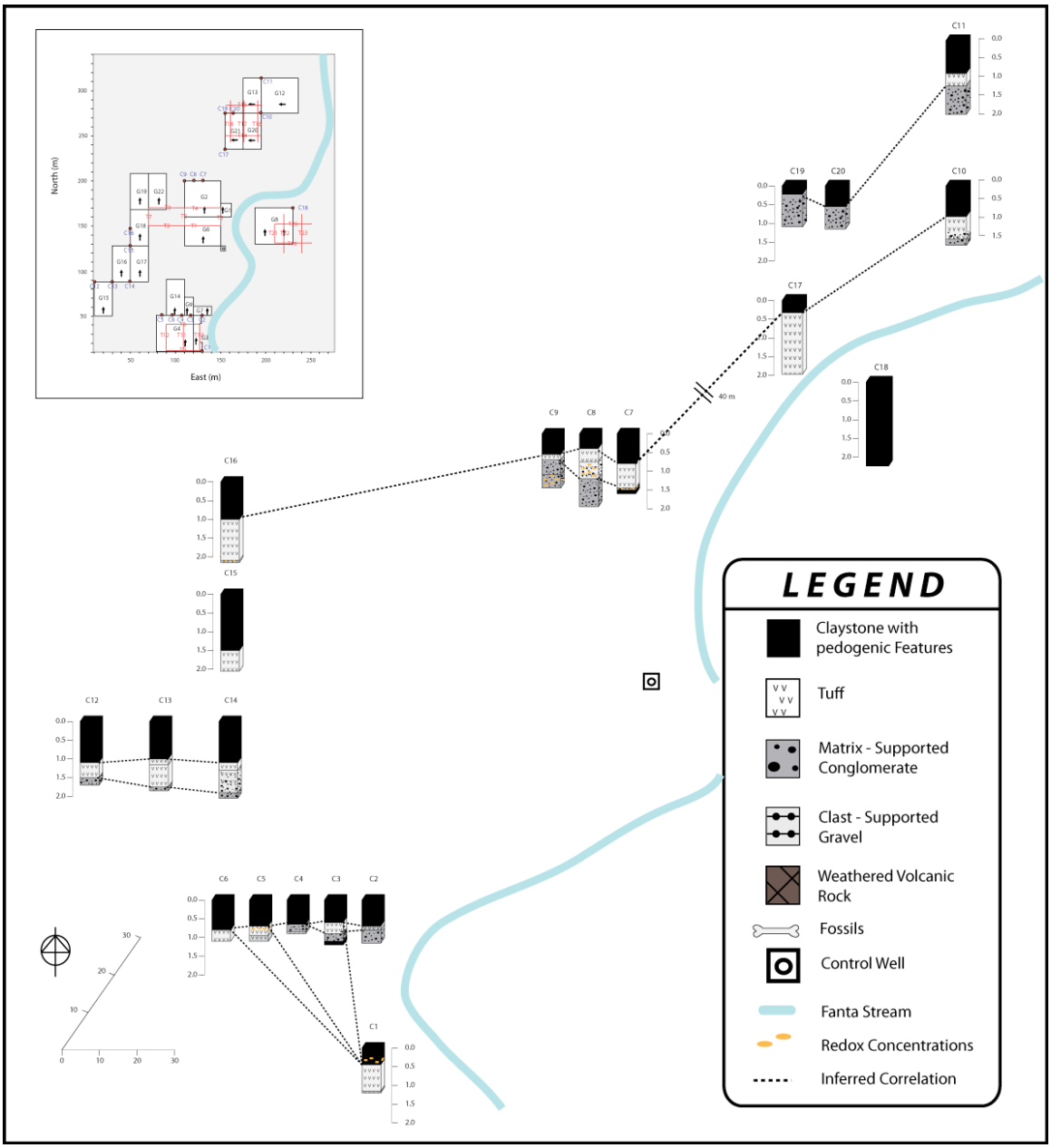

Figure 3.13: 3D core map showing locations of boreholes within the greater Fanta survey area.

CHAPTER IV

RESULTS

Data Interpretation

Once depth calibration was completed for the 2009 season, the critical investigation of interpreting reflection profiles went underway. The stratigraphy at Fanta as seen in GPR profiles is generally considered to generally represent a four – layer model of the subsurface (from Fig. 3.2). This includes the clay soil capstone, gravel and conglomerate units and well as volcanic ash. Other units such as weathered volcanic rock, a stratigraphically deeper tuff unit and clay appears at the bottom of the described section in Figure 3.2. These units were not interpreted in any of the GPR transects due to lack of sufficient penetration.

Two main characteristics of the GPR signal are present throughout the profiles. The first is characterized strong contrasts in highly reflective materials that generate laterally continuous, coherent reflection patters of high amplitude and high frequency. These reflection patterns represent GPR facies that were interpreted as clay and volcanic tuff, material that is generally fine – grained, homogenous and widespread throughout the survey area. The other wave pattern is typified by low reflectance or lossy materials that do not generate continuous subsurface reflection features of a considerable coherency. These weaker reflection surfaces are interpreted as gravels and conglomerates, materials that are coarse – grained and

heterogeneous at the Fanta site. These differences are visualized by the attributes of the reflected waves in terms of amplitude, frequency and coherency. Coherency is defined as a measure in similarity between more than two wave functions (Sheriff, 2006: 55) and generally follows a well – defined phase relationship.

In the case of strong subsurface reflections, there is a maximum amplitude associated with the peak or trough of the reflected wave that is generated at the interface of two stratigraphic depths with significant contrasts in RDP. These amplitudes, generated over a series of traces that stretch across the horizontal axis of the radargram, provide generally continuous reflections that are interpreted as stratigraphic contacts when correlated across the horizontal axis. Figure 4.1 shows an example of the major differences between the linescan and wiggle displays. Both of which are used to represent the Fanta data. In general, changes in amplitude values are partly responsible for the reflectors seen in the radargrams and in time slices. The respective amplitudes can be strong or weak, and at peak (positive) or trough (negative) positions depending on their associated values. Generally, when EM waves move across a material from a lower to a higher dielectric value, a positive maximum amplitude (or peak) is generated. Moving from a higher to lower dielectric value thus produces the opposite effect, and the reflection is generated on the maximum negative amplitude (or trough) (Jones, personal communication, 2011). Rapid changes in amplitude values are interpreted as contrasts in lithology. This is expressed as changes between RDP or ε values. These contrasts are shown throughout the GPR images.

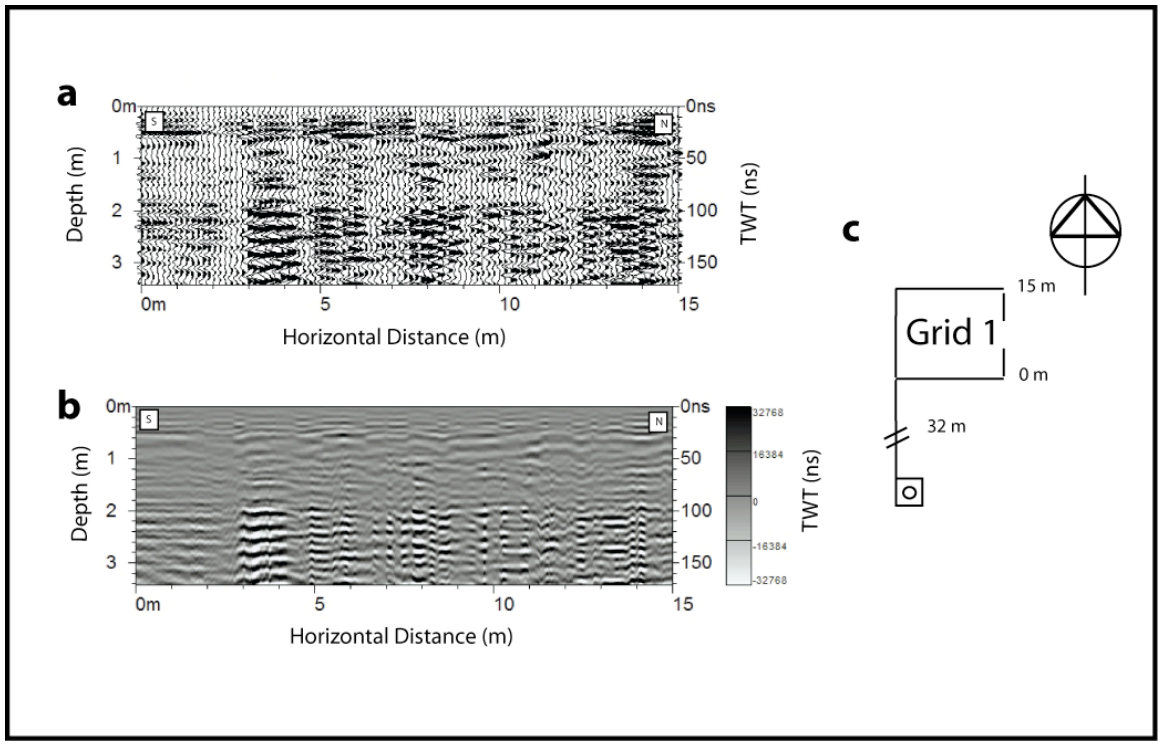

Figure 4.1: Background removal and band – pass filtered radargrams documenting differences in data visualization for interpretation. (a) Wiggle display. Here, the positive amplitude values are filled in with positive pulse or amplitude fill. (b) Linescan display. Data is displayed continuously. A legend to the right of the radargram describes that higher positive amplitude values are black in color and higher negative amplitude values are white in color (linear color transform [see Fig. 3.5]). (c) Index map. The dashed line indicates the position of the transect relative to the grid.

In general, horizontal banding noise is seen at the top of most raw profiles. This is a result of airwave interference in the dataset, commonly seen in the upper – most portions of radargrams. Airwaves are generated as energy that travels in the air at the velocity of sound (Sheriff, 2006: 8):

$$V \approx 1051 + 1.1F \ \ ft/s \qquad (12)$$

Where *V* is velocity and *F* represents Fahrenheit temperature. These interferences are possibly a result of the poor shielding response from the low – frequency 100 MHz antenna (Conyers, 2004: 77). Resulting waves are high amplitude and are visualized as horizontal, planar features that obscure meaningful reflections from the subsurface. The sequence of processing steps are seen throughout the figures presented below, beginning with the 2009 data series.

2009 Results

The 2009 GPR data covers over 19 km^2 of surveyed area. This is an extremely large region considering Ernenwein and Kvamme (2008: 134) describe a survey as 'large – scale' if it breaches 1 ha (0.01 km^2). Grids were arranged surrounding the stream as shown in Figures 3.2 and 3.3 in order to survey the site both inside and outside of the previously delineated area completed by Bobe and Assefa in 2008. No topographic correction of the data was required considering that only marginal elevation changes were noted across the site (less than 1 meter of relief was noted at any location in the area of interest). Figure 4.2 shows a photograph of the

relatively stable topography across the site. Take note of the plowed areas that appear between slightly elevated surfaces in the photograph.

Grid 1

Grid 1 was a test that surveyed previously known areas containing fossiliferous deposits. This grid displays control radargrams with which to model the results collected from the rest of the site. The closest profile to the exposed fossils was File 12, shown in Figure 4.3. Here, the interpretations of reflections can be seen in GPR records between 0 and 120 ns depth. Below this depth, noise has masked the GPR signal in the background and band – pass filtered data (low – pass: 114 MHz; high – pass: 20 MHz) (Figs. 4.3b and c), however some coherent reflections appear in the deconvolution filtered data in this radargram at greater depths beyond 100 ns (Fig. 4.3d).

The raw radargram contains horizontal banding noise at the top of the section (Fig. 4.3a) that was removed during applied background filtering (Fig. 4.3b). This banding noise was present throughout many of the GPR profiles and may be result of signal interference off of the complex plowed surface features (Fig. 4.2). As described previously, this radargram is interpreted based on the coherency of reflection patterns. The uppermost unit appears to be a shallow (under 1 meter in vertical depth), coherent high – amplitude and high – frequency wave pattern that is continuous across the profile. Directly below this, a lower amplitude and coherency event ranges from 1 – 2 meters depth. This is consistent with the depth of the bone bed. The volcanic tuff unit sits below this, as a high amplitude, highly coherent radar

Figure 4.2: Photograph that highlights the surface terrain at the site in 2009. Stakes marking the GPR survey grid corners are shown here.

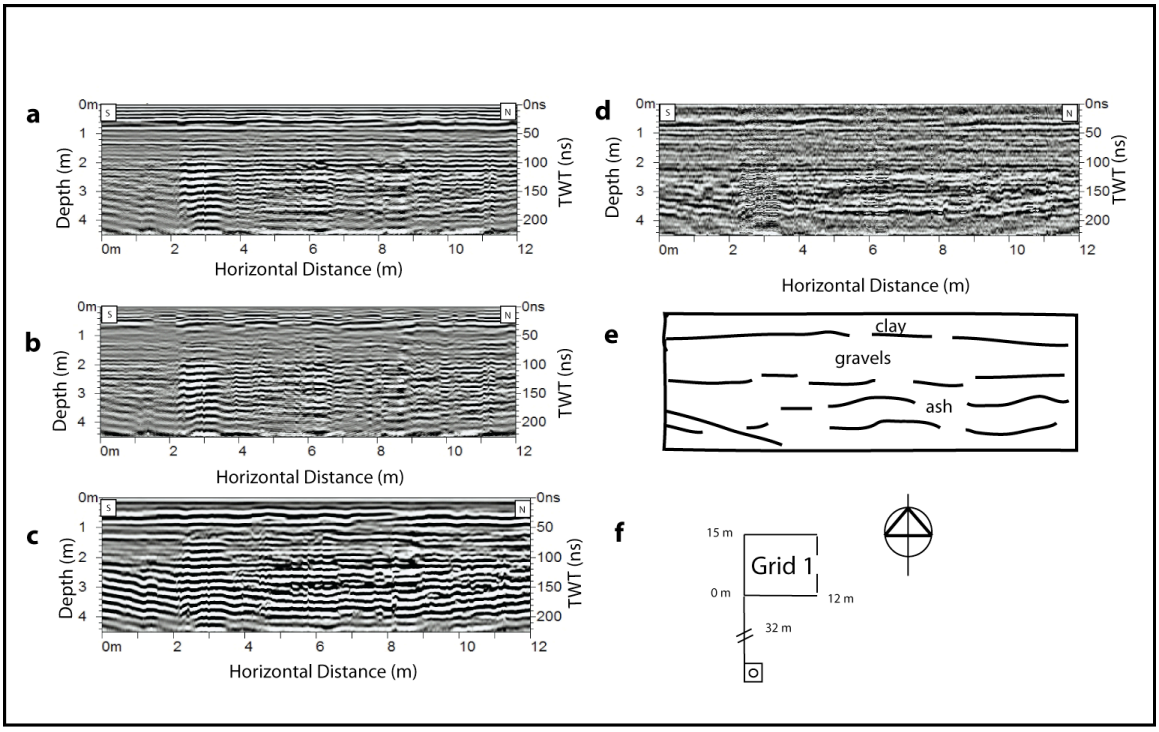

Figure 4.3: Line 12 of Grid 1 radargrams with geologic interpretation. (a) Raw, processed radargram. (b) Background removal filtered data. (c) Background removal and band – pass filter applied. (d) Background removal, band – pass and deconvolution filter applied. (e) Interpretation. (f) Index map of Grid 1 location in survey area. The dashed line indicates the position of the transect relative to the grid.

event. This short (12 m – long) transect provides a first glimpse of the GPR response at the Fanta site, and allows the comparison of other transects collected during the survey.

Grid 2

Grid 2 lies directly to the west of Grid 1 and is an extension of the survey in a much larger grid configuration at 40 × 40 meters. Figure 4.4 shows the radargrams used and an interpretation of the data in Transect 4 of this grid. Figure 4.4a shows the background filter applied to the raw data. Here, generally four units are expressed based on the reflection coherency seen throughout the profile. The relative frequencies and coherency of each reflection pattern provide evidence of differing geological units. Applying the band – pass filter (low – pass: 123 MHz; high – pass: 13 MHz) seen in Figure 4.3b provides additional clarity of the reflection profile. The zone between 50 – 100 ns depth is much more visible and displays greater signal response of the reflectors. In this case, the gravel (fossil – bearing) unit is interpreted as less continuous than the transect shown in Grid 1. A large, dipping reflector is seen between 25 – 15 meters horizontal distance and at 100 ns to the bottom of the profile. This reflection shows the nature of underlying sediments, in this case it most likely relates to the uppermost volcanic tuff unit. Examining this reflector with an applied deconvolution filter, the contrast in the coherency of this unit from underlying units suggest it may be of a different material than the overlying sediments. It is thus interpreted that the tuff unit is undercutting the overlying gravel unit. It is also suspected that the conglomeritic unit extends

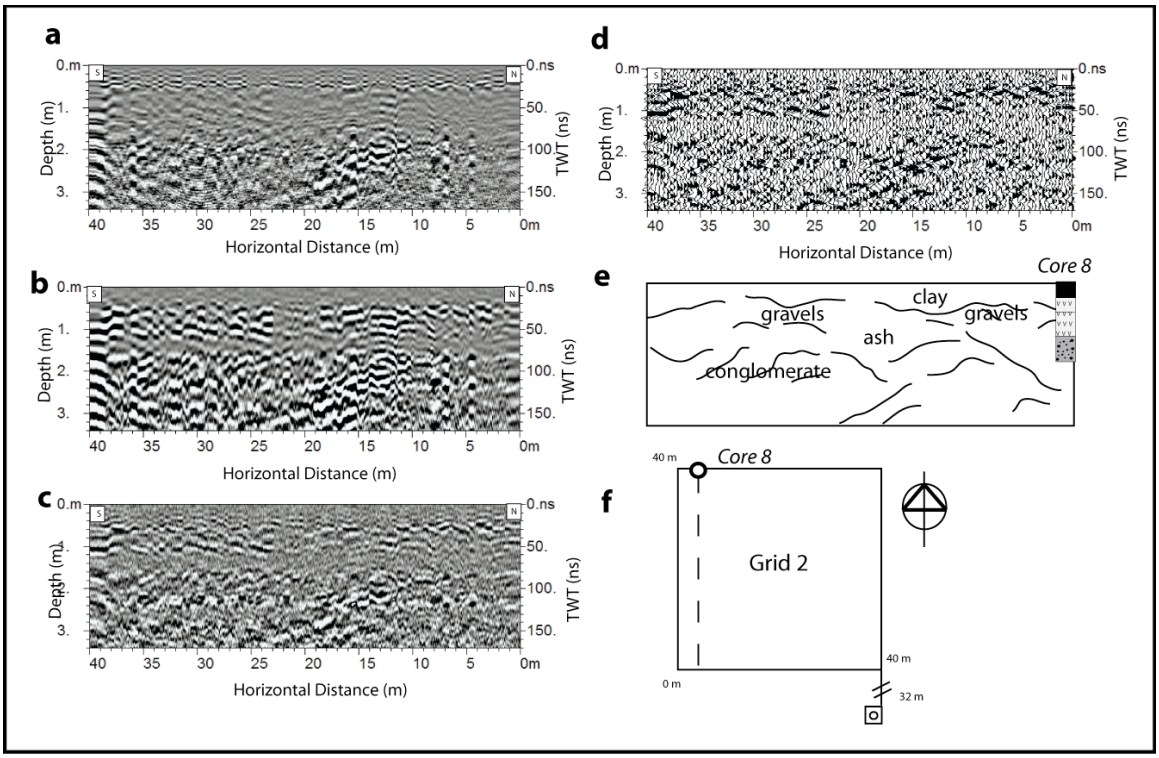

Figure 4.4: Line 4 of Grid 2 radargrams with geologic interpretation. (a) Raw, processed radargram. (b) Background removal and band – pass filter applied. (c) Background removal, band – pass and deconvolution filter applied. (d) Background removal, band – pass and deconvolution filter applied in wiggle display. (e) Interpretation with Core 8 projection. (f) Index map of Grid 2 location in survey area. The dashed line indicates the position of the transect relative to the grid.

from roughly 2.5 meters to the bottom of the profile as the reflectors look weaker and discontinuous at this depth. The same filtering is applied and viewed in the wiggle display (Fig. 4.4d). Visualizing the data in this way provides an interesting contrast from the line – scan or variable density display (see Fig 4.1). This visualization provides a black fill of the positive amplitudes values. Examining across the profile, it may be easier to visualize the location of the reflection surfaces in the wiggle display form. The interpretation (Fig. 4.4e) outlines the major reflections seen throughout the data and provides a four layer model of the subsurface at this location. It is the opinion of the author that the fossil (gravel) unit is present horizontally across the entire profile. The core data can be seen projected in the radargram with interpreted units highlighted (Fig. 4.4d). Here, the radar reflections and interpretations are described with core data from this location for increased confidence in the interpretation. Generally, to the west of the stream cut bank, deposits become thinner compared when compared with Grid 1. These differences in strata show changes in stream sedimentation and may influence the deposition of fossils in this location.

Grid 2: Time Slices

The Grid 2 time slices can be seen in Figure 4.5, where a variety of depths are shown for the shallow subsurface at the site. Time slices were created as described in Chapter III, *GPR Processing*. The generation of time slices allows the location of

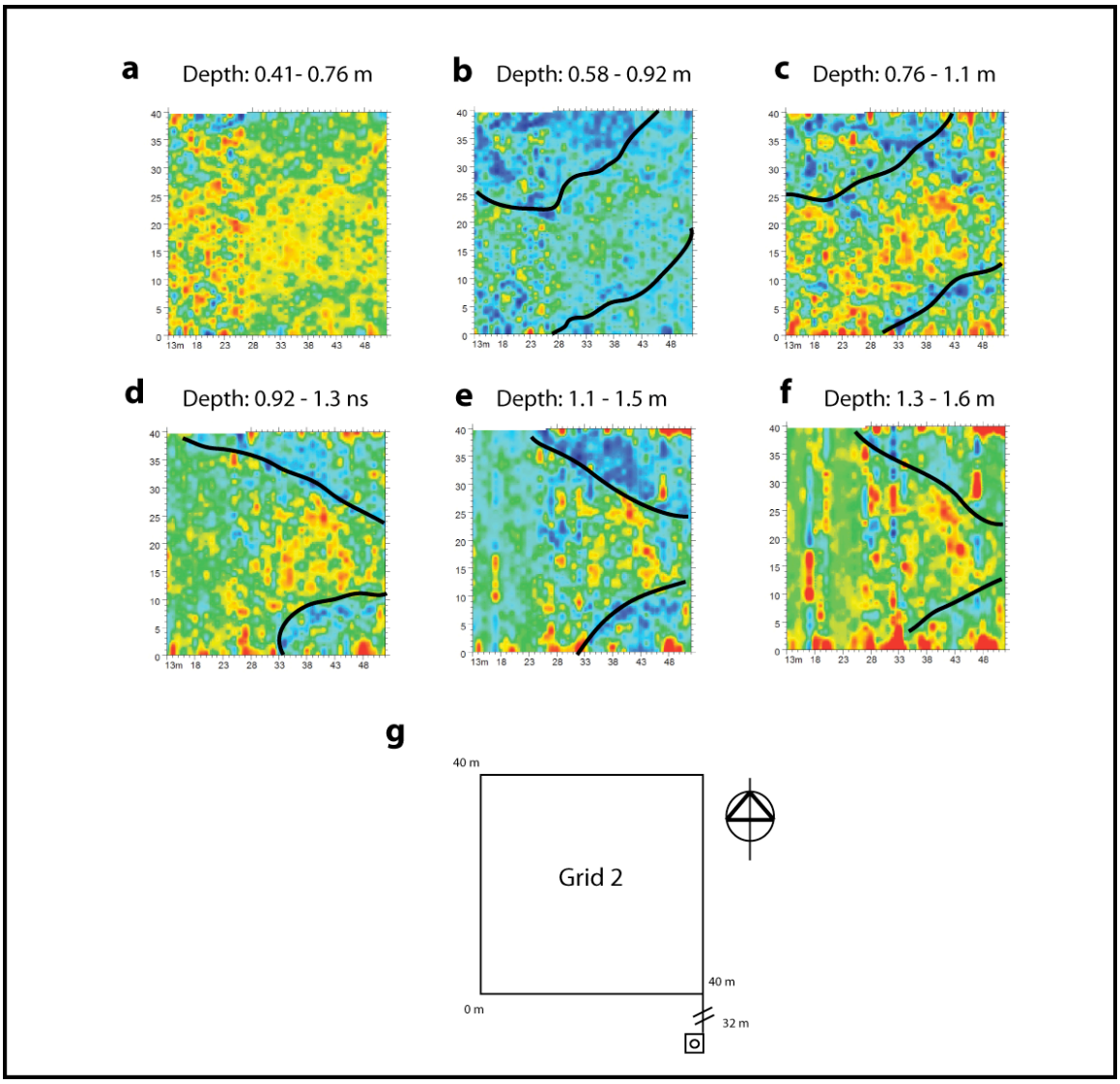

Figure 4.5: Time slice data from Grid 2 of a paleostream channel. Red colors represent high amplitude events and low colors represent low amplitude events. (a) Time slice from depth 0.41 – 0.76 m. (b) Time slice from depth 0.58 – 0.92 m. (c) Time slice from depth 0.76 – 1.1 m. (d) Time slice from depth 0.92 – 1.3 m. (e) Time slice from depth 1.1 – 1.5 m. (f) Time slice from depth 1.3 – 1.6 m. (g) Index map of Grid 2 location in the study area.

stream channel deposits interpreted in the amplitude maps. Figure 4.5a is from 0.41 – 0.76 m depth, the shallowest time slice in this series. Here, a concentration of high – amplitude anomalies can be seen in the western portion of the data. High amplitudes generated at this shallow depth most likely result from clay deposits, as can be seen in the radargrams shown in Figure 4.4.

Visualizing deeper in the section is shown in Figure 4.5b. Here, there is a concentration of high amplitude anomalies seen trending southwest to northeast. This may be related to the beginning of clay infill appearing at the center of the grid. The curvilinear feature seen here is hypothesized to be the remnants of a paleo – stream channel. In Figure 4.5c, this high amplitude pattern has increased in reflection strength, and this most likely represents the channel fill deposit, or center of a paleo – stream channel. Considering the width of this amplitude pattern is consistent with the width of the modern stream channel (between 20 – 25 meters), the interpretation provides a reasonable assumption. Slices seen in Figure 4.5, e and f show a change in the resolution of this feature, and is likely deeper than the subsurface expression of this attribute. In the time slices shown here, it appears as though the high amplitude pattern is becoming narrower in the easterly direction, approaching the distal extent of the channel. This suggests a period of lateral accretion of sediments at this location. The location of fossils within this context is difficult to discern due to the unpredictable nature of fluvial deposition when fossilization occurred. The low amplitude areas surrounding the interpreted stream infill deposits are most likely sediments of lower conductivity, and possibly relate to

gravel or conglomeritic deposits as interpreted in the radargram presented in Figure 4.4e.

Grid 6

Grid 6 was located to the southwest of Grid 1 and to the south of Grid 2, and was in the location near fossil exposures at the site. Seen in Figure 4.6, the transects collected in this grid were oriented from north to south, as were Grid 1 (Fig. 4.3) and Grid 2 (Fig. 4.4). The southern portion of the grid at 0 meters horizontal distance is an area with known fossiliferous deposits. These were visible at the surface and seen from an exposure surface cut by the placement of the water pump (Fig. 3.1). Figure 4.6 shows both raw (Fig. 4.6a) and filtered data. Filters included: background removal filter (Fig. 4.6b), band – pass (low – pass: 114 MHz; high – pass: 20 MHz) and background removal filter (Fig. 4.6c), and a combination of deconvolution and band – pass filters (Fig. 4.5d). Additionally, interpretations of the radargrams (Fig. 4.6e) and index map (Fig. 4.6f) are also presented. Data generally follows a three-layer model of clay, ash and conglomeratic units, as seen most clearly in the deconvolution filtered image (Fig. 4.6d).

The first file presented shows the raw data. This profile has gone through the same processing workflow as other files, but without filtering applied. As seen in Figure 4.6a, the profile appears noisy and does not show any clear reflection patterns. Strong horizontal banding noise is generally in two locations: between 0 and 25 ns and between 25 and 140 ns depth. This ringing can be a result of many types of interference and is also known as the occurrence of multiples (more detail

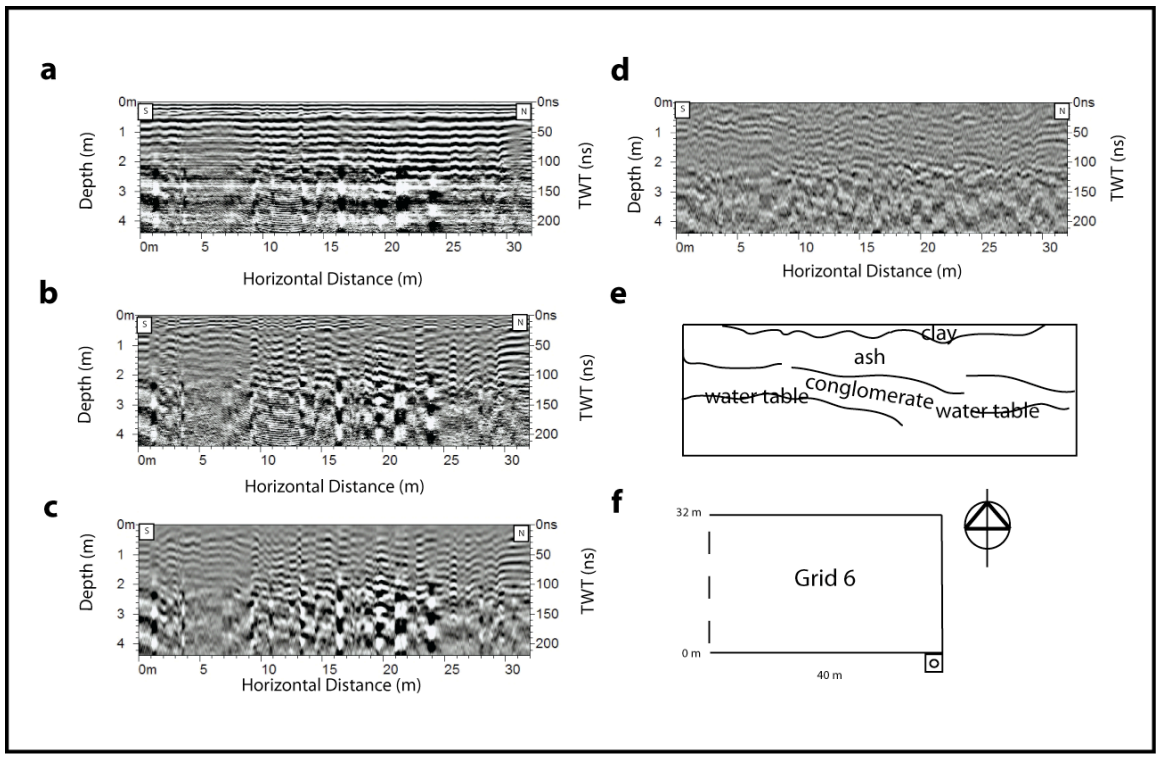

Figure 4.6: Line 1 of Grid 6 radargrams with geologic interpretation. (a) Raw, processed radargram. (b) Background removal filtered data. (c) Background removal and band – pass filter applied. (d) Background removal, band – pass and deconvolution filter applied. (e) Interpretation. (f) Index map of Grid 6 location in survey area. The dashed line indicates the position of the transect relative to the grid.

on this was presented in Chapter III). The application of background filtering can be seen in Figure 4.6b. Here, the ringing in the top of the section has been removed and in the lower portion of the radargram the banding still remains, but with noise removed so that it does not stretch across the entirety of the profile.

The resulting data does not display a low amplitude, low coherency pattern characteristic of the gravel unit as seen in the previous profile, and it is interpreted that the bone unit may not extend into this direction. Data interpretations for this radargram also include a thick (over 1 m) subsurface reflection that is attributed to the water table. Considering the low frequency reflections of different character than preceding profiles, as well as the depth to this feature, this is the most likely scenario. This feature was also present in the previous radargram (Fig. 4.4) but was removed to highlight only the uppermost reflections.

Grid 6: Time Slices

The time slices generated for Grid 6 show a broad, high – amplitude anomaly dominantly in the center of the grid. Figure 4.7 shows the time slices from 0 – 1.1 m depth. The first image (Fig. 4.7a) shows a preferential high amplitude area in the center of the grid, at roughly 15 m in width. As discussed previously, this is the approximate size of what is interpreted as a paleo – stream channel. The anomaly generally runs from east to west across the grid (Figs. 4.7a and b). In Figure 4.7b, however, there seems to be a bend in the direction of this high – amplitude area, appearing between 10 – 25 meters across the horizontal axis. These types of fluctuations in the amplitude values that conform to this shape may relate to stream

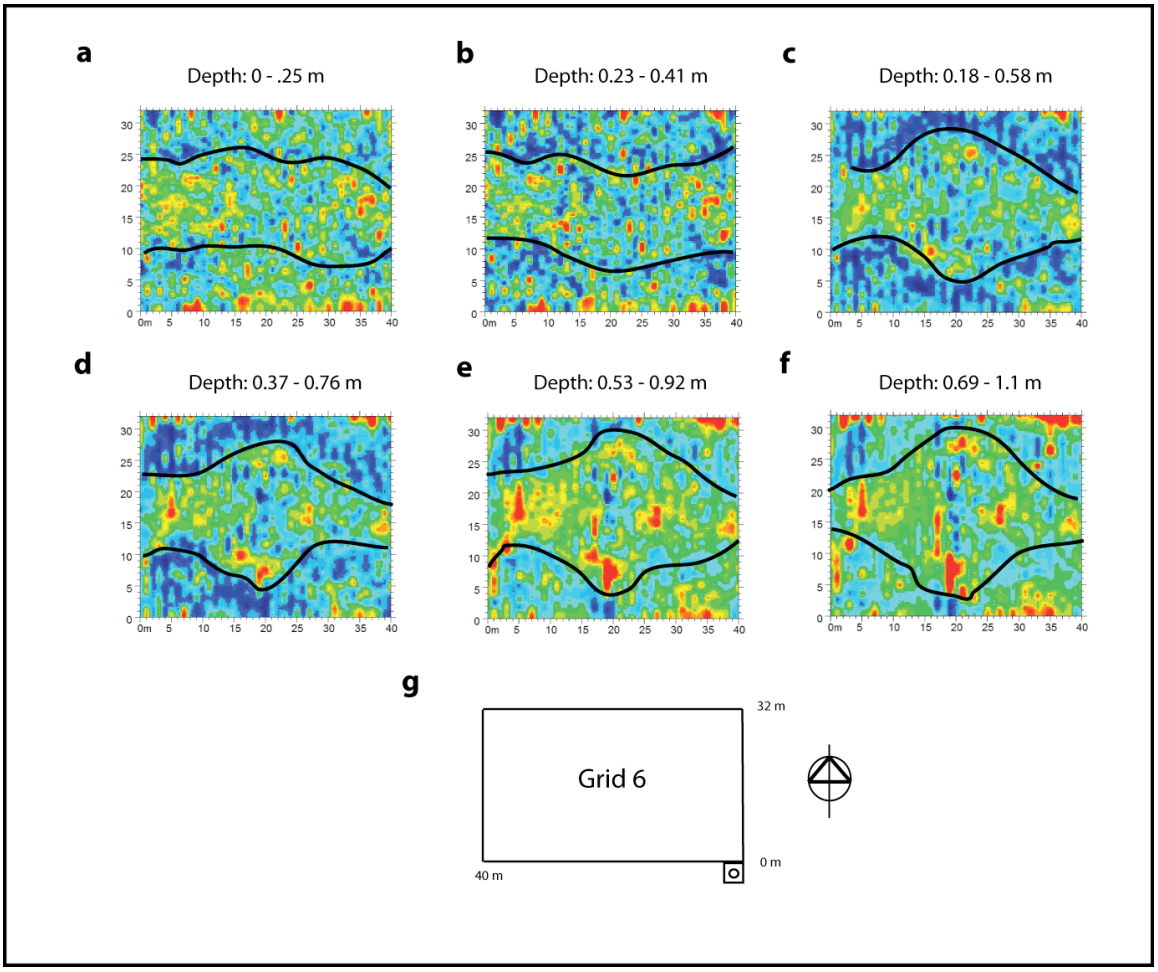

Figure 4.7: Time slice data from Grid 6 of a paleostream channel. Red colors represent high amplitude events and low colors represent low amplitude events. (a) Time slice from depth 0 – 0.25 m. (b) Time slice from depth 0.23 – 0.41 m. (c) Time slice from depth 0.18 – 0.58 m. (d) Time slice from depth 0.37 – 0.76 m. (e) Time slice from depth 0.53 – 0.92 m. (f) Time slice from depth 0.69 – 1.1 m. (g) Index map of Grid 6 location in the study area.

networks as interpreted in the previous time slices for Grid 2 (Fig. 4.5). Figure 4.7c shows a different pattern, however, and a high amplitude bulge appears in the center of the time slice. Here, a central curvilinear feature is surrounded by low amplitude values on either side of this anomaly. This is interpreted as a thickening of clay infill or ash deposits, representing the lateral accretion surface of the stream in the north to south direction. This feature occurs at a relatively shallow depth and can be seen in Figures 4.7c, d, e, and f, where the general shape of this anomaly is preserved from 0.18 – 1.1 m depth. Again, high amplitude values seen on the edges of the time slices in Figures 4.7e and f are most likely related to edge effects and are not interpreted here.

Grid 16

Grid 16 provides data in the western portion of the survey. It was previously thought that this area was not considered as a suspect fossil location based on the surface survey conducted by Bobe and Assefa in 2008 (see Fig. 3.3). GPR data shown in Figure 4.8 documents the presence of a low amplitude reflection zone interpreted as the top of the gravel fossil – containing unit. Transect 1 is at the most western section of Grid 16, and is located at 140 m due west of the control well (Fig. 4.8f). This grid provides a wide aerial extent of the survey, and links grids collected in other fossil – bearing areas known from cut bank exposures.

Data in this grid provides strong reflections at various depths across the profile. Raw data is subjected to airwave interference at the top of the profile (Fig. 4.8a between 0 – 60 ns depth). Here, horizontal banding is possibly generating due

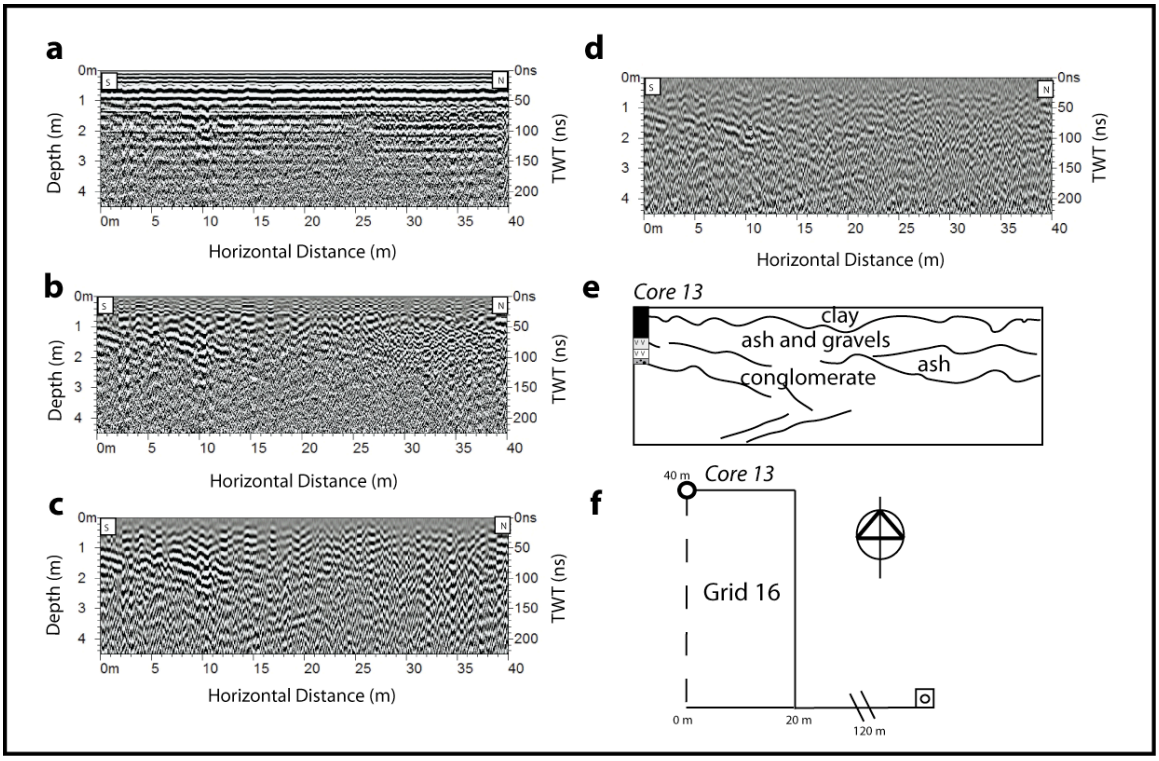

Figure 4.8: Line 1 of Grid 16 radargrams with geologic interpretation. (a) Raw, processed radargram. (b) Background removal filtered data. (c) Background removal and band – pass filter applied. (d) Background removal, band – pass and deconvolution filter applied. (e) Interpretation with Core 13 projection. (f) Index map of Grid 16 location in survey area. The dashed line indicates the position of the transect relative to the grid.

to interference from unstable surface topography. In Figure 4.8b, after background removal filtering the section appears to show enhanced clarity, especially in the near – field zone (between 0 – 50 ns depth) previously masked by airwave interference. This has revealed an undulatory abrupt contact between the black cotton soil and underlying gravel unit. Dipping reflectors can be seen generally from 50 – 100 ns depth. Figure 4.8c provides a clearer, more enhanced data display with the use of band – pass filtering (low – pass: 90 MHz; high – pass: 13 MHz). This is especially true in the lower portion of the section between 100 ns to the bottom of the profile.

The interpreted section (Fig. 4.8e) describes the various strata as a four-layer model. A low – angle, dipping reflector was interpreted between approximately 10 and 20 meters on the horizontal axis and most likely is related to tuff deposits due to its strong coherency, depth and large amplitude value. This area documents the presence of the fossil unit and is confirmed by Core 13 as existing in a location containing the conglomeritic unit. Deconvolution, background and band – pass filtered data (Fig. 4.8d) provides the highest resolution image of the subsurface. Here, the nature of deposits can be seen and is interpreted in Figure 4.8e. The inclusion of core data with the interpretation highlights the continuity of reflections with the core information. Here, clay appears in the upper portion of the profile, as seen in the radargram in Figure 4.8d. This is then followed by a mix of tuff and gravels, being a possible location for fossil deposits. Below this, several dipping beds can be seen here and are interpreted as tuffaceous in nature.

Grid 4

Grid 4 is located near another fossil rich zone and was 40 × 40 meters in area, a large grid compared with other surveyed areas shown thus far. Grid 4 is adjacent to Grid 3, the area used in depth calibration procedures as outlined in Chapter III. Grid 4 outlines a western portion of the survey area and attempts to constrain the most southwestern lateral extent of the exposed fossil unit in the southerly direction. Figure 4.9 shows the location of this grid and radargrams used in stratigraphic analysis. Raw data in Figure 4.9a does not provide much diagnostic information regarding the stratigraphy at the site because of the horizontal banding noise seen throughout much of the profile. At greater depths, reflection interpretation becomes difficult due to multiples appearing in the data and a loss of reflection continuity, most likely due to the water table. The next radargram (Fig. 4.9b) shows the background removal and band – pass filter (low – pass: 138 MHz; high – pass: 45 MHz) applied to the raw data. There is much greater clarity in the upper portion of the profile from 0 to 60 ns depth, but multiple reflections still exist for almost the entirety of the radargram. Figure 4.9c shows the deconvolution filter applied to the background and band – pass filtered data. Here, the multiples seen throughout the other profiles were eliminated to display a composite image of the multiple applied filters. The wiggle display in Figure 4.9d is a result of the deconvolution applied filtering plotted with a shallower depth range to highlight specific near – surface reflections that exists within the data. The interpretation (presented in Fig. 4.9e) documents a three – layer model of the subsurface in this location. Based on the area of lower coherency between 0.80 – 1.50 meters, it is

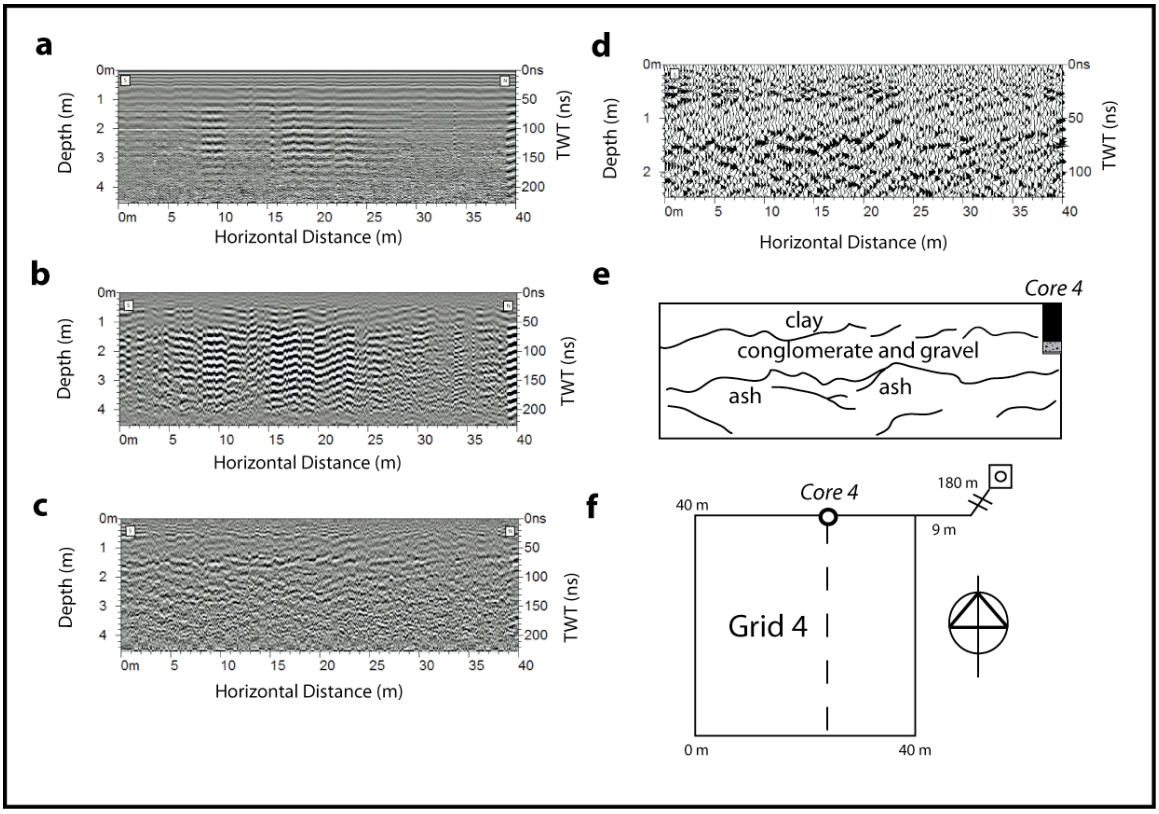

Figure 4.9: Line 25 of Grid 4 radargrams with geologic interpretation. (a) Raw, processed radargram. (b) Background removal and band – pass filter applied. (c) Background removal, band – pass and deconvolution filter applied. (d) Background removal, band – pass and deconvolution filter applied in wiggle display. (e) Interpretation with Core 4 projection. (f) Index map of Grid 4 location in survey area. The dashed line indicates the position of the transect relative to the grid.

expected that the fossil unit still exists throughout the entire gridded area here. Additionally, the core data from this survey is displayed with the reflection interpretation for clarity.

Grid 4: Time Slices

The generation of time slices in Grid 4 provided some interesting results related to amplitude values generated from the combination of profiles surveyed. Figure 4.10 shows three time slices that were generated between 0.25 – 1.13 m depth. In the first image (Fig. 4.10a) there appears to be a selection of high amplitude anomalies appearing in the center of the grid, spanning from northeast to southwest in direction. Despite the high amplitude values appearing to the extreme left of the grid, a curvilinear anomalous shape appears to resemble that of the paleo – stream channel. This orientation is opposite of that seen in Figure 4.5 where a northeast – southwesterly orientation can be seen. It is expected that there would be a differing pattern associated with these two areas, as they are spatially distant from each other. Figure 4.10b shows varying distribution of high amplitude events. This occurs between 0 – 10 meters horizontal distance along the x – axis and trends in the northwest direction. Another high amplitude area is seen to the east of this feature, and is separated by a low amplitude area. In the next figure (Fig.4.10c), the pattern appears to be complicated by varying high amplitude features in what appears to be in various clustered locations across the grid. The separation of the northern verses southern amplitude variations can be seen in the interpretation and is likely a result of stream incision, here at a depth of 0.78 – 1.13 m. The high

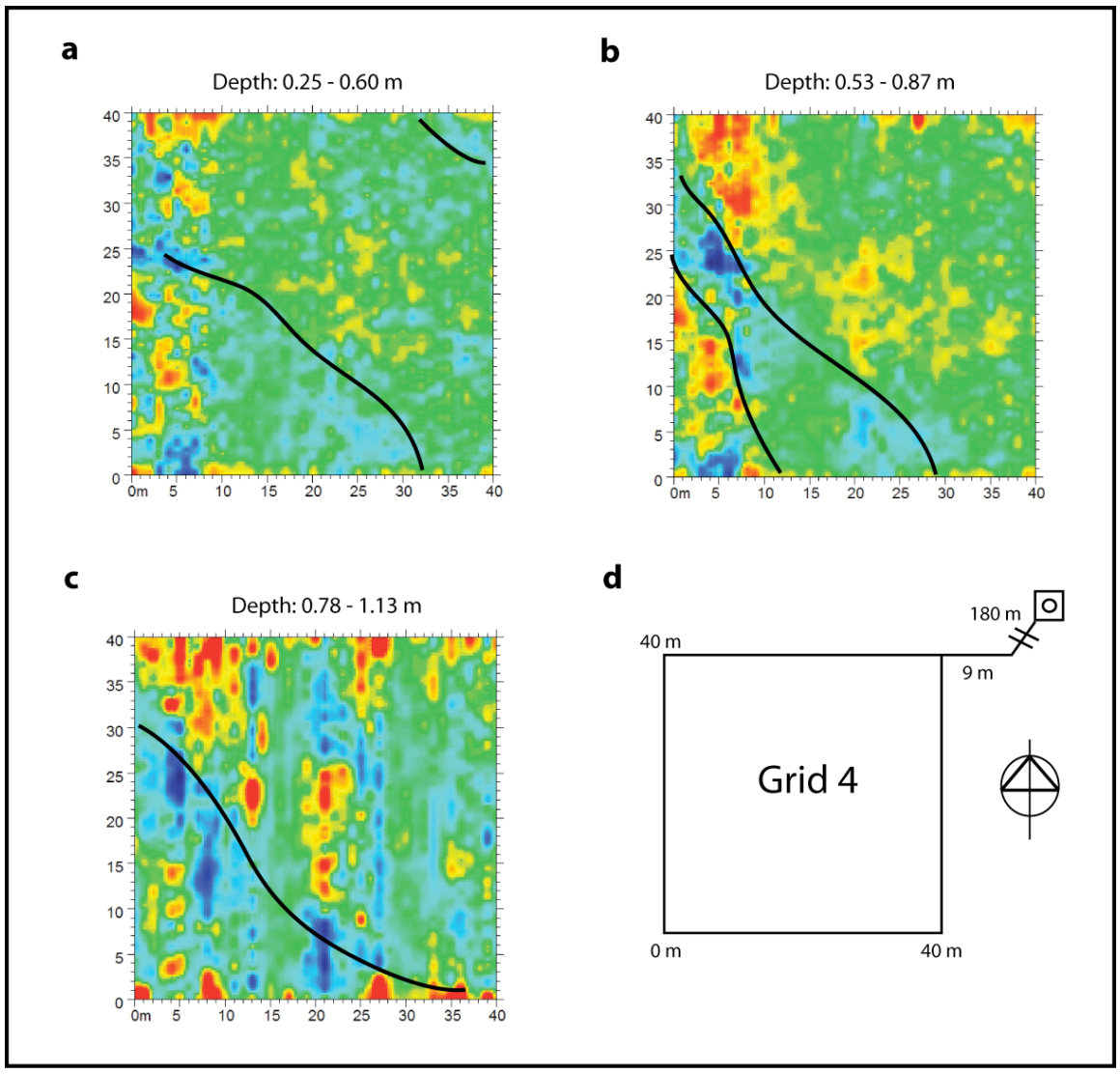

Figure 4.10: Time slice data from Grid 4 of a paleostream channel. Red colors represent high amplitude events and low colors represent low amplitude events. (a) Time slice from depth 0.25 – 0.60 m. (b) Time slice from depth 0.53 – 0.87 m. (c) Time slice from depth 0.78 – 1.13 m. (d) Index map of Grid 4 location in the study area.

amplitude anomalies seen in the extreme southern part of this time slice may be related to edge effects and are not considered in the interpretation of these data.

Grid 19

Grid 19 is located to the northeast of the control well, to the west of Grid 2. This grid is 40 × 20 meter in area, as the 40 × 40 meter grids proved to be a problematic configuration during data collection. This is because of the movement of the radar antenna and control unit across the large area was taxing on the individuals pulling the antenna. A 20 × 40 meter area was an optimal size that allowed for additional set – up adjustments before data collection began. This is especially true with regard gain control. The gain setting was the most problematic parameter to control during data collection since amplitude values changed drastically across the site. Adjusting to smaller grid sizes thus allowed for easier control over the gain function throughout the survey.

Figure 4.11a shows the raw radar profile. Banding noise is present across almost the entire radargram throughout the raw data. These ringing effects were seen in a variety of the raw data files (i.e. Figs. 4.3a, 4.4a, etc.) and were successfully removed using background and band – pass filtering as seen in Figure 4.11b (low – pass: 174 MHz; high – pass: 12 MHz). Throughout this radargram, reflections as a variety of depths can be seen and were selectively interpreted. This is seen particularly at the contact of clay and gravel, at roughly 0.5 meters depth. A series of reflections appear to be dipping at roughly 0 to 5 meters on the horizontal axis just

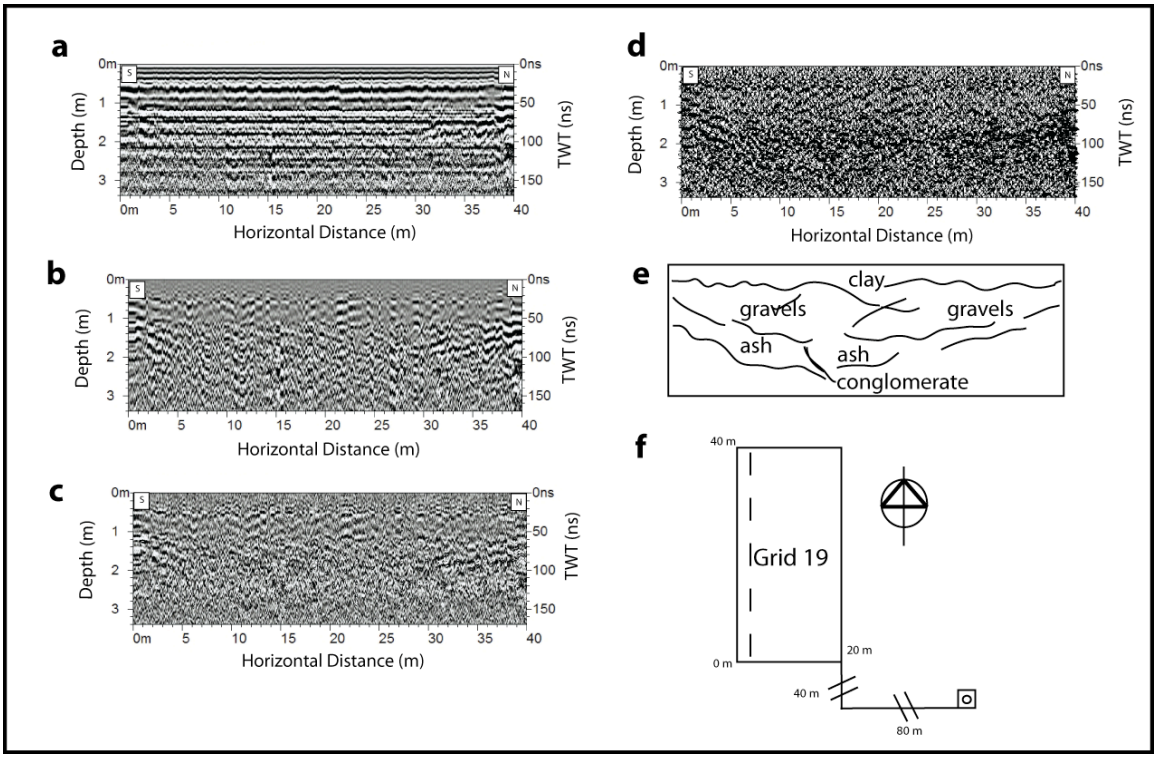

Figure 4.11: Line 4 of Grid 19 radargrams with geologic interpretation. (a) Raw, processed radargram. (b) Background removal and band – pass filter applied. (c) Background removal, band – pass and deconvolution filter applied. (d) Background removal, band – pass and deconvolution filter applied in wiggle display. (e) Interpretation. (f) Index map of Grid 19 location in survey area. The dashed line indicates the position of the transect relative to the grid.

below this depth, and it appears that the overlying sediment, the conglomeritic unit, is onlapping against a highly reflective unit, interpreted as volcanic tuff. Depths below this are thought to be conglomeritic due to the strong amplitudes related to a generally low coherency reflection pattern. The deconvolution filter applied to the data as seen in Figure 4.11c exemplifies the reflections between 30 – 100 ns. This is interpreted as gravel deposits due to its characteristic low coherency.

Another feature is what appears to be related to the other interpreted dipping unit between 30 to 40 meters on the horizontal distance axis. This may be a concave feature related to paleo – fluvial channelization. The time slice data however does not provide additional evidence to support this interpretation. These data may suffer from edge effects related to starting and ending line gain transitions as seen in other time slices. The wiggle display (Fig. 4.11d) shows additional detail to aid in interpretation. Here, a four-layer model of sediments occurs in this transect and is interpreted in Figure 4.11e. It is expected that the fossil layer exists past this extent of the grid, enlarging the previous boundaries of the site from the surface survey by Bobe and Assefa conducted in 2008.

Grid 8

Grid 8 is located on the opposite side of the stream channel as all of the other grids described so far. This is to the east of the control well, where fossils are exposed at the surface. This area is known to contain similar fossils to the other side of the channel, however it is also unknown how far these deposits stretch laterally across the site. Figure 4.12 shows a profile collected at transect 14, almost halfway

through the gridded area. Figure 4.12a shows the raw, processed data. As with most other raw profiles, horizontal banding noise effects mask the section, and not much data is visible at the top of the profile. Between 0 to 70 ns depth the radargram is largely composed of banding noise. Some diffraction hyperbola can also be seen at various depths. In Figure 4.12b, the background removal filter has been applied. In this radargram, much higher resolution and clarity of reflections are present compared to the raw data. The uppermost 0 – 30 ns contains high frequency reflections related to the clay capstone unit. Blow this, between 30 to roughly 70 ns depth, there appears to be a unit with less defined coherency. This is most likely related to the graveliferous unit due to its lack of coherency compared with over and underlying lithological units that display continuous high amplitude reflection patterns. In the northern portion of the radargram at this depth there also appears to be a dipping reflector from 0 – 10 meters horizontal distance. On the next profile (Fig. 4.12c), the application of an applied band – pass (low – pass: 182 MHz; high – pass: 51 MHz) and deconvolution filter shows the vertical extent of a dipping reflector, which stretches from 0 to 17 meters horizontally. This significant feature may be related to stream morphology and incision, although this interpretation not evident in the time slice data. Various cross – bedded reflections appear to the left of this feature, their geometry discordant and complex and is generally of low coherency. This may be related to the conglomeritic – volcanic tuff interface, where the interplay of the sedimentary and fluvial systems have caused this complex geophysical signature. The wiggle display (Fig. 4.12d) highlights data with positive fill and provides a different visualization from the line – scan display mode. Here,

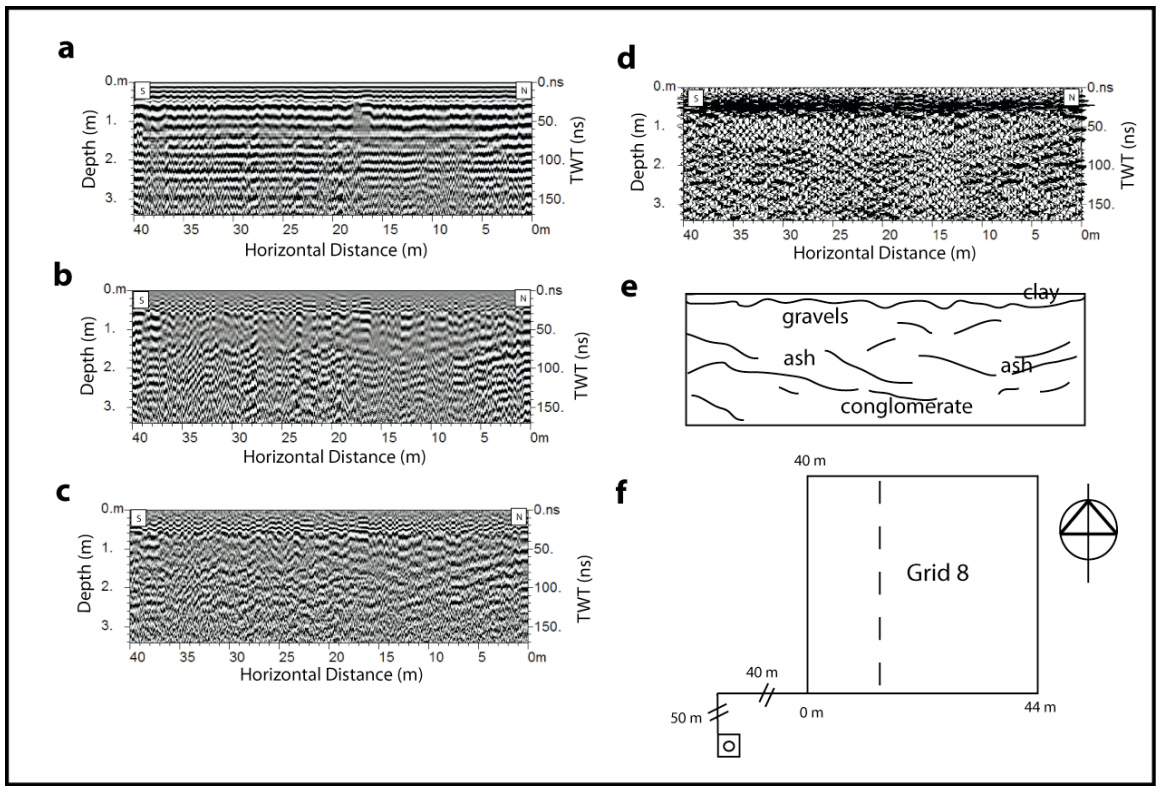

Figure 4.12: Line 14, of Grid 8 radargrams with geologic interpretation. (a) Raw, processed radargram. (b) Background removal and band – pass filter applied. (c) Background removal, band – pass and deconvolution filter applied. (d) Background removal, band – pass and deconvolution filter applied in wiggle display. (e) Interpretation. (f) Index map of Grid 8 location in survey area. The dashed line indicates the position of the transect relative to the grid.

the cross-bedded features located throughout the profile from approximately 2 m to the bottom of the section can be seen more clearly. The interpretation (Fig. 4.12e) highlights a four layer model of clay, gravels, tuff and conglomeritic units. The continuity of the reflection patterns seen here relate to the same geological interpretations as in the other grids, and provides some corroborative data control with which to compare results.

Grid 20

Grid 20 represents a grid in the northern portion of the survey. It is located in a different fossil area than grids presented thus far. The extent of the fossil bed is unknown in this location, and only minimal exposure in the stream sediments and on the surface allows any indication of fossils. This area is in the northern extent of the initial delineation of the site completed in 2008 by Assefa and Bobe. Interestingly, GPR data and sediment coring has demonstrated the potential presence of the gravel unit in this area. In Figure 4.13a, the raw radargram is shown. In this image, there appears to be horizontal banding noise present from 0 to 70 ns depth. This is the same banding noise that appears in much of the raw data presented thus far. Reflections are present below this depth, and they appear to be more visible in this image than in other raw images. The clarity of the lower portion of the profile may be related to low water content or changing lithology and significant contrasts in RDP across the site. This image, however, does not allow the readily definable units known in this location to be accurately interpreted. Figure 4.13b shows the same transect with the applied background

removal filter. In this image, it appears as though the horizontal banding noise has been removed, allowing for a more interpretable section of the subsurface to be displayed. Between 0 – 0.6 m there appears to be very high – frequency undulatory reflection pattern that most likely represents the clay capstone unit. Directly below this at 0.7 – 1.5 m depth, there is a relatively low frequency unit with low coherency. This is assumed to be the graveliferous unit, as core data has confirmed this depth and it is seen throughout the interpreted section (Fig. 4.13e). Below this depth, at 1.5 m to the bottom of the profile, various cross – bedded and slightly dipping reflections are present. This represents the ash and conglomeritic unit, and potentially a mix of the two. The next image (Fig. 4.13c) shows the band – pass filter applied to the background filtered data (low – pass: 144 MHz; high – pass: 37 MHz). This data appears to show the same reflections as the previous image but is more 'smoothed' and appears to be a higher – resolution image compared with Figure 4.13b. The next image (Fig. 4.13d) shows the same applied filters as the previous profile but in wiggle display format. In this view, the reflections can be visualized more easily for interpretation. Displaying core data alongside the profile allows the interpretation of this data with that of the collected core, in this case, Core 10 was used as it approximates the nearest sampled location to the transect. Here, the interpretation reflects both core data and radar reflections. In all, this area is suspected to contain fossiliferous deposits throughout.

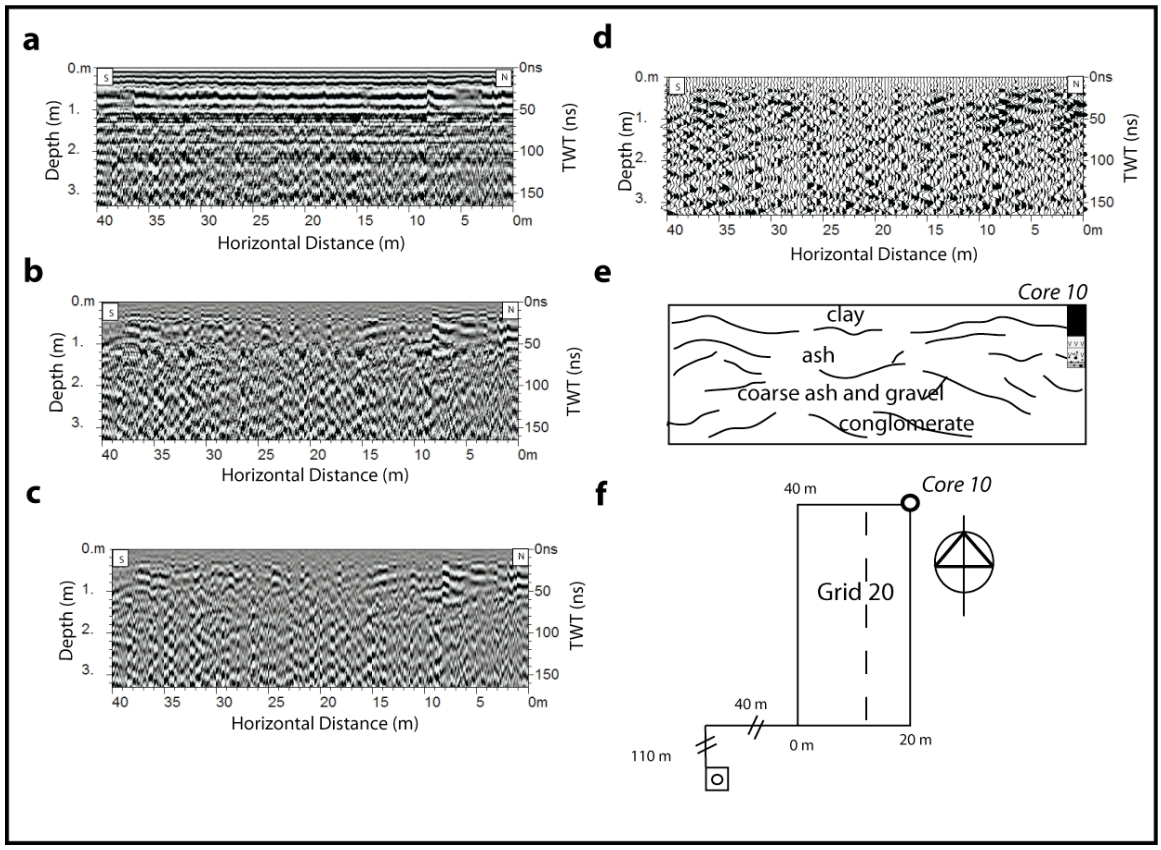

Figure 4.13: Line 12 of Grid 20 radargrams with geologic interpretation. (a) Raw, processed radargram. (b) Background removal filter applied. (c) Background removal and band – pass filter applied. (d) Background removal and band – pass and filter applied in wiggle display. (e) Interpretation with Core 10 projection. (f) Index map of Grid 20 location in survey area. The dashed line indicates the position of the transect relative to the grid.

Grid 20: Time slices

Time slice data recorded from this grid shows some interesting features that may be related to the Fanta stream's ancient morphology. Figure 4.14 shows a series of time slices over varying depths from 0 to 2.14 meters total. These data do not have any applied filtering and are raw time slice images. Throughout the succession of time slices, it appears as though high – amplitude anomalies (in red) appear to stretch across much of the center of the time slice. Based on the curvilinear geometry of this high – amplitude feature, a possible paleomeander bend, it is hypothesized that this may be related to a paleo – fluvial channel of the stream itself. Considering the low amplitude features (blue) in relation to the high – amplitude anomaly, there is a significant change in properties of these materials. A high – amplitude response may be related to potential clay infill within these areas. This may describe the orientation of fossils if they are related to lag deposits within the paleo – channel, interpreted as the blue area.

With increased depth, it appears as though the interpreted meander bend pattern changes. This reflects transformations over time, and it appears to be shrinking in size or changing laterally with increased depth. The last time slice (Fig. 4.14e) shows this feature pinching out to other high – amplitude linear reflections. These are most likely related to striping or edge effects during data collection and not an interpretable subsurface feature. It is additionally hypothesized that the low – amplitude areas should be examined during future periods of the site's ultimate excavation.

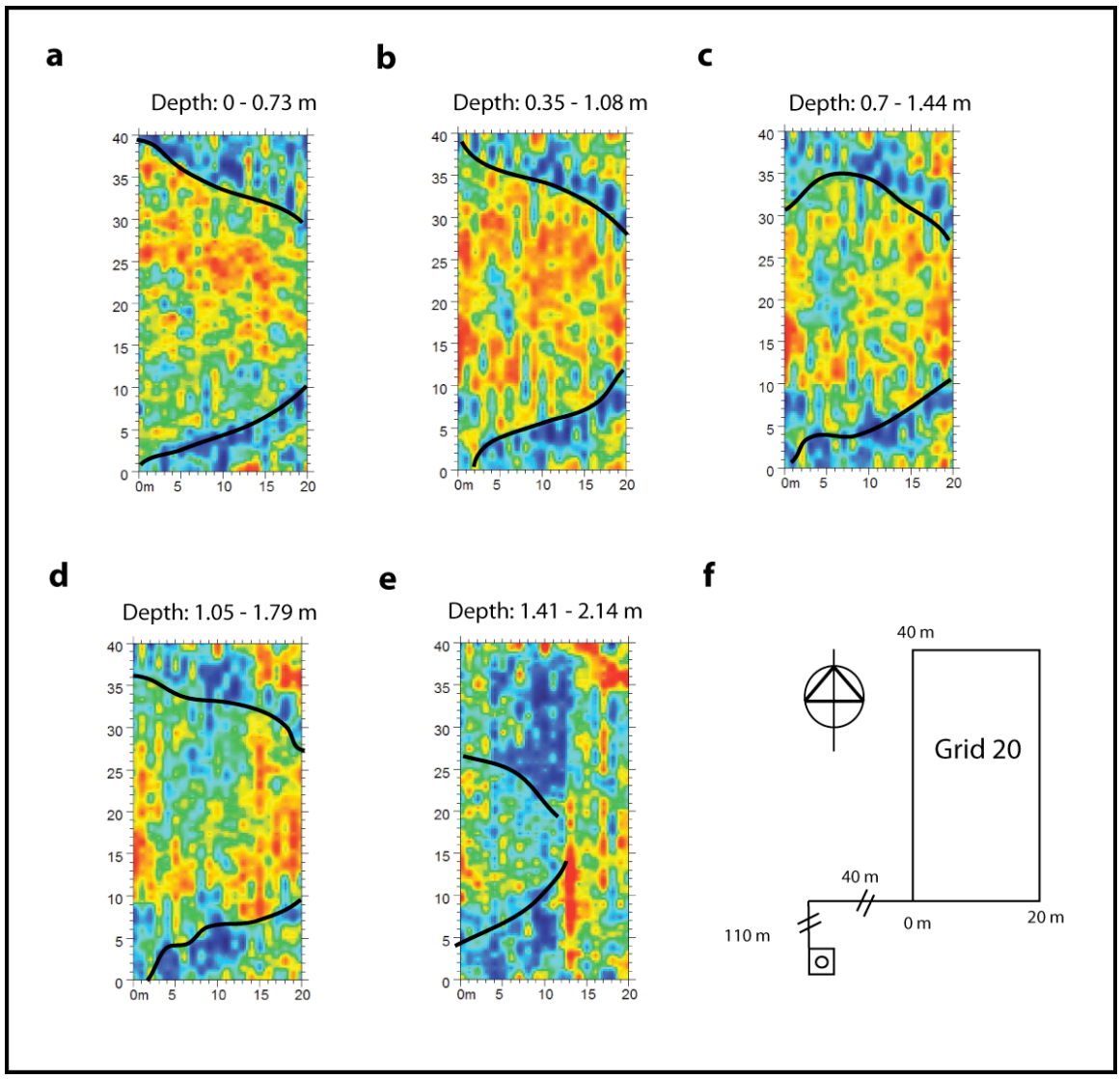

Figure 4.14: Time slice data from Grid 20 of a meander bend in the paleostream channel. (a) Time slice from depth 0 – 0.73 m. (b) Time slice from depth 0.35 – 1.08 m. (c) Time slice from depth 0.70 – 1.44 m. (d) Time slice from depth 1.05 – 1.79 m. (e) Time slice from depth 1.41 – 2.14 m. (i) Index map of Grid 20 location in the study area.

Figure 4.15 shows an intersection of a time slice with the profile data. This provides an excellent visualization of the two data types. The radargram has been colored to highlight the high – amplitude areas and to match the time slice color scheme. The high amplitude anomaly in the time slice (taken from 0.35 – 1.08 meters depth, Fig. 4.15b) appears to fall in the same location as the high amplitude reflections in the profile data. This highlights the relationship of the time slice data in conjunction with profiles. The high – amplitude reflections to the left side of the radargram is most likely related to noise due to edge effects, and questions the validity of the high – amplitude anomalies on the sides of the time slices. Figure 4.15b highlights the areas that are interpreted as a result of paleo – fluvial action. The geometry of the high amplitude reflections on the profile data appears to be a result of fluvial incision. This is more clearly seen in the interpretation. Figure 4.15c shows an index map of the grid location in reference to the projected images. The time slices seen in Figure 4.15 is a result of composite profiles over the entire gridded area shown in this illustration.

2010 Results

2010 data was collected in various locations with respect to the grids in 2009 (Fig. 3.2) during a different seasonal period at Fanta. Data was collected on March 13 – 15, 2010. This is generally a drier period of the year than in the summer months when the 2009 survey took place. Results may be greatly affected by this change in hydrological conditions. During this survey, intersecting transects in fence diagram configurations were selected over the grid geometry. This was due to the

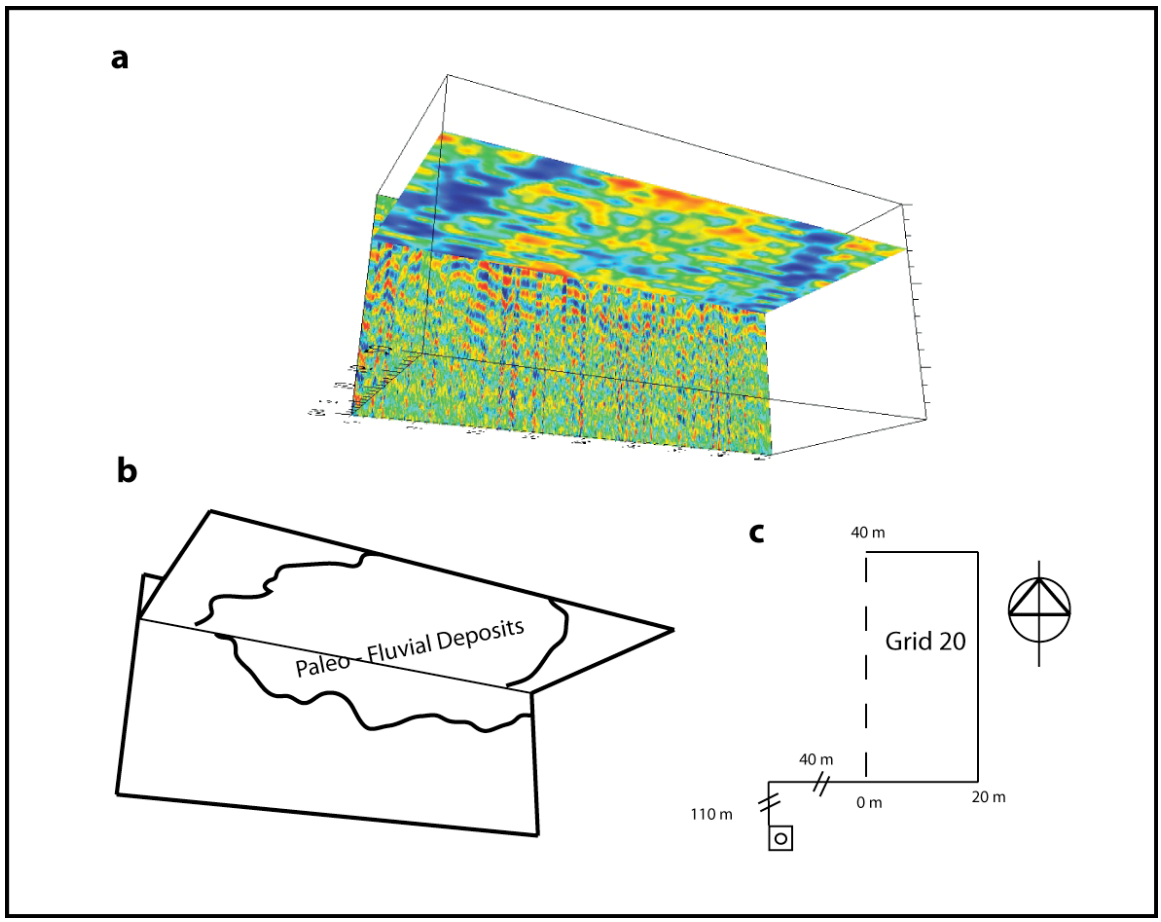

Figure 4.15: Grid 20 time slice intersection with Line 1 radargram showing the meander bend and fluvial accretionary deposits of the paleostream channel. (a) Background and band – pass filtered radargram with time slice from depth 0.35 – 1.08 m. (b) Interpretation. (c) Index map of Grid 20 location in the study area. The dashed line indicates the position of the transect relative to the grid.

time constraint placed on the author during this time, which only allowed for a few days of additional data collection. The 2010 survey was only a short field season with Assiged Getahun of the Ethiopian Geological Survey and Addis Ababa University. This took place while the author was participating in another archaeological research project, SWEAP, the Southwest Ethiopia Archaeological Project, led by Steven Brandt of the University of Florida. The GPR system and survey equipment was the same as the survey completed in 2009. Only the site's environmental conditions were different. A photograph of the site taken in 2010 (seen in Fig. 4.16) shows the difference in surface conditions compared with the 2009 survey (Fig. 4.1). During this survey, the surface was unplowed and was laterally uniform. This may have additionally affected the resolution of the dataset.

Transects 1 – 7

The first surveyed area from 2010 is located near the visible fossil exposures at 20 – 40 meters north of the control well. The alignment of transects created a long series of profiles; where 2 transects totaling 80 meters long were collected perpendicular to the stream, in the opposite direction as the 2009 survey grids comprising this area. This was done in order to examine the changes in strata in the perpendicular direction, which may yield additional information about the extent of fossil beds.

Transects 1 – 7 overlay Grids 1, 2, 6, 18, 19, and 22 (Figure 4.17), encompassing a large area. Transects were aligned using a box geometry with a total of 7 transects. Each of these transects were re – collected in the reverse direction at

Figure 4.16: Photograph documenting the surface conditions at Fanta during the 2010 survey.

a shorter time window (150 ns instead of 250 ns). These data did not provide any laudable advantage to the 250 ns data, and are not displayed throughout this Thesis. However, several images are displayed at a lower sample range to cut off low frequency noise that is present in the 2010 data, and appear to be at 150 ns depth or deeper. The choice to employ a shorter sample window was evaluated for each file, and only the clearest, processed data was selected.

In Figure 4.17a, raw data from Transect 4 can be seen. Horizontal banding noise is apparent in the uppermost portion of the profile, from 0 to 1 m depth. This banding noise is punctuated by several diffraction hyperbolas, specifically at 8, 10, 26 and 31 meters horizontal distance at roughly 1 m depth. Additional striping in the data appears below 1 m to the bottom of the profile. This is more subtle than the high amplitude striping at the top of the section, and does not appear visible after background removal and band – pass filtering (low – pass: 123 MHz; high – pass: 28 MHz) seen in Figure 4.17b. Figure 4.17c shows the same profile with deconvolution applied to the same filtering techniques previously mentioned. Here, the high – frequency near field zone between 0 – 0.5 m is more apparent throughout. Below this depth, various horizontal reflectors can be visualized. The wiggle display shows reflection surfaces more apparently in Figure 4.17d. The interpretation is presented in the next image (Fig. 4.17e) and outlines a three – layer model of the subsurface based on coherent positive amplitude reflections. Generally, low coherence amplitudes from 1 – 1.3 m depth is hypothesized to be composed of gravel deposits. Directly below this unit, a more coherent reflection pattern appears horizontally

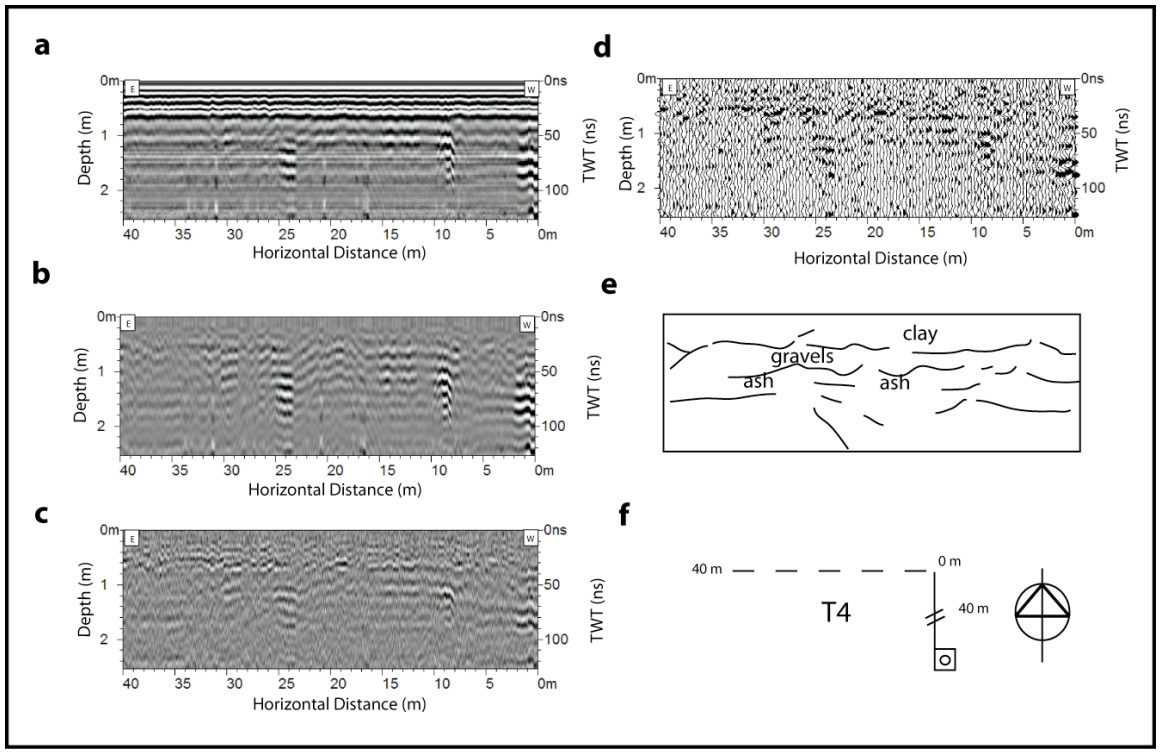

Figure 4.17: Transect 4, 2010 radargrams with geologic interpretation. (a) Raw, processed radargram. (b) Background removal and band – pass filter applied. (c) Background removal, band – pass and deconvolution filter applied. (d) Background removal, band – pass and deconvolution filter applied in wiggle display. (e) Interpretation. (f) Index map of T4 location in survey area.

across the profile at about 1.3 m depth. This is related to volcanic tuff unit and is interpreted as existing below the fossil zone. Data seen here confirms similar results to what was visualized in the Grid 6 data, however, this transect was collected from east to west, unlike the north – south transects mapped in the 2009 survey in the same location.

Transects 8 – 12

This area was over the visible fossil exposures to the maximum southern extent of the survey area. This encompasses the previous Grid 3 and 4 from the 2009 survey. The transects here are overlooking the cut bank exposure at the southern edge of the stream channel. Resulting data from the 2010 survey can be readily compared with that of the 2009 survey data. Figure 4.18a shows the raw profile from Transect 8. This image is similar to other raw data images throughout this study as horizontal banding noise is present at the top of the profile, between 0 to 1 m depth. Beyond this, there appears to be a series of horizontal bands generated from 80 ns to the bottom of the profile, located at 0 to 15 meters horizontal distance. Additional noise can be seen from 25 to 39 meters at the bottom of the profile, where a series of linear vertical bands stretch across the radargram at various distances. In all, the profile cannot be interpreted on the raw data images, and the reliance on post – processing and filtering is necessary in gleaning relevant information about the subsurface strata. Figure 4.18b shows the same data with an applied background and band – pass filter (low – pass: 210 MHz; high – pass: 23

MHz). This allows increased clarity of the data, especially at the top of the section where there is an undulatory contact between high – frequency clay sediments and the low – frequency gravel unit at roughly 60 cm depth. A strong, structurally coherent feature is present on the left (or easterly) side of the radargram toward the bottom of the profile. This is most likely the volcanic tuff unit appearing at the bottom of the section. This feature is more clearly seen in the background removal, band – pass and deconvolution – filtered data (Fig. 4.18c), which isolates the top of the reflection contact on the southern edge of the radargram. Toward the right side, or westerly direction, the continuity of the reflections dissipates quickly and it is uncertain if this feature is laterally continuous toward this side of the profile. Reflection patterns seen at the bottom of the section from roughly 2 – 3 m is likely related to the conglomeritic unit. Upon examination of the wiggle display of this data (Fig. 4.18d), subtle reflections viewed at the bottom of the radargram are more easily identifiable. The interpretation in Figure 4.18e shows the interpretation of the profile modeled after Figure 4.18d, the wiggle display. These data shows similar radar response with sedimentary units at Fanta and compare with interpretations performed on the 2009 data.

Transects 14 – 18

Transects 14 – 18 encompassed several 2009 grids: 13, 20 and 21. Data collected from this area was generally poorer quality and resolution than the data collected in 2009. This is especially true at the greatest depths of the profiles. Figure 4.19a is the raw profile. Like in most other raw images, horizontal banding noise has

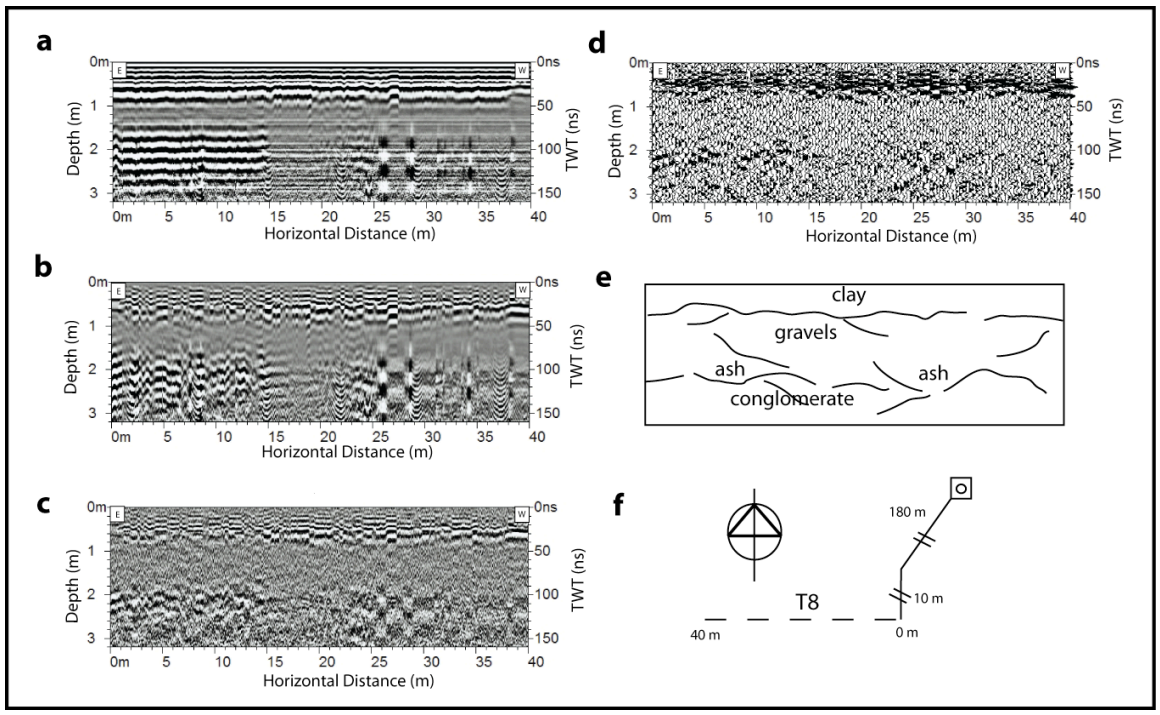

Figure 4.18: Transect 8, 2010 radargrams with geologic interpretation. (a) Raw, processed radargram. (b) Background removal and band – pass filter applied. (c) Background removal, band – pass and deconvolution filter applied. (d) Background removal, band – pass and deconvolution filter applied in wiggle display. (e) Interpretation. (f) Index map of T8 location in survey area.

masked possible data that may exist. This is present at 0 to 80 cm depth as low frequency horizontal banding that crosses the entire transect. Data past this beyond this depth range does not provide any useful data considering that the few reflections here are weakly identifiable. In the next image (Fig. 4.19b), much of the horizontal banding noise has been eliminated after the application of background removal and band-pass filtering (low – pass: 528 MHz; high – pass: 19 MHz), allowing for clarity of reflections seen in the uppermost part of the section (0 – 80 cm). Between 0 and 30 cm, multiple high – frequency reflections are apparent that was previously masked by banding noises. This is similar in coherency to what was interpreted as the clay capstone unit in the 2009 data. From 50 – 90 cm, some weakly reflective units can be seen. This area is interpreted as the gravel and fossil – bearing unit. There is a general lack of reflection continuity at this depth. This is better visualized in Figure 4.19c, where the wiggle display of the same data is presented. From greater than 1 m depth, it appears as though no coherent amplitude information is present that can be interpreted. This may be a result of attenuation effects or environmental problems related with sediment saturation. The reflections and strong amplitudes at the bottom of the section appear linearly across the profile, and is suspect of a potential relation to noise effects. This is particularly apparent at 1.4 depth along the 27 – 30 meter horizontal distance axis. The most informative data is highlighted in Figure 4.19d, where the wiggle display with applied background, band – pass and deconvolution – filters is presented. In this view, the amplitudes below 0.5 m depth appear in a easily interpretable.

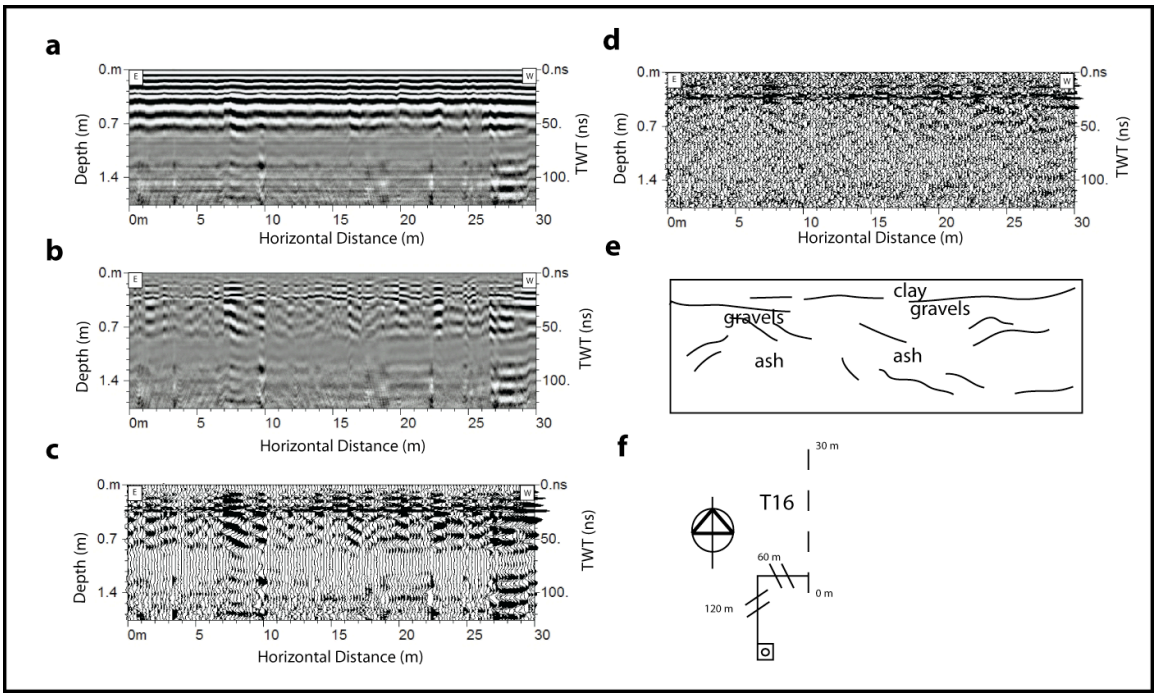

Figure 4.19: Transect 16, 2010 radargrams with geologic interpretation. (a) Raw, processed radargram. (b) Background removal and band – pass filter applied. (c) Background removal and band – pass filter applied in wiggle display. (d) Background removal, band – pass and deconvolution filter applied in wiggle display. (e) Interpretation. (f) Index map of T16 location in survey area.

Transects 19 – 23

Transects 19 – 23 are on the eastern side of the Fanta River, located in the vicinity of Grid 8 and expanding in the easterly direction of the bounding area of Grid 8. Data presented here follows the order of other figures. Figure 4.20a shows raw, processed data. As seen here, there is strong horizontal banding noise that is likely a result of airwave interference. This occurs from 0 – 1.7 m depth. Additionally, horizontal banding noise is also seen at greater depths, especially to the extreme western portion of the profile, at 32 – 40 meters horizontal distance. Various hyperbolic features are present in parts of the section that are visible. Figure 4.20b shows the background removal and band – pass filtered data (low – pass: 107 MHz; high – pass: 24 MHz). The entire section appears to be free of the horizontal banding noise seen in the previous image. Here, a high frequency zone with strong amplitudes can be seen from roughly 20 cm – 1 m depth. This likely relates to the clay capstone unit, as it appears first stratigraphically. Below this, a zone weaker amplitude and coherency reflections appear at 1.5 – 3 m depth. This is most likely related to the gravel unit, possibly containing fossiliferous deposits. The western portion of this radargram (between 30 – 40 meters horizontal distance) appears to be dominated by a high amplitude and high frequency waveforms at 3.2 m depth. Considering the geometry of these features, the reflections may be a result of multiple noise. The following images (Figs. 4.20c and 4.20d) are a result of the previous processing and filtering steps, but with the deconvolution filter applied. Here, generally two major reflective units can be seen, the upper clay unit at roughly 1 m depth and a lower, horizontal feature at roughly 3 m depth. The lowermost

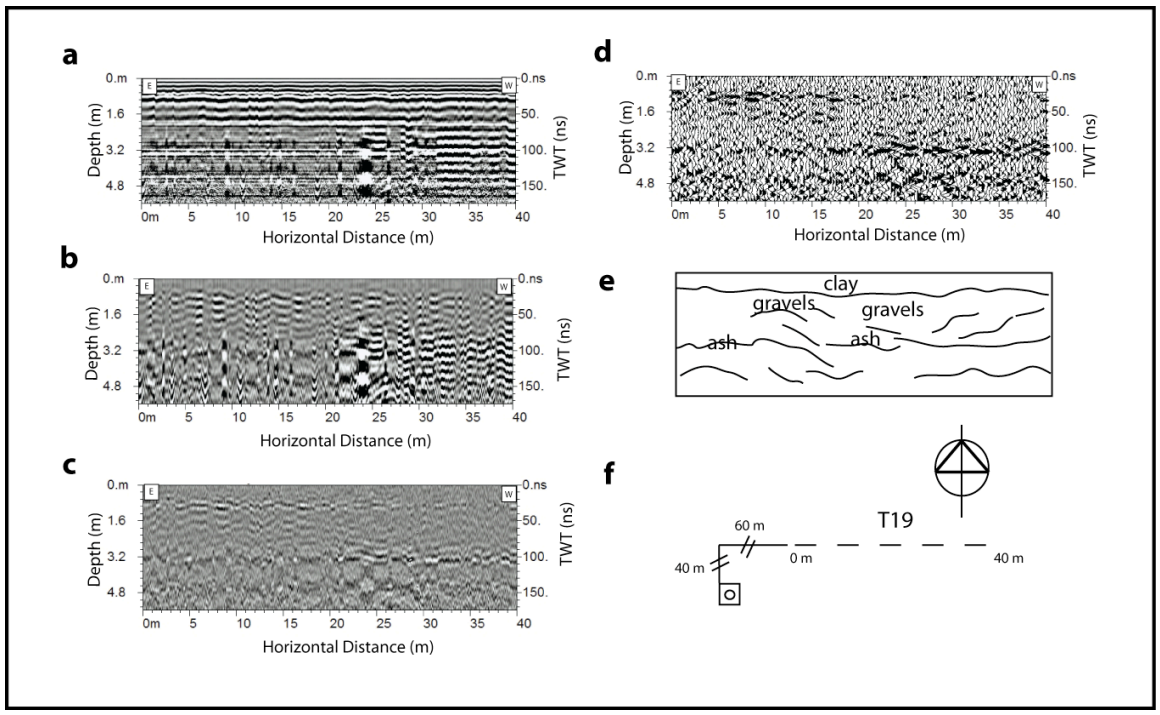

Figure 4.20: Transect 19, 2010 radargrams with geologic interpretation. (a) Raw, processed radargram. (b) Background removal and band – pass filter applied. (c) Background removal, band – pass and deconvolution filter applied. (d) Background removal, band – pass and deconvolution filter applied in wiggle display. (e) Interpretation. (f) Index map of T19 location in survey area.

feature below 3.5 m may relate to the water table at the site due to its relatively horizontal reflection pattern. This feature is not interpreted as stratigraphy, however reflections above this interface most likely relate to the gravel (fossil - containing unit), clay and tuff units. The disrupted cross bedding apparent here indicates the variable stratal architecture apparent in the radar profiles.

CHAPTER V

DISCUSSION AND CONCLUSIONS

Data obtained from the 2009 and 2010 surveys provided a mechanism with which to understand the geophysical, geological and hydrological components of the Fanta Stream Site, satisfying the primary objectives of this research. These data were then processed and interpreted to make inferences about the geological and stratigraphic evolution of the Fanta Stream Site. With regard to developing GPR for paleontological reconnaissance, this is a new utilization of this technology and is particularly novel in east Africa. As demonstrated in Chapter IV, GPR provided images of the subsurface deposits at Fanta in an attempt to understand the location and extent of the fossil bone beds together with that of adjacent stratigraphy.

Although two fossiliferous units exist at the site, only the uppermost fossil layer could be visualized with the equipment during the field surveys. This is due to many reasons. Stratigraphically, the site is generally made up of materials that have high dielectric values, including clays ($\varepsilon = 5 – 40$) and volcanic tuff ($\varepsilon = 4 – 7$). These materials cause attenuation effects at depth, and signal is rapidly consumed by noise in the lower portion of the profiles throughout many of the transects collected in both 2009 and 2010 surveys. Considering the appearance of these materials above the lower paleontological or 'bone' unit, the amount of EM energy required to transmit to this depth is insufficient to resolve geological units at this depth. Even with an increased time window (or range) of 500 ns, resulting data does not allow

for a reliable interpretation of reflections below 150 ns depth or roughly 4 meters. The complexity of stratigraphy at the site further complicates the ability to image stratigraphic contacts at greater depths. This may be a result of low dielectric contrast at the interface of deeper earth materials. The velocity of propagated radar waves declines rapidly at depth, which accounts for another problem in visualizing reflection patterns toward the bottom of the profiles. Additionally, the effect of water related to seasonal variability between 2009 and 2010 surveys played a major role considering the variability of resolution in lower portions of the radar profiles.

Differing environmental conditions during the 2009 verses 2010 survey had a large effect on the data quality and resolution throughout. This is expressed most apparently in the deeper portions of the radargrams, generally below 150 ns depth. In the 2009 data, this portion of the radargram spectrum is dominated by noise, where no coherent reflection patterns could be imaged. Figure 5.1 shows a comparison of the 2009 and 2010 data at 250 ns depth (512 samples). As seen here, noisy conditions affect the 2009 data at roughly 150 ns depth (Fig. 5.1a), whereas in 2010, noise at the bottom of the section is present at approximately 200 ns or 5 meter depth (Fig. 5.1b). This most is most likely related to the water table present at those depths. Conditions related to water content can greatly affect surveying conditions and were considered when interpreting final sections. 2009 data generally show poor resolution in samples at greater depths than 4 meters (150 ns), where amplitude values are large, causing problems in the application of interpretation. All of the final images in Chapter IV have thus been truncated to

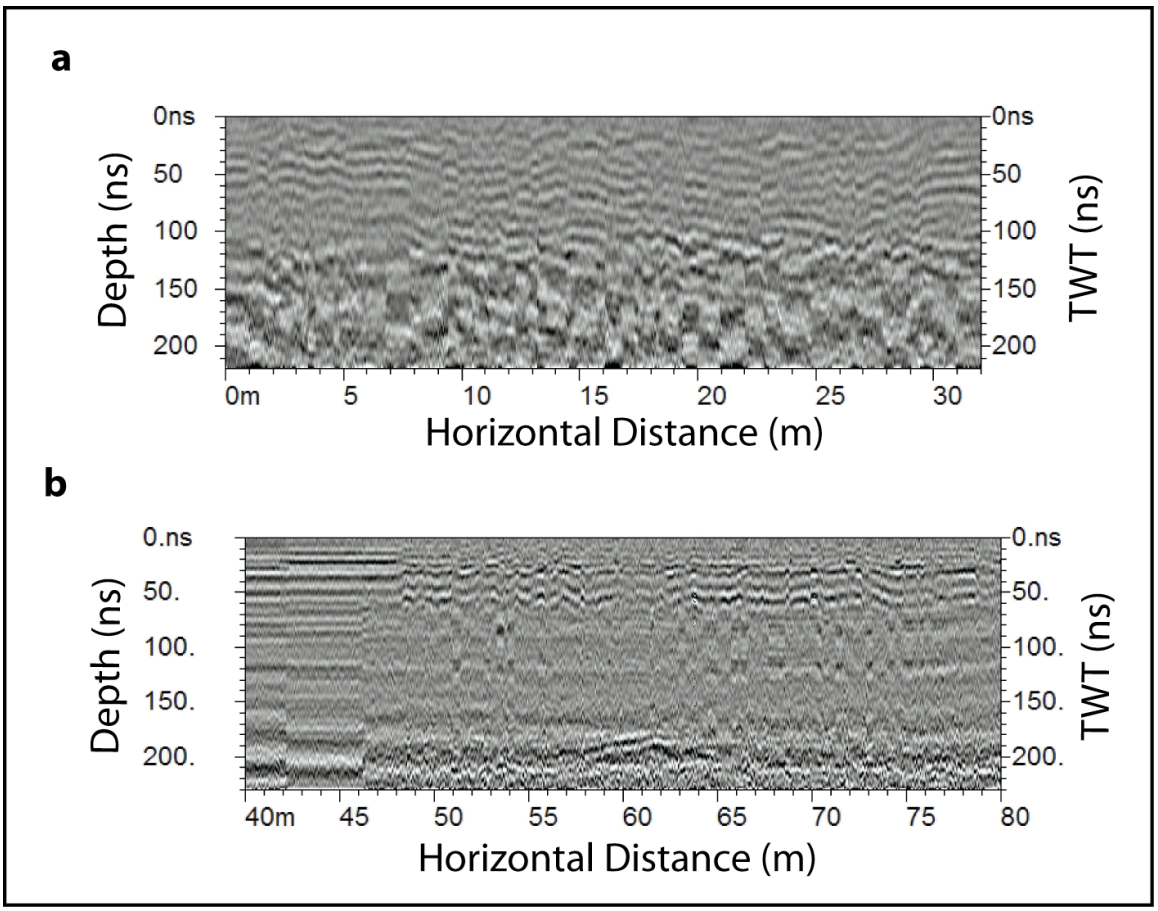

Figure 5.1: Comparison of 2009 verses 2010 radargrams. (a) 2009 radargram example (Grid 6, line 1). (b) 2010 radargram example (Transect 2).

highlight the best data resolution, generally only showing the 0 – 150 ns depth range. The differences between the two datasets most likely relate to moisture content at the sites during each survey.

Seasonal episodes vary in this region of Ethiopia, especially during the summer rainy season known as "Kiremt" which occurs from June – September (Fig. 5.2). This is primarily controlled by the seasonal migration of the Inter Tropical Convergence Zone (ITCZ), which appears in northern Ethiopia during this time (Legesse, et al., 2003: 73). Kiremt is a boreal, monsoonal summer rain that accounts for 65 – 95 percent of total annual rainfall throughout the country (Segele and Lamb, 2005: 154). Although the 2009 GPR surveys were conducted during this cycle, it was not expected to have a substantial impact on the survey, considering only the presence of isolated rain showers during a few survey periods. The dry period extends between October and February (known locally as "baga"), during which time the ITCZ migrates to the south of Ethiopia. Additionally, a small rainy season ("belg") occurs from March to May when the ITCZ moves from south to north across the country (Legesse, et al., 2003: 73). This climate pattern is referred to as 'bimodel,' due to short, spring rains and long, summer Kirmt rains, without a pronounced dry period in between (Meze – Hausken, 2004: 21). Despite the interannual variability of Kiremt rainfall, the rainy season has affected the data with regard to the two surveys. The effect of this seasonal variability at the Fanta site was described by Lanzarone, et al. (2010).

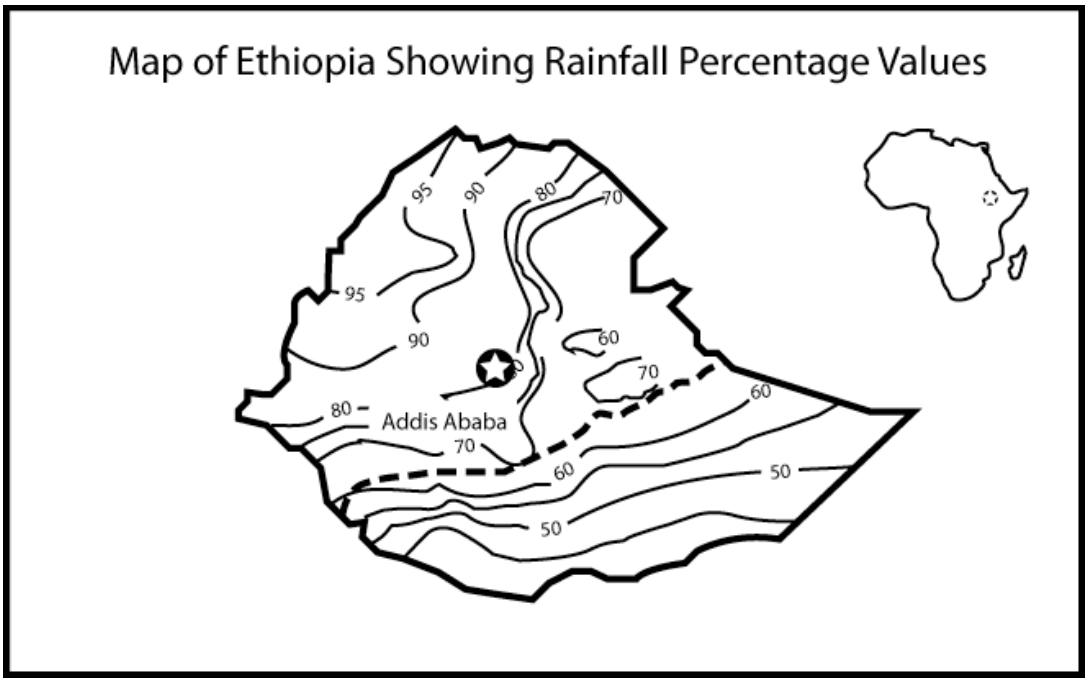

Figure 5.2: Average percentage of annual rainfall during the months of May – October. North of the dashed line, the rainy season (Kiremt) occurs during July – September, whereas areas to the south have maximum rainfall in April and October, with virtually no rain during the summer months. (Modified from Segele and Lamb, 2005: 154).

Velocity analysis was an extremely important aspect of this study. Traditionally, archaeological GPR studies have little discrimination to relating buried anomalous features to real depths (Conyers and Goodman, 1997: 107). However, considering this study utilized GPR in order to map geological units, related radar reflections to absolute depth in meters was a foremost concern in developing a high – resolution model of the subsurface. Using a variety of methods outlined in Chapter III, an acceptable velocity value was calculated and extended for both 2009 and 2010 datasets.

An additional objective of this study was to introduce ground penetrating radar as a geophysical and archaeological tool to the local Ethiopian scientific community. Several talks by the author were held throughout the region in disseminating information regarding GPR theory and applications. This included talks at the Geological Survey of Ethiopia (2009), Addis Ababa University (2009), Wolayta Sodo University (2010) and Sanford International School (2010).

Conclusion

The broad discipline of archaeological geology utilizes earth science techniques in resolving archaeological questions. The GPR and coring survey performed throughout this Thesis is only a small manifestation of this field that is constantly growing as new approaches and techniques emerge. The documented importance of the Fanta site highlights the value of preserving this resource for future generations of scientists, students and the local communities. The fossil finds at Fanta have the potential to make this site a major cultural and natural resource

and directly contribute to our broad understanding of human evolution. The proximity of this site to the urban sprawl of Addis Ababa offers unparalleled opportunities to educate the public about the rich heritage of Ethiopia and to encourage tourism. Various threats due to population pressure, development projects and agricultural practices has forced the Fanta site to undergo a rapid undertaking of study and research before the site is potentially destroyed. It is hoped that this Thesis will serve in the greater understanding of spatially defining this site for future excavations and a greater geological understanding of the site in general. Additionally, this study has shown the powerful ability of using GPR in the context of aiding in fossil recovery and paleontological exploration. This is demonstrated by stratal interpretations on radargram profiles and time slices. A final map appearing in Figure 5.3 shows the combined GPR results in the survey to show the approximated locations of the fossil deposits and serves as a final image with which to utilize in protecting the site. In this figure, the entire surveyed area is suspected to contain the fossil – bearing gravel unit. This is based on similar reflection patterns of the low coherency unit seen throughout the presented profiles. The fossil area documented here thus greatly increases the approximate size of the site by roughly 100 meters in the westerly direction and 50 meters in the easterly direction. The site could additionally extend much farther, although its maximum extent is unknown until the site becomes excavated in these areas.

Future work at the Fanta site can be recommended based on the results from this Thesis. This includes extensive excavation in the delineated areas provided by the GPR and core surveys. Considering the utility of GPR analyses at Fanta, the

Figure 5.3: Composite map highlighting areas of high interest in future fossil excavation planning (white dashed line) over the 2008 survey map generated by Bobe and Assefa (Assefa, et al., 2008).

application of this technique applied to the Gemeda and Koche sites would provide additional spatial sampling that could aid in the delineation of fossil areas.

Finally, the application of GPR as demonstrated here may help to understand the deposition of fossils and the evolution of other fluvial sites in Africa at large. It is hoped that the application of shallow geophysical analyses can be useful at many archaeological sites in this region in allowing for a better understanding of inter – site stratification and the identification of dense fossil areas.

REFERENCES CITED

Abdallatif, T., Mousa, S. and Elbassiony, A. 2003. Geophysical Investigation for Mapping the Archaeological Features at Qantir, Sharqyia, Egypt. *Archaeological Prospection* **10**: 27 – 42.

Annan, A., 2009. Electromagnetic Principles of Ground Penetrating Radar. *In* Jol, H. ed., Ground Penetrating Radar: Theory and Applications. Elsevier, Oxford.

Asfaw, B., White, T., Lovejoy, O., Latimer, B., Simpson, S. and Suwa, G. 1999. *Australopithecus garhi*: A New Species of Early Hominid from Ethiopia. *Science* **284**: 629 – 635.

Asfaw, B., Gilbert, H., Beyene Y., Hart, W., Rennell, P., WoldeGabriel, Vrba, E. and White, T. 2002. Remains of Homo Erectus from Bouri, Middle Awash, Ethiopia. *Nature* **416**: 317 – 320.

Arthur, J., Lakew, B. and Curtis, M. 2009. Historical Archaeology and Oral Tradition in the Gamo Highlands of Southern Ethiopia. Paper presented at the 74th Annual Meeting of the Society for American Archaeology, Atlanta, GA.

Assefa, Z., Bobe, R. and Lepre, C. 2008. Field Report on the 2008 Rescue Paleoanthropology Project: Fanta, Gemeda and Koche. Unpublished Report on file at Authority of Research and Conservation of Cultural Heritage, Government of Ethiopia, Addis Ababa, Ethiopia.

Baker, G., Steeples, D., Schmeissner, C., Pavlovic, M. and Plumb, R. 2001. Near – surface imaging using coincident seismic and GPR data. *Geophysical Research Letters* **28**: 627 – 630.

Baker, G, Jordan, T. and Pardy, J. 2007. An introduction to ground penetrating radar (GPR). *In* Baker, G. and Jol, H., eds., Stratigraphic Analyses Using GPR: *Geological Society of America Special Paper* **432**: 1 – 18.

Brandt, S., Hildebrand, E. and Fisher, E. 2007. Field Report on the 2007 Excavations at Moche Borago Rock Shelter. Unpublished report on file at the Authority for Research and Conservation of Cultural Heritage, Government of Ethiopia, Addis Ababa, Ethiopia.

Bristow, C. 2009. Ground Penetrating Radar in Aeolian Dune Sands. *In* Jol, H. ed. Ground Penetrating Radar: Theory and Applications. Elsevier, Oxford.

Cardarelli, E., Marrone, C. and Orlando, L. 2003. Evaluation of tunnel stability using integrated geophysical methods. *Journal of Applied Geophysics* **52**: 93 – 102.

Casana, J., Herrmann, J. and Fogel, A. 2008. Deep Subsurface Geophysical Prospection at Tell Qarqur, Syria. *Archaeological Prospection* **15**: 207 – 225.

Cassidy, N. 2009. Ground Penetrating Radar Data Processing, Modeling and Analysis. *In* Jol, H. ed. Ground Penetrating Radar: Theory and Applications. Elsevier, Oxford.

Cassidy, N. 2008. GPR Attenuation and Scattering in a Mature Hydrocarbon Spill: A Modeling Study. *Vadose Zone Journal* **7**: 140 – 15.

Chow, J., Chang, S. and Yu, H. 2006. GPR reflection characteristics and depositional models of mud volcanic sediments – Wushanting mud volcano field, southwestern Taiwan. *Journal of Applied Geophysics* **60**: 179 – 200.

Conyers, L. 2004. *Ground – Penetrating Radar for Archaeology*. Altamira Press, Walnut Creek.

Conyers, L. and Goodman, D. 1997. *Ground Penetrating Radar: An Introduction for Archaeologists*. Altamira Press, Walnut Creek, London and New Delhi.

Crossley, R. 1984. Controls of sedimentation in the Malawi Rift Valley, Central Africa. *Sedimentary Geology* **40**: 33 – 50.

Daniels, D. 2009. Antennas. *In* Jol, H., ed. Ground Penetrating Radar: Theory and Applications. Elsevier, Oxford.

Deiana, R., Cassiani, G., Villa, A., Bagliani, A and Bruno, V. 2008. Calibration of a Vadose Zone Model Using Water Injection Monitored by GPR and Electrical Resistance Tomography. *Vadose Zone Journal* **7**: 215 – 226.

Derobert, X. and Abraham, O. 2000. GPR and seismic imaging in a gypsum quarry. *Journal of Applied Geophysics* **45**: 157 – 169.

Dobrin M. and Savit C.1988. *Introduction to Geophysical Prospecting*. McGraw – Hill, New York.

Doolittle, J. and Butnor, J. 2009. Soils, Peatlands, and Biomonitoring. *In* Jol, H., ed. Ground Penetrating Radar Theory and Applications. Elsevier, Oxford.

Edwards, W. Okita, M. and Goodman, D. 2000. Investigation of a Subterranean Tomb in Miyazaki, Japan. *Archaeological Prospection* **7**: 215 – 224.

Ernenwein, E. and Kvamme, K. 2008. Data Processing issues in Large – area GPR Surveys: Correcting Trace Misalignments, Edge Discontinuities and Striping. *Archaeological Prospection* **15**: 133 – 149.

Gaffney, C. 2008. Detecting Trends in the Prediction of the Buried Past: A Review of Geophysical Techniques in Archaeology. *Archaeometry* **50**: 313 – 336.

Garrison, E. 2003. *Techniques in Archaeological Geology.* Springer – Verlag, Berlin, Heidelberg, New York.

Geleta, K., 2009. Rapid Antiquities Conservation Undertaking. Unpublished report on file at the Authority for Research and Conservation of Cultural Heritage, Government of Ethiopia, Addis Ababa, Ethiopia.

Geophysical Survey Systems, Inc. (GSSI) 1995a. *SIR SYSTEM – 2 Training Notes*. GSSI, New Salem, NH.

Geophysical Survey Systems, Inc. (GSSI) 1995b. *Manual for SIR SYSTEM – 2*. GSSI, New Salem, NH.

Getahun, A. 2009. *Personal Communication*. Geological mapping provided by Getahun in 2007 as part of the Geological Survey of Ethiopia identified locally well – known surficial deposits at Fanta during the 2009 GPR surveys.

Getahun, A. 2007. Geology of Addis Ababa City. Unpublished report on file at the Ministry of Mines and Energy Regional Geology and Geochemistry Department. Addis Ababa.

Ghose, R. and Slob, E. 2006. Quantitative integration of seismic and GPR reflections to derive unique estimates for water saturation and porosity in subsoil. *Geophysical Research Letters* **33**: 1 – 4.

Gomez, C., Lavigne, F., Hadmoko, D., Lespinasse, N. and Wassmer, P. 2009. Block – and – ash flow deposition: A conceptual model from a GPR survey on pyroclastic – flow deposits at Merapi Volcano, Inonesia. *Geomorphology* **110**: 118 – 127.

Gomez – Ortiz, D., Matrin – Velazquez, S., Martin – Crespo, T., Marquez, A., Lillo, J., Lopez, I. and Carreno, F. 2006. Characterization of volcanic materials using ground penetrating radar: A case study at Teide volcano (Canary Islands, Spain). *Journal of Applied Geophysics* **59**: 63 – 78.

Goodman, D. 2010. *GPR SLICE User's Manual Version 7.0.* Geophysical Archaeometry Laboratory. Gypsy Lane, CA.

Goodman, D., Piro, S., Nishimura, Y., Schneider, K, Hongo, H., Higashi, N., Steinberg, J. and Damiata, B. 2009. GPR Archaeometry. *In* Jol, H., ed. Ground Penetrating Radar: Theory and Applications. Elsevier, Oxford.

Grasmueck, M., Weger, R. and Horstmeyer, H. 2005. Full – resolution 3D GPR imaging. Geophysics **70**: 13 – 19.

Hayakawa and Kawanaka, 1998. Radar imaging of underground pipes by automated estimation of velocity distribution versus depth. *Journal of Applied Geophysics* **40**: 37 – 48.

Hildebrand, J., Wiggins, S., Henkart, P. and Conyers, L. 2002. Comparison of Seismic Reflection and Ground – penetrating Radar Imaging at the Controlled Archaeological Test Site, Champaign, Illinois. *Archaeology Prospection* **9**: 9 – 21.

Jutzi, S. 1988. Deep Black Clay Soils (Vertisols): Management Options for the Ethiopian Highlands. *Mountain Research and Development* **8**: 153 – 156.

Johanson, D. and Edey, M. 1981. *Lucy: The Beginnings of Humankind*. Warner Books, Inc. New York.

Jol, H., Smith, D. and Meyers, R. 1996. Digital Ground Penetrating Radar (GPR): A New Geophysics Tool for the Coastal Barrier Research (Examples from the Atlantic, Gulf and Pacific Coasts, U.S.A.). *Journal of Coastal Research* **12**: 960 – 968.

Jol, H. 1995. Ground penetrating radar antenna frequencies and transmitter powers compared for penetration depth, resolution and reflection continuity. *Geophysical Prospecting* **43**: 693 – 709.

Jones, B. 2011. *Personal Communication*. Geophysical Survey Systems, Inc. New Salem, NH.

Kamei, H., Atya, M., Abdallatif, T., Mori, M. and Hemthavy, P. 2002. Ground – penetrating Radar and Magnetic Survey to the West of Al – Zayyan Temple, Kharga Oasis, Al – Wadi Al – Jadeed (New Valley), Egypt. *Archaeological Prospection* **9**: 93 – 104.

Kingdon, J. 1997. The Kingdon Field Guide to African Mammals. A&C Black Publishers Ltd., London.

Knight, R., Tercier, P. and Irving, J. 2004. The effect of vertical measurement resolution on the correlation structure of a ground penetrating radar image. *Geophysical Research Letters* **31**: 1 – 4.

Kvamme, K. 2003. Geophysical Surveys as Landscape Archaeology. *American Antiquity* **68**: 435 – 457.

Lanzarone, P. 2010. Field Report on the 2009 Ground Penetrating Radar (GPR) Examinations at the Fanta Stream Site. Unpublished report on file at the Authority for Research and Conservation of Cultural Heritage, Government of Ethiopia, Addis Ababa, Ethiopia.

Lanzarone, P.; Garrison, E. and Getahun, A. 2010. Multi – Seasonal Ground – Penetrating Radar (GPR) Analyses at the Fanta Stream Fossil and Archaeological Site, Central Ethiopia. Geological Society of America Abstracts with Program 42: 578.

Legesse, D., Vallet – Coulomb, C. and Gasse, F. 2002. Hydrological response of a catchment to climate and land use changes in Tropical Africa: case study South Central Ethiopia. *Journal of Hydrology* **275**: 67 – 85.

Lepre, C. 2010. *Personal communication*. Sediment dating provided by Lepre as part of the Rescue Paleoanthropology Project. Lamont – Doherty Earth Observatory, Columbia University. Palisades, NY.

Longley, P., Goodchild, M., Maguire, D. and Rhind, D. 2005. *Geographic Information Systems and Science*. Second Edition. John Wiley & Sons, Ltd. West Sussex.

Lunt, I., Hubbard, S and Rubin, Y. 2005. Soil moisture content estimation using ground – penetrating radar reflection data. *Journal of Hydrology* **307**: 254 – 269.

Main, D. and Hammon, W. 2003. The application of Ground Penetrating Radar as a mapping technique at vertebrate fossil excavations in the Cretaceous of Texas. *Cretaceous Research* **24**: 335 – 345.

Meze – Hausken, E. 2002. Contrasting climate variability and meteorological drought with perceived drought and climate change in northern Ethiopia. *Climate Research* **27**: 19 – 31.

Milsom, J. 1996. *Field Geophysics*. Second Edition. John Wiley & Sons, West Sussex.

Mohr, P. 1966. Geological report on the Lake Langano and adjacent plateau regions. *Bulletin of the Geophysical Observatory Addis Ababa* **9**: 59 – 75.

Neal, A. 2004. Ground – penetrating radar and its use in sedimentology: principles, problems and progress. *Earth – Science Reviews* **66**: 261 – 330.

Neto, P. and Medeiros, W. 2006. A practical approach to correct attenuation effects in GPR data. *Journal of Applied Geophysics* **59**: 140 – 151.

Neuendorf, K., Mehl, J. and Jackson, J. 2005. *Glossary of Geology*. Fifth Edition. American Geological Institute, Alexandria.

Noon, D., Stickley, G. and Longstaff, D. 1998. A frequency – independent characterization of GPR penetration and resolution performance. *Journal of Applied Geophysics* **40**: 127 – 137.

Nuzzo, L. 2003. Coherent noise attenuation in GPR data by linear and parabolic Radon Transform techniques. *Annals of Geophysics* **46**: 533 – 547.

Olhoeft, G. 1996. Application of Ground Penetrating Radar. *In* Proceedings of the Sixth International Conference on Ground Penetrating Radar (GPR'96), September 30 – October 3, 1996, Department of Science and Technology, Tohoku University, Sendai, Japan, 1 – 4.

Orlando, L. and Soldovieri, F. 2007. Two different approaches for applying georadar processing: A case study in archaeological prospecting. *Journal of Applied Geophysics* **64**: 1 – 13.

Park, R. 1997. *Foundations of Structural Geology*. Third Edition. Routledge, London and New York.

Pyke, K., Eyubolglu, S., Daniels, J. and Vendl, M. 2008. Controlled Experiment to Determine the Water Table Response Using Ground Penetrating Radar. Journal of Environmental and Engineering Geophysics 13: 335 – 342.

Russell, J. and Stasiuk, M 1997. Characterization of volcanic deposits with ground – penetrating radar. *Bulletin of Volcanology* **58**: 515 – 527.

Rust, A. and Russell, J. 2000. Detection of welding in pyroclastic flows with ground penetrating radar: insights from field and forward modeling data. *Journal of Volcanology and Geothermal Research* **95**: 23 – 34.

Saarenketo, T. 1998. Electrical Properties of water in clay and silty soils. *Journal of Applied Geophysics* **40**: 73 – 88.

Schneider, K. 2011. *Personal Communication*. Underground Imaging Solutions, Inc., Gainesville, GA.

Schwamborn, G., Dix, J., Bull, J. and Rachold, V. 2002. High – resolution Seismic and Ground Penetrating Radar – Geophysical Profiling of a Thermokarst Lake in the Western Lena Delta, Northern Siberia. *Permafrost and Periglacial Processes* **13**: 259 – 269.

Segele, Z. and Lamb,P. 2005. Characterization and variability of Kiremt rainy season over Ethiopia. *Meteorology and Atmospheric Physics* **89**: 153 – 180.

Seren, A., Gelisli and Catakli, A. 2008. A Geophysical Investigation of the Late Roman Underground Settlement at Aydintepe, Northeast Turkey. *Geoarchaeology: An International Journal* **23**: 842 – 860.

Shaaban, F. and Shaaban, F. 2001. Use of two – dimensional electric resistivity and ground penetrating radar for archaeological prospecting at the ancient capital of Egypt. African Earth Sciences 33: 661 – 671.

Sharma, P. 2002. *Environmental and Engineering Geophysics*. Cambridge University Press, Cambridge.

Sheriff, R. 2006. *Encyclopedic Dictionary of Applied Geophysics*. Forth Edition. Society of Exploration Geophysicists, Tulsa.

Stokes, P. and Laub, R. 2006. Using Ground Penetrating Radar (GPR) to find Pleistocene Megafauna Fossils at the Hiscock Site in Western New York. *Geological Society of America Abstracts with Programs*: **38**: 2.

Thompson, M., Elnaiem, D., Ashford, R and Conner, S. 1999. Towards a kala azar risk map for Sudan: mapping the potential distribution of *Phlebotomus orientalis* using digital data of environmental variables. *Tropical Medicine and International Health* **4**: 105 – 113.

Tohge, M., Karube, F. Kobayasi, M, Tanaka, A and Ishii, K. 1998. The use of ground penetrating radar to map an ancient village buried by volcanic eruptions. *Journal of Applied Geophysics* **40**: 49 – 58.

Vandenberghe, J. and van Overmeeren, R. 1999. Ground penetrating radar images o selected fluvial deposits in the Netherlands. *Sedimentary Geology* **128**: 245 – 270.

Vaughan, C. 1986. Ground – penetrating radar survey used in archaeological investigations. *Geophysics* **51**: 595 – 604.

Winter, J. 2001. *An Introduction to Igneous and Metamorphic Petrology*. Prentice Hall, New Jersey.

Witten, A., Levy, T., Adams, R. and Won, I. 2000. Geophysical Surveys in the Jebel Hamrat Fidan, Jordan. *Geoarchaeology: An International Journal* **15**: 135 – 150.

White, T., Asfaw, B., DeGusta, D., Gilbert, H., Richards, G., Suwa, G. and Howell, F. 2003. Pleistocene *Homo sapiens* from Middle Awash, Ethiopia. *Nature* **423**: 742 – 747.

WoldeGabriel, G., Haile – Salassie, Y., Renne, P., Hart, W., Ambrose, S., Asfaw, B., Heiken, G. and White, T. 2001. Geology and palaeontology of the Late Miocene Middle Awash valley, Afar rift, Ethiopia. *Nature* **412**: 175 – 178.

Zeng, X and McMechan, G. 1997. GPR characterization of buried tanks and pipes. *Geophysics* **62**: 797 – 806.

APPENDIX A

PREVIOUS DELINEATIONS OF THE FANTA SITE

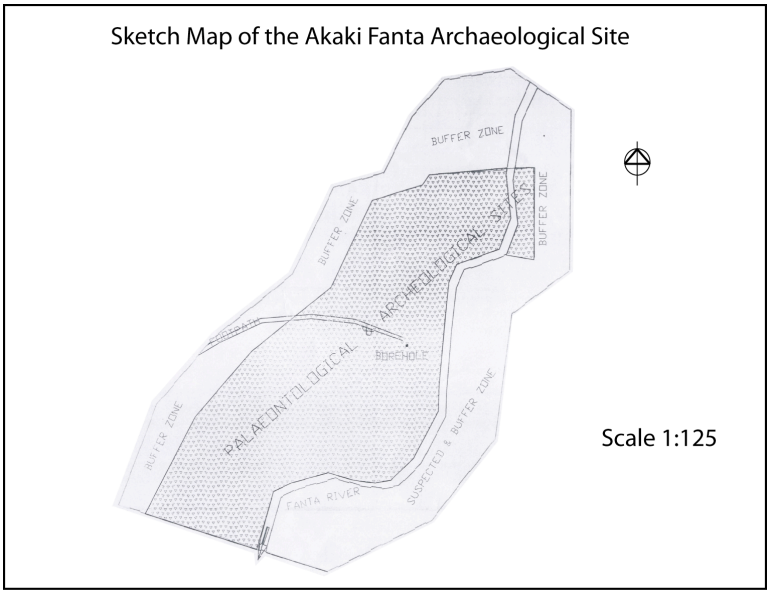

(Modified from Geleta, 2009)

APPENDIX B

GPS CONTROL POINT DATA

2009 Control Points

Lat+	Long+	Point	Feature	Date
8.88231	38.80065	59	Control Well	6/6/09
8.88229	38.80065	60	Control Well	6/7/09
8.88225	38.80079	61	Edge of Exposed Bones from Well	6/7/09
8.88226	38.80078	62	Edge of Stream from Well	6/7/09
8.88257	38.80056	63	Grid 1 : SW Corner	6/7/09
8.8827	38.8006	64	Grid 1 : NW Corner	6/7/09
8.88274	38.80069	65	Grid 1 : SE Corner	6/7/09
8.88266	38.80073	66	Grid 1 : NW Corner	6/7/09
8.88257	38.80063	67	Grid 2: SE corner	6/7/09
8.8829	38.80021	68	Grid 2: NE corner	6/7/09
8.8829	38.80022	69	Grid 2: NW corner	6/7/09
8.88254	38.80025	70	Grid 2: SW corner	6/7/09
8.8823	38.80065	71	Control Well	6/7/09
8.88916	38.80075	72	Edge of Grid 4	6/7/09
8.8823	38.80066	73	Control Well	6/7/09
8.88115	38.79963	74	Grid 3: SE Corner	6/8/09
8.88116	38.79954	75	Grid 3: SW Corner	6/8/09
8.8815	38.79954	76	Grid 3: NW Corner	6/8/09
8.88151	38.79964	77	Grid 3: NE Corner	6/8/09
8.88145	38.79961	78	Rod for Depth Calibration (G3)	6/8/09
8.88119	38.79916	79	Grid 4: SW Corner	6/8/09
8.88116	38.79954	80	Grid 4: SE Corner	6/8/09
8.88144	38.79956	81	Grid 4: NE Corner	6/8/09
8.88145	38.79956	82	Grid 4: NW Corner	6/8/09
8.8815	38.7996	83	Grid 4: NW Corner	6/9/09
8.88151	38.79953	84	Grid 5: NE Corner	6/9/09
8.88151	38.79953	85	Grid 5: NW Corner	6/9/09
8.88122	38.79926	86	Grid 5: SW Corner	6/9/09
8.88117	38.79953	87	Grid 5: SE Corner	6/9/09
8.88228	38.80063	88	Control Well	6/10/09
8.88259	38.8006	89	Grid 6: NE corner	6/10/09
8.88225	38.80029	90	Grid 6: NW corner	6/10/09
8.88225	38.80028	91	Grid 6: SW corner	6/10/09
8.88153	38.79973	92	Grid 6: SE corner - well	6/10/09

8.8796621	38.798709		Grid 7: SW corner	6/10/09
8.88152	38.79971	93	Grid 7: SE corner	6/10/09
8.88199	38.79951	94	Grid 7: NE corner	6/10/09
8.88228	38.80069	95	Grid 7: NW corner	6/10/09
8.88265	38.80143	96	Grid 8: NE corner	6/11/09
8.88263	38.80101	97	Grid 8: SE corner	6/11/09
8.88263	38.80101	98	Grid 8: SW corner	6/11/09
8.88296	38.80106	99	Grid 8: NW corner	6/11/09
8.88168	38.79955	100	Grid 9: SE corner	6/11/09
8.88168	38.79947	101	Grid 9: NE corner	6/11/09
8.88152	38.79941	102	Grid 9: NW corner	6/11/09
8.88152	38.79941	103	Grid 9:SW corner	6/11/09
8.88264	38.80102	104	Grid 10: SW Corner	6/12/09
8.88299	38.80125	105	Grid 10: SE Corner	6/12/09
8.88302	38.80107	106	Grid 10: NE Corner	6/12/09
8.88302	38.80107	107	Grid 10: NW corner	6/12/09
8.883	38.8011	108	Grid 11: NE corner	6/12/09
8.88120077	38.80056		Grid 11: SE corner	6/12/09
8.881119	38.800518		Grid 11: SW corner	6/12/09
8.881128	38.80025		Grid 11: NW corner	6/12/09
8.88402	38.80125	109	Grid 12: SW corner	6/13/09
8.882159	38.8004		Grid 12: SE corner	6/13/09
8.882195	38.80007		Grid 12: NE corner	6/13/09
8.881843	38.8		Grid 12: NW corner	6/13/09
8.88371	38.80069	110	Grid 13: SW corner	6/13/09
8.88406	38.80068	111	Grid 13: NW corner	6/13/09
8.88405	38.80089	112	Grid 13: NE corner	6/13/09
8.88405	38.80088	113	Grid 13: SE corner	6/13/09
8.88151	38.79963	114	Core 1	6/14/09
8.88151	38.79963	115	Core 2	6/14/09
8.88152	38.79953	116	Core 3	6/14/09
8.88156	38.79947	117	Core 4	6/14/09
8.8817	38.79927	118	Core 5	6/15/09
8.88171	38.79938	119	Core 6	6/15/09
8.88269	38.80048	120	Core 7	6/15/09
8.8828	38.80034	121	Core 8	6/15/09
8.88292	38.8002	122	Core 9	6/15/09
8.88371	38.80069	123	Core 10	6/15/09
8.8819	38.79954	124	Grid 14: SE corner	6/16/09
8.88189	38.79955	125	Grid 14: SW corner	6/16/09
8.88189	38.79956	126	Grid 14: NW corner	6/16/09
8.88223	38.79958	127	Grid 14: NE corner	6/16/09
8.88223	38.79937	128	Grid 15: SW corner	6/16/09
8.88255	38.79961	129	Grid 16: NW corner	6/17/09
8.88254	38.79973	130	Grid 16: NE corner	6/17/09
8.88221	38.79958	131	Grid 16: SW corner	6/17/09
8.88222	38.79974	132	Grid 16: SE corner	6/17/09

8.88225	38.79937	133	Core 12	6/17/09
8.88228	38.79954	134	Core 13	6/17/09
8.88222	38.79974	135	Core 14	6/17/09
8.88261	38.79975	136	Core 15	6/17/09
8.88219	38.79939	137	Grid 17: SW corner	6/17/09
8.88221	38.79989	138	Grid 17: SE corner	6/17/09
8.88256	38.79995	139	Grid 17: NE corner	6/17/09
8.88259	38.79976	140	Grid 17: NW corner	6/17/09
8.88292	38.80017	141	Grid 18: NE corner	6/18/09
8.8826	38.80018	142	Grid 18: SE corner	6/18/09
8.88262	38.79993	143	Grid 18: SW corner	6/18/09
8.88294	38.79996	144	Grid 18: NW corner	6/18/09
8.88328	38.79998	145	Grid 19: NW corner	6/18/09
8.8833	38.8002	146	Grid 19: NE corner	6/18/09
8.88294	38.80017	147	Grid 19: SE corner	6/18/09
8.88296	38.79995	148	Grid 19: SW corner	6/18/09
8.88258	38.80069	149	Stratigraphic Description	6/19/09
8.8826	38.80073	150	Stratigraphic Description	6/19/09
8.88337	38.80066	151	Grid 20: SW corner	6/19/09
8.88335	38.80089	152	Grid 20: SE corner	6/19/09
8.88374	38.80089	153	Grid 20: NE corner	6/19/09
8.88372	38.80069	154	Grid 20: NW corner	6/19/09
8.88333	38.80044	155	Grid 21: SW corner	6/19/09
8.88334	38.8006	156	Grid 21: SE corner	6/19/09
8.88373	38.80068	157	Grid 21: NE corner	6/19/09
8.8837	38.80048	158	Grid 21: NW corner	6/19/09
8.88337	38.80045	159	Core 17	6/19/09
8.88316	38.80098	160	Strat Descr. ash	6/20/09
8.88309	38.80111	161	Strat Descr. E of channel	6/20/09
8.88307	38.80145	162	Core 18	6/20/09
8.88327	38.80142	163	Core 20	6/20/09
8.88325	38.80146	164	Core 19	6/20/09
8.88293	38.80043	165	Grid 22: SW corner	6/20/09
8.88298	38.80058	166	Grid 22: SE corner	6/20/09
8.88341	38.80073	167	Grid 22: NE corner	6/20/09
8.88335	38.80053	168	Grid 22: NW corner	6/20/09
8.88323	38.80137	169	Grid 23: SW corner	6/20/09
8.88319	38.80142	170	Grid 23: SE corner	6/20/09
8.88342	38.80149	171	Grid 23: NE corner	6/20/09
8.88344	38.80137	172	Grid 23: NW corner	6/20/09
8.88339	38.80133	173	Bar Test: 14 m N, SW corner G 23	6/20/09
8.88225	38.80063	174	Control Well	6/20/09
8.88251	38.80067	175	Bar Test	6/20/09
8.881073	38.799263		Core 16	6/19/09

+ Collected using WGS 1984 datum UTM Zone 17N

2010 Control Points

Lat+	Long+	Point	Feature	Date
8.881616	38.799708	68	T 10: NE point	4/25/10
8.881299	38.799508	69	T 10: SE point	4/25/10
8.8814533	38.79922	70	T 12: SW point	4/25/10
8.8817789	38.799217	71	T 12: NW point	4/25/10
8.883815	38.80119	78	T 14: SE point	4/25/10
8.883905	38.80086	79	T 14: SW point	4/25/10
8.884204	38.80128	80	T 15: NE point	4/25/10
8.88434859	38.80079	81	T 16: NW point	4/25/10
8.8825123	38.800563	72	T 5: NE point	4/25/10
8.8824669	38.800262	73	T 5: SE point	4/25/10
8.8824215	38.799908	74	T 7: SW point	4/25/10
8.88261144	38.79988	75	T 7: NW point	4/25/10
8.88289249	38.801099	82	T 19: SW point	4/25/10
8.882911	38.8015	83	T 19: SE point	4/25/10
8.883101	38.801454	84	T 20: NE point	4/25/10
8.8830643	38.801099	85	T 20: NW point	4/25/10

+ Collected using WGS 1984 datum UTM Zone 17N